4-2012

A Data Driven Frequency Based Method For Electrical-Mechanical Actuator Condition Monitoring

Anthony J. Chirico III

A Data Driven Frequency Based Method For Electrical-Mechanical Actuator Condition Monitoring

by

Anthony J. Chirico III

A Thesis Submitted in Partial Fulfillment of the Requirements for the
Degree of Master of Science
in Mechanical Engineering

Supervised by

Assistant Professor Dr. Jason Kolodziej
Department of Mechanical Engineering
Kate Gleason College of Engineering
Rochester Institute of Technology
Rochester, New York
April 2012

Approved by:

Dr. Jason Kolodziej, Assistant Professor
Thesis Advisor, Department of Mechanical Engineering

Dr. Mark Kempski, Professor
Committee Member, Department of Mechanical Engineering

Dr. Ferat Sahin, Associate Professor
Committee Member, Department of Electrical Engineering

Dr. Edward Hensel, Department Head
Committee Member, Mechanical Engineering

Thesis Release Permission Form

Rochester Institute of Technology
Kate Gleason College of Engineering

Title:

A Data Driven Frequency Based Method For Electrical-Mechanical Actuator Condition Monitoring

I, Anthony J. Chirico III, hereby grant permission to the Wallace Memorial Library to reproduce my thesis in whole or part.

Anthony J. Chirico III

Date

Dedication

It is not possible to complete such a journey without the support and sacrifice of my family, to whom I dedicate this Thesis. I am grateful to my Mom and Dad for giving me an appreciation for the world and providing the opportunity to have such an education. I would especially like to thank my wife Emily. I would not be successful in this effort without her patience and support of my dreams and goals.

Acknowledgments

This research would not be possible without the support of Moog Inc. which funded my graduate education and provided the test equipment and resources necessary for laboratory set-up and data collection. I would like to personally thank Larry Hall for his guidance and support of this research and his contribution to my personal and professional development. I am fortunate to have the support of several others at Moog Inc. who allowed me to dedicate time to this research in concert with my daily work initiatives. Special thanks go to Rick Fosdick, Paul Stoelting, and Duff Bushway. I would also like to thank my thesis advisor, Dr. Jason Kolodziej, who provided constant guidance and support.

Abstract

A Data Driven Frequency Based Method For Electrical-Mechanical Actuator Condition Monitoring

Anthony J. Chirico III

Supervising Professor: Dr. Jason Kolodziej

This research investigates a novel data driven approach to condition monitoring of Electro-Mechanical Actuators (EMAs) consisting of feature extraction and fault classification. Since many common faults in rotating machinery produce unique frequency components, the approach is based on signal analysis in the frequency domain of both inherent EMA signals and accelerometers. The feature extraction process exposes fault frequencies in signal data that are synchronous with motor position through a series of signal processing techniques consisting of digital re-sampling, Power Spectral Density (PSD) computation, and feature reduction. The resulting reduced dimension feature is then used to determine the condition of the EMA with a trained Bayesian Classifier. Signal data collected from EMAs in known health configurations is used to train the algorithms so that the condition of EMA's with unknown health may be predicted. Laboratory results show that EMA condition can be determined over multiple non-steady operating conditions and is capable of isolating multiple faults that produce unique fault signatures.

Contents

List of Tables

List of Figures

Chapter 1

Introduction

1.1 Flight Control Actuation

Currently, many aircraft utilize hydraulic Servocontrols (SC) to control primary flight control surfaces. These types of actuators typically use Electrohydraulic Servovalves powered by a hydraulic supply system, and convert electrical position commands to an hydraulic output for positioning the ram. SC actuators are reliable and provide precise position accuracy. However, the hydraulic supply system includes many elements which drive the cost and weight of a vehicle. More recently, Electrohydrostatic Actuators (EHAs) have been incorporated on primary surfaces in addition to SCs (such as on the A380 and A350) or as a replacement for SCs completely (such as F35). Unlike SCs, EHAs are closed hydraulic systems with a motor and pump as the prime mover for the actuator and do not require a supporting hydraulic system.

Electrical-Mechanical Actuators (EMAs) are the next progression in flight control actuators as the industry continues to move towards the goal of All Electric Aircraft [1]. Currently, these types of actuators are used mainly on secondary flight control surfaces, such as Spoilers and Horizontal Tail Stabilizers. This is mainly due to the failure modes of the EMAs which can

not be mitigated in flight as easily as its EHA and SC counterparts. Specifically, the risk of jamming can cause a flight control surface to lock in place, compromising the safe operation of the flight control system. However, there are many benefits for more electric aircraft such as overall weight reduction, increased reliability, better maintainability, reduced operating costs and increased safety [2].

1.2 Integrated Health Management

Integrated Health Management (IHM) offers an advantage to make the adaptation of EMAs in critical applications more practical by indicating the need for service prior to catastrophic EMA failure and disruption of service. IHM is also a viable progression from Statistical Based Maintenance to Condition Based Maintenance (CBM) for flight control actuation systems. In CBM, the condition of the equipment is monitored and maintenance is based on the assessed condition. As such, IHM systems must be capable of monitoring degradation and detecting faults at the early stages of development, in advance of full functional failure.

IHM is usually comprised of data acquisition, signal reduction/feature extraction, condition assessment, fault diagnosis, prognostics, and decision support [3]. The signal data contains information about the condition of the unit, but in most cases is difficult to expose due to the size and hidden nature of the fault signatures within the data. As such, feature extraction is a technique or set of techniques to expose patterns or indicators in the data that give insight into the condition of the equipment and reduce the amount of data. These features are then used to provide a condition assessment and one or more fault diagnoses. Prognostics is the discipline related to predicting the future condition of the equipment which can then be used in decision

support. Approaches to IHM may be broadly categorized into experience, knowledge, data driven, and model based. Hybrid systems combine two or more of these approaches in order to take advantage of the strengths and minimize the weaknesses of each approach.

1.3 Review of EMA Condition Monitoring Techniques

The most common approaches for EMA IHM to date have been model based and data driven. Model based approaches typically involve the creation of an accurate mathematical model to predict the outputs to a set of inputs for assessing health. For instance, the error between the actual outputs and the model predicted outputs can be used to estimate system parameters such as damping and efficiency. The estimated parameters can then be compared to the parameters of a healthy system to determine if there is a fault. This approach was utilized in [4] by injecting faults or altering model parameters in a validated actuator model and then diagnosing the faults through parameter estimations. For instance, the effective number of motor windings were derived from motor current and voltage signals through least squares optimization. The parameter could then be used to diagnose the severity of the fault. Another recursive model estimation approach was demonstrated in [5] which estimated frictional damping coefficient, local gear stiffness and torque constant parameters to assess health, isolate faults, and predict fault severity.

Noted benefits of the model based approach were that failure modes are traced back to model parameters to lend insight into the failure for fault diagnosis. In addition, the severity of the fault could be characterized by the deviation of the estimated parameters to the healthy EMA parameters which

were previously characterized. This type of approach is also suited to predict health over multiple non-steady operating conditions, but only as long as command and disturbances can be measured or calculated. The drawback of the model based approach is that models are often complex and must be validated. As such, the models are then very specific to the application and new models must be created and validated for each new application. In addition, implementing this type of scheme in an EMA controller would require a significant amount of processing capability when added to the normal control and management schemes typically employed for flight control actuators.

As opposed to model based techniques, data driven approaches operate directly on signal data without the use of mathematical models, and use signal processing techniques to expose patterns/signatures in signal data that give insight into machine condition. Data driven approaches are an attractive option to IHM since it does not require complex models and can be applied to many types of systems.

Within the field of actuator fault detection and isolation, data driven techniques have included Wavelet analysis, Statistical analysis, Neural Network analysis, and Frequency Domain analysis. For instance, [6] used several statistical features including accelerometer sensor standard deviation, thermocouple temperature deviation from nominal, and thermocouple drift. In [7] vibration sensors were used to detect fault frequencies that would appear as components started to wear. In [8] one of the methods employed was to measure the degree of overlap of signal probability densities between a baseline ”Healthy” EMA set and EMAs with artificially aged capacitors during steady state operating conditions.

The previous works cited focused primarily on feature extraction, but

several other works also included health classification and prognostics, such as [9] which was applied to a hydraulic actuator. Here, FFT based features were used in addition to a neural network error tracking method. Automated health classification was accomplished by a Fuzzy Logic classifier with data fusion. Finally, a prognostics model was developed using a Kalman filter feature based state space tracking routine for fault to failure prediction. Another approach taken by [10] used the Hilbert Transformation as the feature extraction technique for identifying turn-to-turn winding faults for a Brushless DC motor in an EMA and a particle filter for anomaly detection and prognostics.

One of the main problems cited in EMA condition monitoring research is the masking of defects due to differing and non-constant operating conditions. For instance, as motor speed and load vary, the amount of vibration changes and fault frequencies are spread throughout the frequency spectrum, making fault identification difficult. This problem was also cited by [11] who proposed the use of the Discrete Wavelet Transform (DWT) to show how frequency content varies with time with non-stationary conditions. The energy of each DWT detail was used as the feature for fault detection. An alternate approach using Wavelets was proposed by [12], who combined the wavelet transform with FFT post-processing to isolate specific fault frequencies. Another approach to deal with non-steady motor velocities was proposed in [13] who used a digital re-sampling method to map signals from the time domain to the spatial domain, since many faults in rotating machinery are synchronous with motor position.

There are several other challenges in EMA condition monitoring that could benefit from research done in related areas. One issue that arises in

EMA condition monitoring is the permissibility of using specialized sensors. As a result, emphasis has been placed on the ability to use only available EMA signals. A technique known as Motor Current Signature Analysis (MCSA) has been shown to be successful for identifying faults in components that are part of motor controlled systems, such as motor, bearing and gear faults [14]. Another challenge is due to the potentially large number of feature variables that result from using multiple feature extraction methods. Principal Components Analysis (PCA) is a way of identifying patterns in data and reducing the dimensionality of the data. Another important aspect of PCA is that it transforms a set of possibly correlated variables into a set of principal components which are linearly uncorrelated. The PCA technique has been used for various applications, including face recognition and image compression, but also in fault detection and classification. For instance [15] uses PCA as a feature selection scheme for contending features for bearing defect classification.

1.4 Approach and Objectives

This research focuses on the feature extraction and fault diagnosis portions of the IHM process for condition monitoring of EMAs. The goal is to improve upon previous research in EMA health monitoring by creating a data driven approach that is able to handle non-steady motor speeds and multiple loading conditions, is able to use standard and non-standard EMA sensors, and can handle multiple contending features.

The research paper is organized as follows: Chapter 1 gave an assessment of the current state of Flight Controls Actuators and the progression

from hydraulic actuators towards EMAs. The need for EMA Health Management was given and a comprehensive review of EMA health monitoring research was presented including the challenges that exist. Chapter 2 presents the proposed approach to feature extraction and fault classification together with the associated principles and mathematics. In Chapter 3 the approach is demonstrated via simulation using generated data for healthy and defective signals. In Chapter 4, the approach is tested with laboratory generated EMA data over five different operating conditions using a healthy EMA and an EMA with a bearing fault. The performance of the approach is demonstrated by the percentage of false positives and false negatives. Finally, plans for improvement and future work is given in Chapter 5.

Chapter 2

EMA Fault Detection Approach

The fault detection scheme after data acquisition is comprised of feature extraction and fault classification as shown in Figure 2.1. The objective is to assign a class that relates to the condition of the EMA based on the sensor measurements, $\mathbf{x}$. Ideally the predicted condition matches the true condition of the EMA. The system from which measurements are obtained includes the EMA to be monitored and the associated environment. The system is excited with inputs $\mathbf{r}$, and results in the measurement outputs, $\mathbf{x}$. The measurement data is transformed after data acquisition by the feature extraction process in order to give insight into the condition of the EMA. It also serves to reduce the size of the data prior to classification. A feature vector, $\mathbf{z}$, is then input to a classifier which uses this data to predict the condition of the EMA, $\omega(\mathbf{z})$, from a possible set of conditions $\omega \, \epsilon \, \{\omega_1, \omega_2, \omega_3, \ldots\}$.

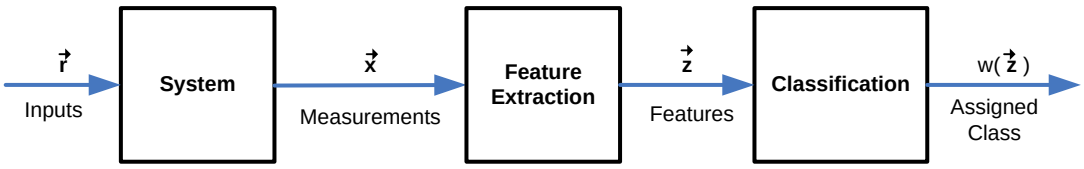

Figure 2.1: EMA Fault Detection Architecture

2.1 Feature Extraction Technique

In Feature Extraction, the measurement data is transformed in order to expose patterns and signatures within the data that give insight into the condition of the EMA. The feature extraction method proposed in this paper is aimed at exposing faults that produce fault signatures in the frequency domain that are synchronous with motor position. Frequency analysis of vibration and motor current signals has been shown to be effective in exposing fault signatures in rotating machine equipment, including: bearing and gear faults, screw defects, stator and armature faults, broken rotor bar and end ring faults, and eccentricity faults among others [16, 17, 18, 19]. For instance, the mechanical defect frequency produced by an inner race defect on a ball bearing is

$$f_{IR} = \frac{n}{2} f_r \left(1 - \frac{BD}{PD} \cos\phi\right) \tag{2.1}$$

where n equals the number of rotating elements (balls), BD is the ball diameter, PD is the pitch diameter, ϕ is the contact angle, and f_r is the motor speed expressed in Hz.

The defect will appear in the motor current signal at the following frequency:

$$f_c = |f_e \pm m f_{IR}| \tag{2.2}$$

where m is an integer accounting for the harmonic contributions, and f_e is the fundamental current frequency. For a three phase Permanent Magnet Synchronous Motor, the fundamental current frequency is related to the rotor frequency by

$$f_e = \frac{p}{2} f_r \tag{2.3}$$

where p is the number of motor poles. Therefore equation 2.2 becomes

$$f_c = f_r \left| \frac{p}{2} \pm \frac{m f_{IR}}{f_r} \right| \tag{2.4}$$

In general, EMAs have velocities which are non-constant, therefore fault frequencies will vary with the motor frequency.

In this research, the feature extraction architecture shown in Figure 2.2 is proposed. Signal data that is originally sampled according to the fixed time sampling interval, T_s, is re-sampled to the spatial domain according to the spatial sampling interval, θ_s. The signal is then transformed to the order domain (as opposed to the frequency domain as a result of the spatial resampling) by computing the Power Spectral Density (PSD). The PSD is filtered and then a binning process groups the frequency content into energy bins. The data is then reduced by a Feature Space Transformation process which maps the data to a lower dimension space via a transformation matrix. The transformation matrix is optimized using training samples so that the most important information in the data is retained.

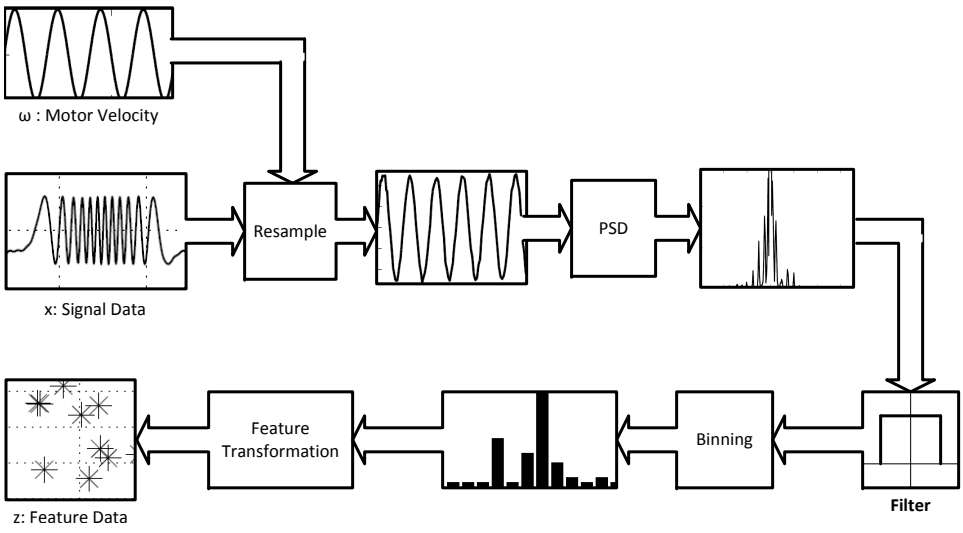

Figure 2.2: Feature Extraction PSD Method

2.1.1 Resampling Technique

Many electrical and mechanical fault signatures in rotating equipment are synchronized with the angular motor position. Since normal operation of an EMA for many applications involves varying motor speeds, fault signatures will be periodic with motor position, but not in time. If signals are acquired according to the fixed-time sampling period, T_s, a post processing method must exist to resample the signal according to the spatial sampling period, θ_s, to expose the periodic nature of the fault.

Consider a motor velocity signal, $\omega(t)$ that ramps uniformly in time and the corresponding cumulative motor angle, $\theta_c(t)$:

$$\omega(t) = 100t \tag{2.5}$$

$$\theta_c(t) = 50t^2 \tag{2.6}$$

When the signal is sampled with period T_s, the discrete signal representation is

$$\omega(k) = 100kT_s \tag{2.7}$$

$$\theta_c(k) = 50k^2T_s^2 \tag{2.8}$$

If the motor angle is not acquired directly, it may be approximated from the motor velocity signal, for instance (Trapezoidal Integration):

$$\theta_c(k) = \frac{T_s}{2}\sum_{m=0}^{k}\omega\left(\left(m-1\right)T_s\right) + \omega\left(mT_s\right) \tag{2.9}$$

Note that this is an expression for the cumulative motor angle. The circular motor angle has a value in the interval $(0, 2\pi)$ which may be obtained by

$$\theta_m(k) = mod\left(\theta_c\left(k\right), 2\pi\right) \tag{2.10}$$

Next, consider a signal, $x_1(t)$, that has a fault frequency dependent upon the motor angle as follows:

$$x_1(t) = \sin\left(6\theta_c(t)\right) = \sin\left(300t^2\right) \tag{2.11}$$

After time sampling, the discrete signal may be represented by

$$x_1(k) = \sin\left(300k^2T_s^2\right) \tag{2.12}$$

A simulation of the resulting signals over 0.5 seconds is shown in Figure 2.3. Note that the signal, x_1, is not periodic in time, but is periodic when plotted against the cumulative motor angle.

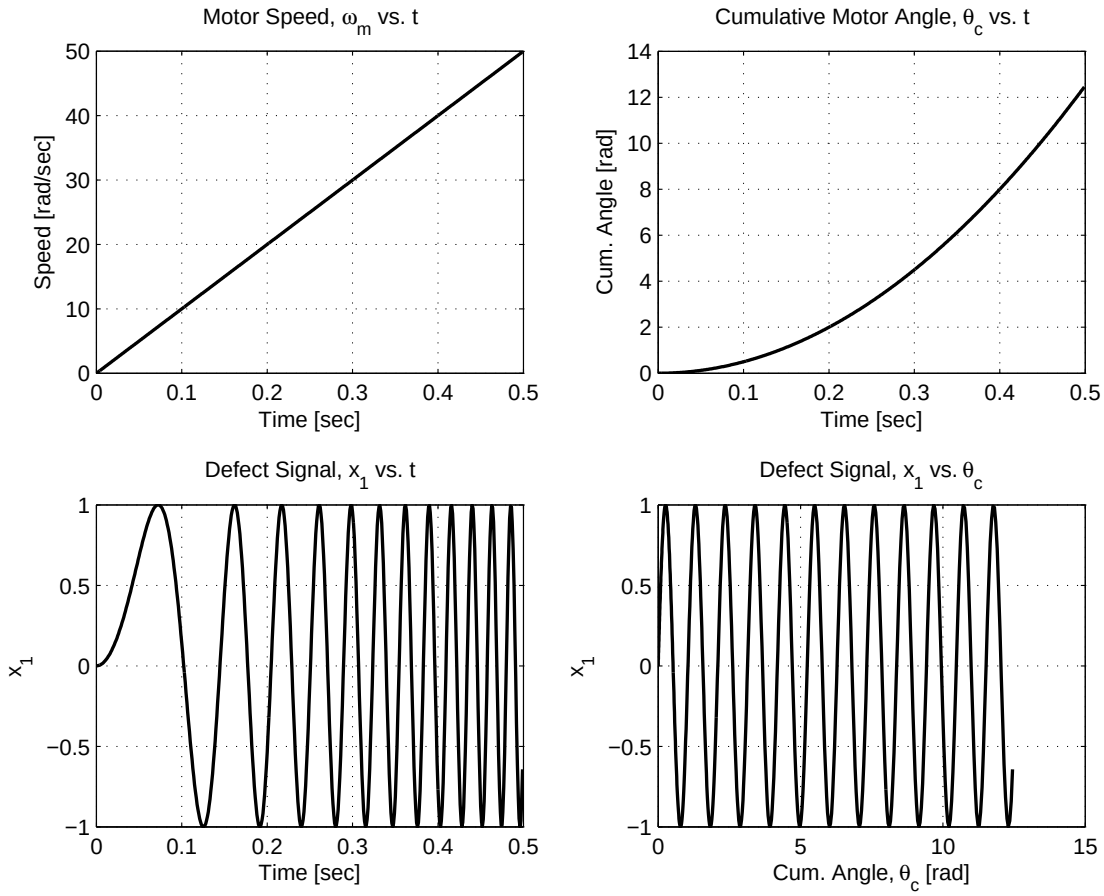

Figure 2.3: Example of Defect Signal Periodicity with Motor Angle

To make the sampled signal, $x_1(k)$ periodic, the time sampled signal must be re-sampled based on motor angle. For this research a simple linear interpolation formula is used:

$$x(n) = x(k) + \frac{x(k) - x(k-1)}{\theta_c(k) - \theta_c(k-1)} \left(n\theta_s - \theta_c(k-1)\right) \tag{2.13}$$

The equation maps the time sampled signal $x(k) = x(kT_s)$ to the spatially sampled signal $x(n) = x(n\theta_s)$. Note that there will be an associated interpolation error since the exact value of the signal between data points, $\theta_c(k-1) < n\theta_s < \theta_c(k)$ is unknown. In order to prevent signal aliasing the sample period, θ_s, should be less than one half the smallest period per revolution of the motor for a given signal. For instance, the signal x_1 has a frequency of six times per motor revolution, therefore $\theta_s < \frac{2\pi}{12}$ rad. The finer the sampling period, the more accurate the resampled signal will be until it exceeds the resolution of the time sampled motor position signal at which point the signal is essentially upsampled. Figure 2.4, shows the re-sampled signal $x_1(n)$ using Equation (2.13), with $\theta_s = 2\pi/60$ radians. The samples shown appear at 10 times per period. Thus, for any motor velocity this method will synchronize the frequencies of a signal that are periodic with motor position, as expected with common EMA defects.

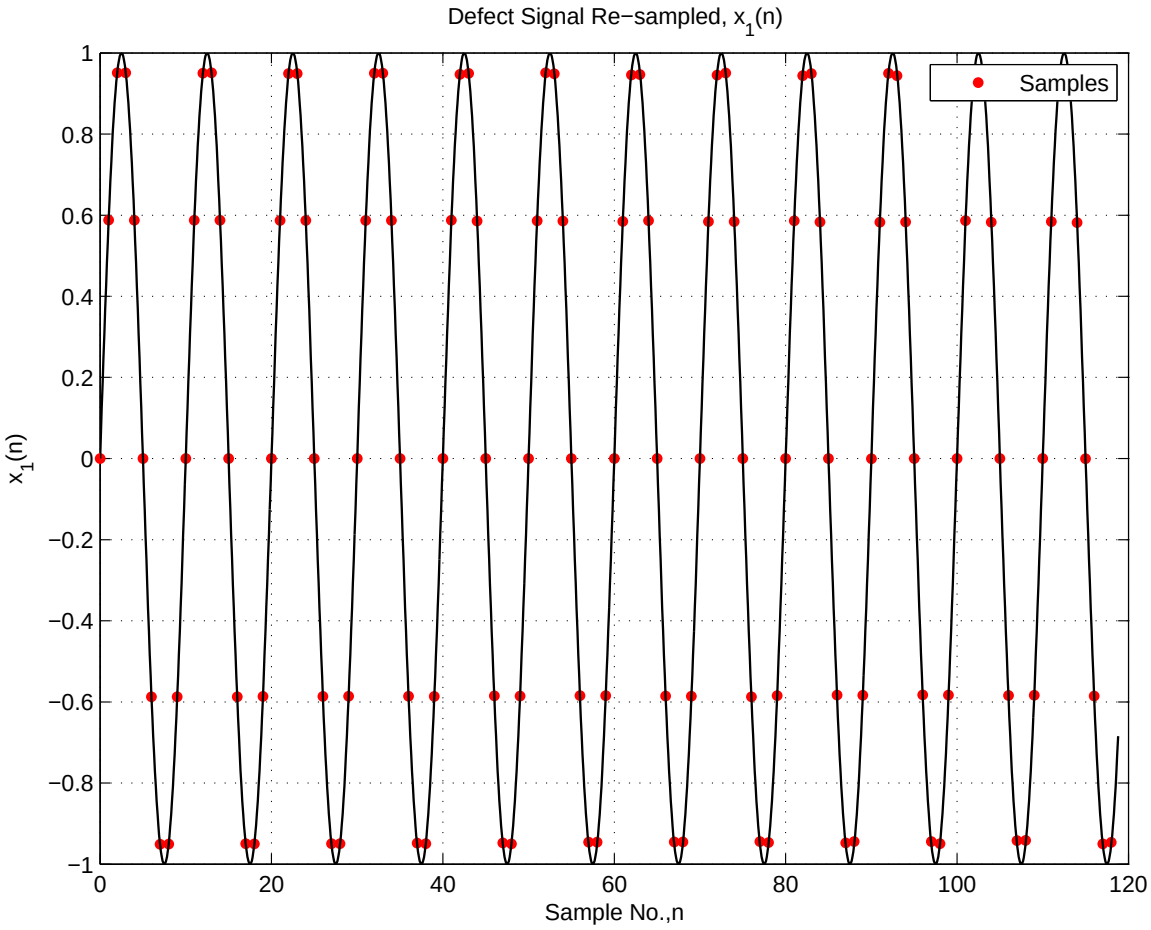

Figure 2.4: Example of Defect Signal After Resampling

2.1.2 Power Spectral Density

The two sided power spectrum of a discrete signal is

$$S_{xx}(k) = \frac{1}{w_f L^2} X_w(k) X_w^*(k) \qquad -L/2 < k \leq L/2 \tag{2.14}$$

where L is the number of samples, and $X_w(k)$ is the Discrete Fourier Transform (DFT) of the windowed signal $x_w(n)$:

$$X_w(k) = \sum_{n=o}^{L-1} x_w(n) e^{-i2\pi k \frac{n}{N}} \tag{2.15}$$

The windowed signal $x_w(n)$ is the signal $x(n)$ multiplied by a window function $w(n)$:

$$x_w(n) = w(n)x(n) \tag{2.16}$$

For instance, a rectangular window results when $w(n) = 1$, or a Hanning Window of length L may be used to reduce the effect of leakage to out of band frequencies, Equation (2.17).

$$w(n) = \frac{1}{2}\left(1 - \cos\left(2\pi\frac{n}{L}\right)\right) \tag{2.17}$$

The window factor, w_f, is needed to scale the power spectrum to account for the loss of amplitude when using a non-rectangular window,

$$w_f = \frac{1}{L}\sum_{k=0}^{L-1} w(k)^2 = \frac{1}{L}w'w \tag{2.18}$$

In many cases, the DFT may be computed by a more computationally efficient algorithm known as the Fast Fourier Transform (FFT). For instance when the number of samples is a power of two, the radix-2 Cooley-Tukey FFT algorithm may be used. Since a single FFT has some uncertainty, several FFTs of length L are computed for a given signal and the resulting two sided power spectrums are averaged together to get a more accurate estimate

$$\bar{S}_{xx}(k) = \frac{1}{M}\sum_{m=1}^{M} S_{xx}^m(k) \tag{2.19}$$

where M is the total number of computed two sided power spectrums, and S_{xx}^m denotes the m^{th} power spectrum. Next, the one sided power spectrum is computed from the averaged two sided power spectrum

$$G_{xx}(k) = 2\bar{S}_{xx}(k) \qquad k = 1, ..., L/2 \tag{2.20}$$

$$G_{xx}(0) = \bar{S}_{xx}(0) \tag{2.21}$$

Finally, the one sided continuous PSD is estimated from the one sided discrete power spectrum by

$$\tilde{G}_{xx}(k) = T_p G_{xx}(k) \tag{2.22}$$

where $T_p = L/F_s$ is the period of the signal sampled with frequency $F_s = 1/T_s$.

Consider the sinusoidal signal, x_2, with unit amplitude and cyclic frequency, F,

$$x_2(t) = sin(2\pi F t) \tag{2.23}$$

When the signal is sampled with frequency, F_s, the resulting sampled signal is

$$x_2(n) = sin(2\pi f n) \tag{2.24}$$

where $f = F/F_s$. As an example, let $F = 40$Hz, and $F_s = 640$Hz. The corresponding continuous and discrete sampled signals along with their respective one sided power spectrums are shown in Figure 2.5. As expected, the discrete power spectrum has an amplitude of 0.5 at a normalized frequency of $f = F/F_s = .0625$ cycles per sample and the continuous power spectrum has an amplitude of .025 at $F = 40$ Hz. Note that the number of samples used in the simulation was $L = 32$ and a rectangular window was used to compute the FFT.

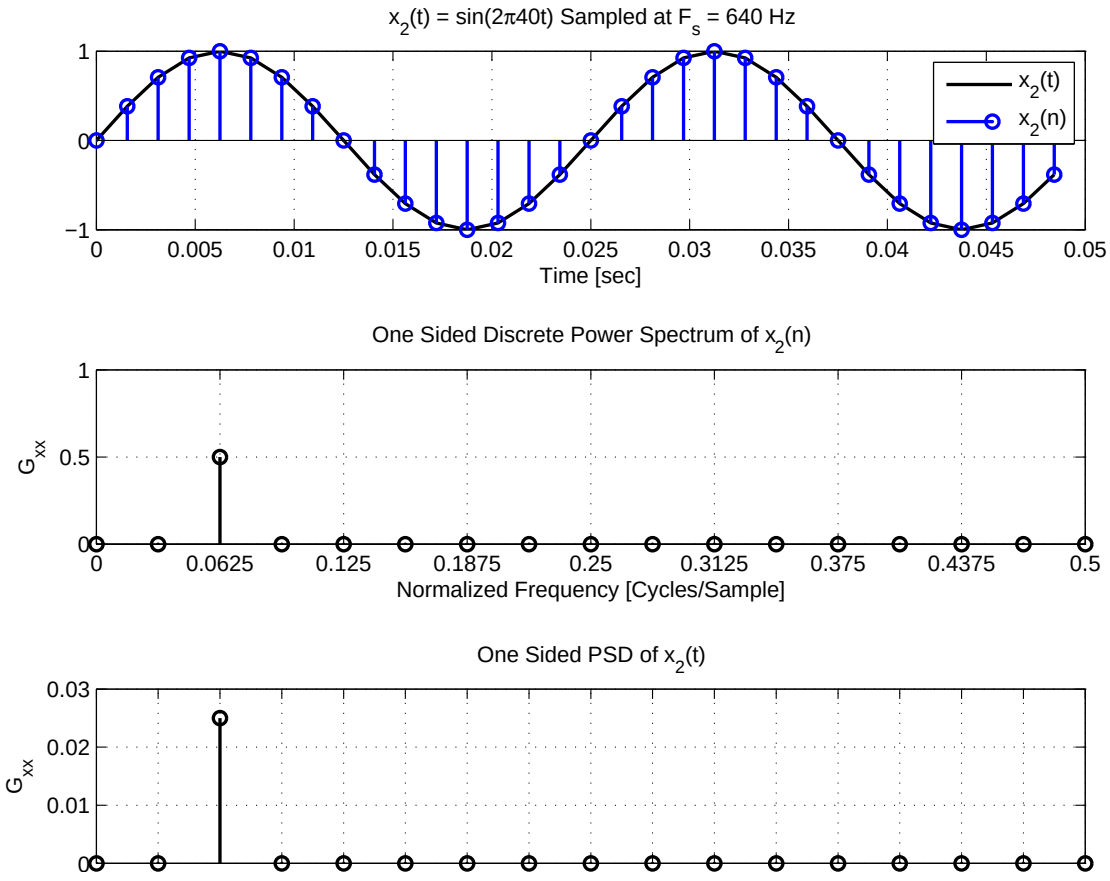

Figure 2.5: Continuous and Discrete Sampled Signals and Power Spectrum

Next consider the signal $x_1(t)$ in Equation (2.11) whose frequency is dependent upon the motor angle θ. The signal along with the corresponding PSD is shown in Figure 2.6.

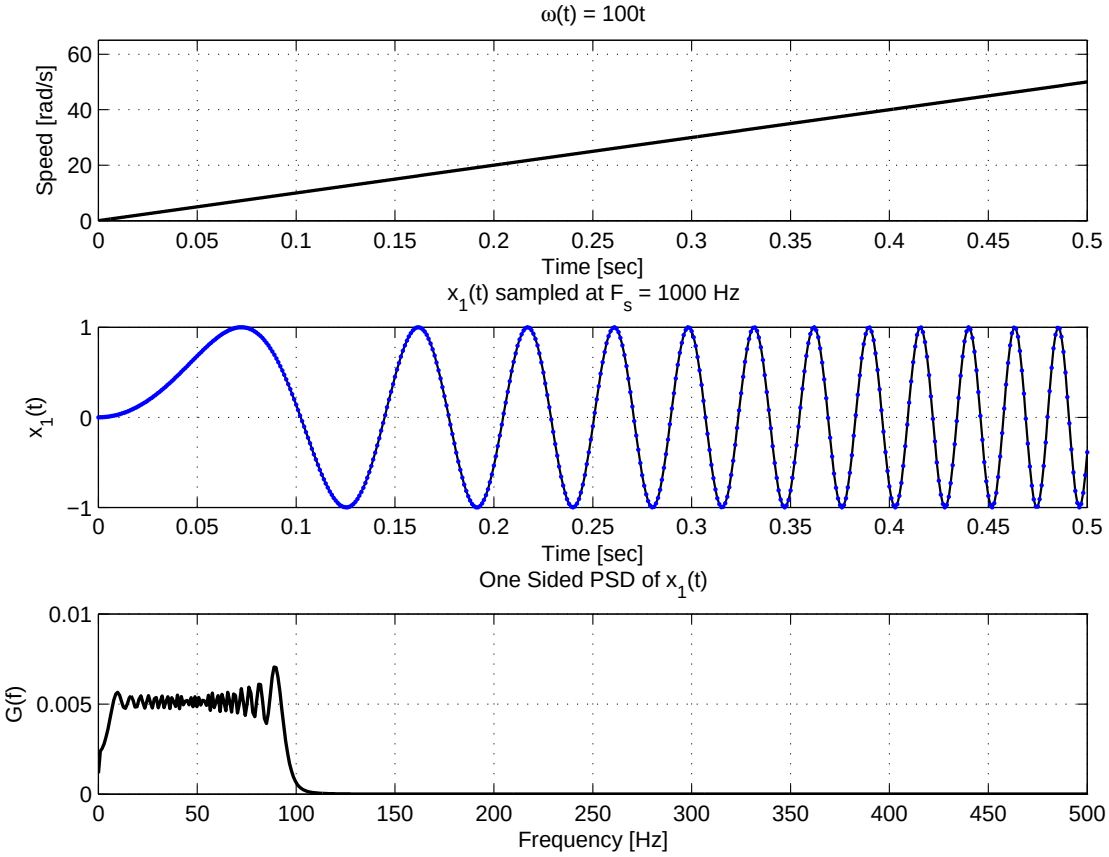

Figure 2.6: Signal and Power Spectrum of $x_1(t)$

Since the motor velocity is increasing uniformly, the frequency of the signal, $x_1(t)$, is also increasing. This results in a smearing of the frequency content from 0 to about 100 Hz. If the motor velocity waveform were to change, as in the case of EMAs under different operating conditions, the frequency content of the signal $x_1(t)$ would also change, making it difficult to detect any defect frequencies that are synchronous with the motor velocity. However, if the signal is resampled according to Equation (2.13), with $\theta_s = 2\pi/60$ radians per sample, then the resulting PSD has a narrow frequency band around 6 orders only (Figure 2.7). The scale continues to $O_{max} = 30$ orders since the resample frequency was 60 times per motor

revolution. The frequency resolution for the samples of the continuous PSD is $\delta o = O_{max}/L = .1172$ since the number of samples used in the FFT was $L = 256$. There is not a single sharp peak since 6 orders is not an exact multiple of the resolution, resulting in a slight leakage effect using a rectangular window. The other source of leakage is due to integration and interpolation errors. Despite the leakage effects, the approximate frequency of the signal can be determined from the PSD without attenuating the signal amplitude much. Therefore the combination of resampling and PSD computation will reveal the frequency content in a signal that is synchronous with motor velocity as expected with common EMA defects.

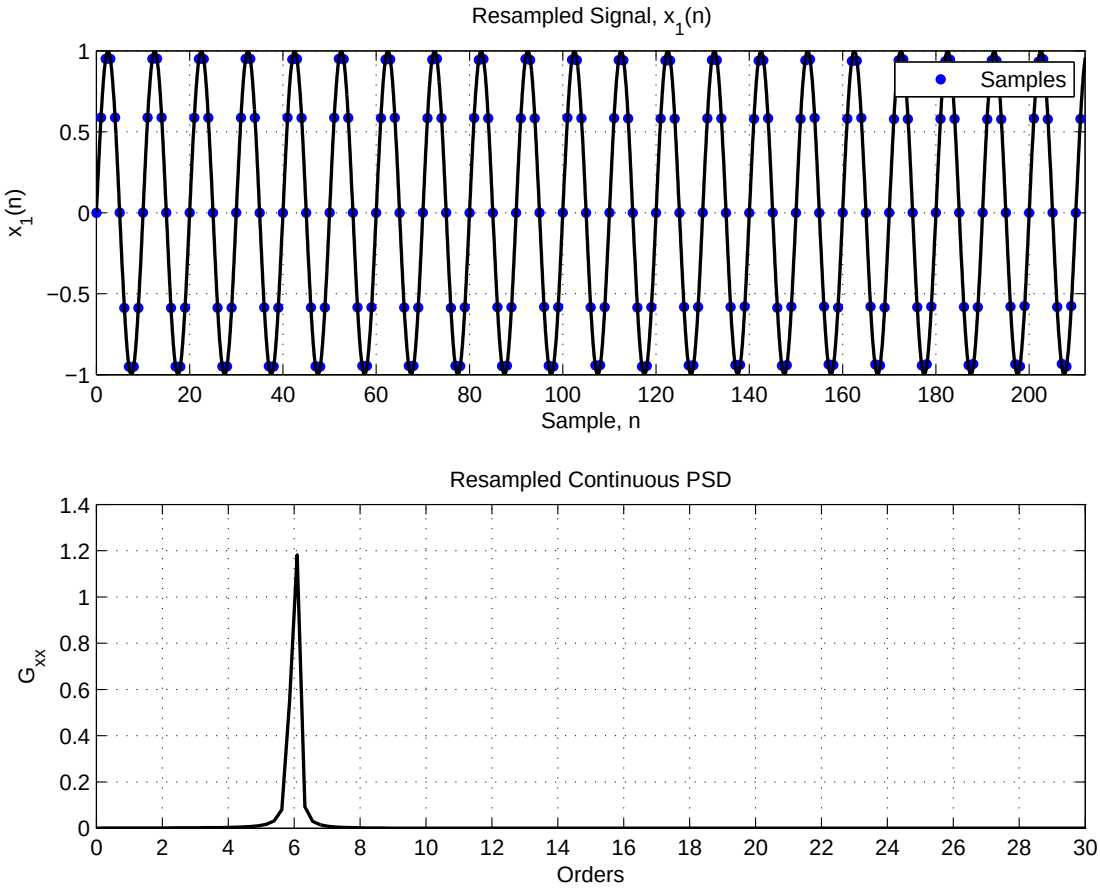

Figure 2.7: Resampled Signal and Power Spectrum

2.1.3 Feature Space Transformation

After resampling and PSD computation, the PSD samples are grouped into energy bins of size δb using the trapezoidal integration method, illustrated in Figure 2.8.

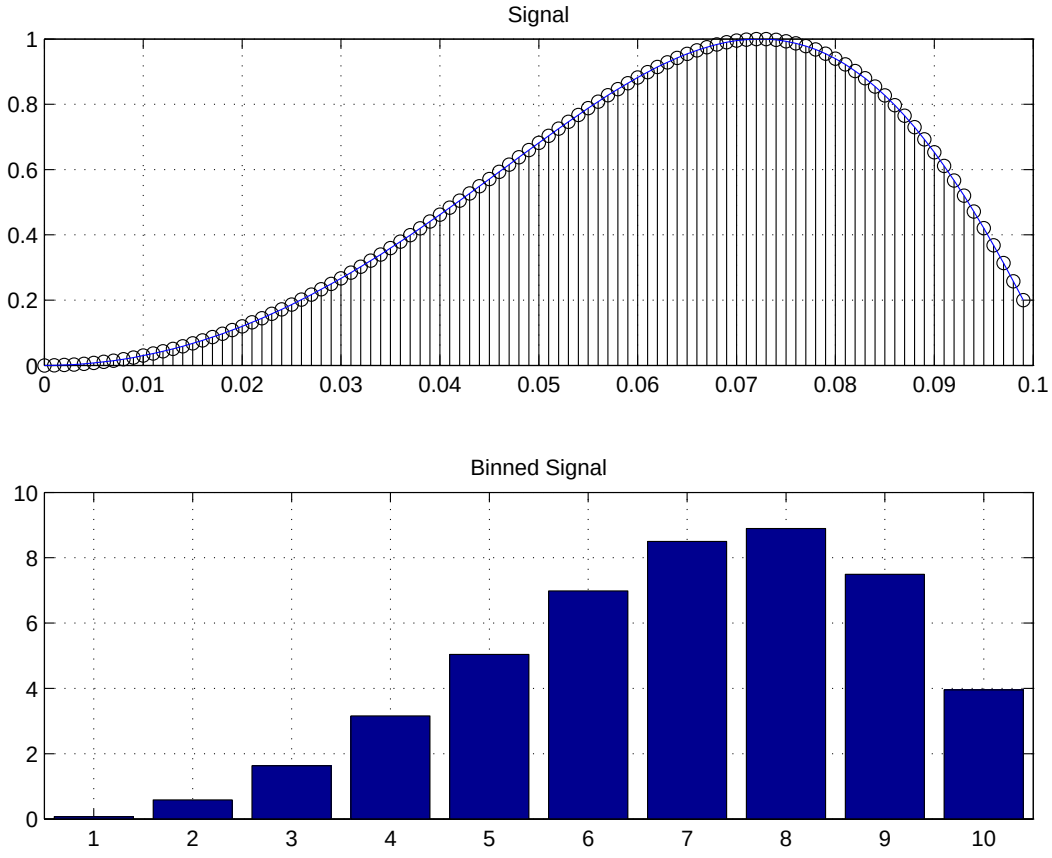

Figure 2.8: Illustration of Binning Concept

Since the signal is first translated to the rotational domain, the PSD transforms the data into an order spectrum (as opposed to the frequency spectrum). The resulting binned PSD vector from a single data set consists of N elements,

$$\mathbf{y} = [y_1, y_2, y_3, ..., y_N]^T \tag{2.25}$$

Each of the components of $\mathbf{y}$ correspond to the magnitude of the binned PSD at specific orders of motor frequency for a single trial run. Since N will typically be large in PSD computations, a method must be used to reduce the size of the PSD vector prior to classification in order to limit the number of training samples required. The exact orders of interest are assumed to be unknown for a data driven process and we cannot simply choose certain components of the PSD vector and discard the rest. Thus, in order to reduce the dimension of the vector, a transformation is needed to map from a space with a large dimension N to a smaller dimension D while retaining the information needed to identify a fault. This is accomplished using the linear transformation,

$$\mathbf{z} = \mathbf{W}\mathbf{y} \tag{2.26}$$

The linear transformation (or weight) matrix, $\mathbf{W} \epsilon D \times N$, maps the PSD vector $\mathbf{y}$ onto the reduced dimension feature vector $\mathbf{z}$ (Figure 2.9).

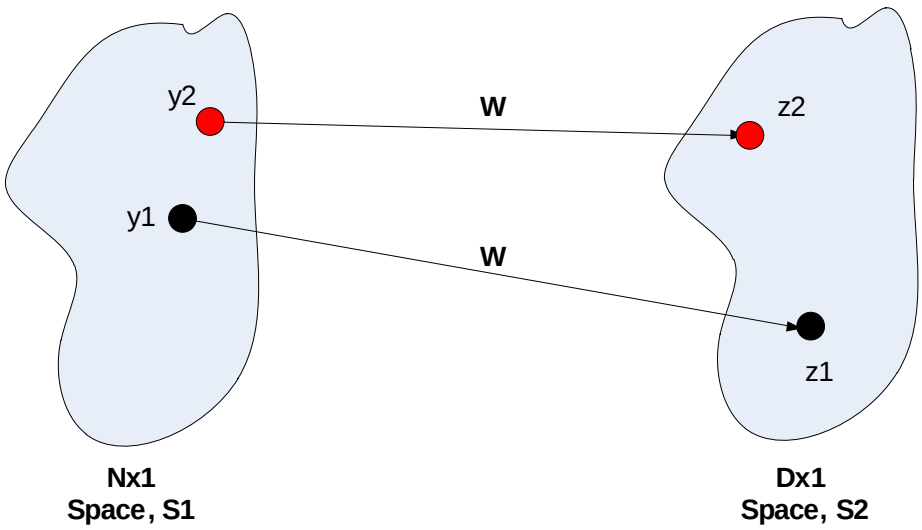

Figure 2.9: Feature Space Transformation

Principal Components Analysis (PCA) is chosen to obtain the components of the weight matrix using data from a training set. A training set consists of PSD computations from signal data collected from a population of known healthy units, and units that are known to have defects. The PCA technique produces principal components that explain a percentage of the variances present in the data (training) set. The goal of the PCA technique when applied in this manner is to obtain a transformation matrix that weighs the PSD orders which give the most insight into the health of the machine more heavily (i.e. the components that differ between healthy and defective units). The orders that differ in magnitude between the healthy and defective data should produce a larger variance resulting in a larger weighting.

For multiple trial runs in which data is collected from EMAs over the course of several experiments, the PSD vector will have random variation from one run to the next. As such, the elements of $\mathbf{y}$ may be treated as random variables having a specific probability distribution based on the condition of the EMA. For example, a set of normal/healthy EMAs may have a different probability distribution for some PSD orders than for EMAs with defects. Let the training set PSD vector be denoted by $\mathbf{Y_{ts}}$ (Equation (2.27)), consisting of training data from a population of known healthy units, $\mathbf{Y_h}$ (Equation (2.28)) and data from a population of EMAs with known defects, $\mathbf{Y_{d1}}, \mathbf{Y_{d2}}, \cdots, \mathbf{Y_{dm}}$ (Equation (2.29)).

$$\mathbf{Y_{ts}} = [\mathbf{Y_h}, \mathbf{Y_{d1}}, \mathbf{Y_{d2}}, \cdots, \mathbf{Y_{dm}}] \tag{2.27}$$

$$\mathbf{Y_h} = \begin{bmatrix} y_{h_{11}} & y_{h_{12}} & y_{h_{13}} & \cdots & y_{h_{1N}} \\ y_{h_{21}} & y_{h_{22}} & y_{h_{23}} & \cdots & y_{h_{2N}} \\ \vdots & \vdots & \vdots & \ddots & \vdots \\ y_{h_{K1}} & y_{h_{K2}} & y_{h_{K3}} & \cdots & y_{h_{KN}} \end{bmatrix} \tag{2.28}$$

$$\mathbf{Y_{di}} = \begin{bmatrix} y_{di_{11}} & y_{di_{12}} & y_{di_{13}} & \cdots & y_{di_{1N}} \\ y_{di_{21}} & y_{di_{22}} & y_{di_{23}} & \cdots & y_{di_{2N}} \\ \vdots & \vdots & \vdots & \ddots & \vdots \\ y_{di_{K1}} & y_{di_{K2}} & y_{di_{K3}} & \cdots & y_{di_{KN}} \end{bmatrix} \tag{2.29}$$

Each of the rows represent a different sample from the training set population and each of the columns represent a specific order in the binned PSD vector. The PCA technique computes the eigenvectors and corresponding eigenvalues of the covariance matrix of the training set matrix. Each eigenvalue and corresponding eigenvector explains a percentage of the total variation of the training set. The larger the eigenvalue, the more representative the associated eigenvector explains the variation. A total of N eigenvalues and eigenvectors are computed, but only the D largest are retained that explain a certain percentage of the variation (typically 90%). The weight matrix is given by the D eigenvectors ordered from the largest eigenvalue to the smallest:

$$\mathbf{W} = \begin{bmatrix} e_{11} & e_{12} & e_{13} & \cdots & e_{1N} \\ e_{21} & e_{22} & e_{23} & \cdots & e_{2N} \\ \vdots & \vdots & \vdots & \ddots & \vdots \\ e_{D1} & e_{D2} & e_{D3} & \cdots & e_{DN} \end{bmatrix} \tag{2.30}$$

From Equation (2.26), the PCA technique maps the vector $\mathbf{y}$ onto the feature vector (also known as principal component vector), $\mathbf{z} = [z_1, z_2, ..., z_D]^T$ by

$$z_i = e_{i1}y_1 + e_{i2}y_2 + e_{i3}y_3 + ... + e_{iN}y_N \tag{2.31}$$

Thus, the first principal component explains the most training set variance, the second component explains the second most variance, and so on. In addition, the PCA transforms the set of possibly correlated variables into a set of principal components which are linearly uncorrelated.

To demonstrate the methodology, let the PSD vector $\mathbf{y}$ consist of $N = 4$ elements

$$\mathbf{y} = [y_1, y_2, y_3, y_4] \tag{2.32}$$

Each of the components of $\mathbf{y}$ correspond to the magnitude of the PSD at a specific order for a single trial run. Treating each of component of $\mathbf{y}$ as a random variable, each component is assumed to have a specific probability distribution based on the condition of the EMA. As an example, let $\mathbf{y_H}$ denote the PSD vector from a healthy unit containing components that are normally distributed

$$\mathbf{y_H} \sim [N(1, .01), N(10, .01), N(5, .01), N(4, .01)] \tag{2.33}$$

The notation $N(\mu, \sigma^2)$ is the representation for a normal probability density with mean μ and variance σ^2. Let's now assume that an EMA with a bearing inner ring defect has a PSD vector, $\mathbf{y_D}$ with the following distributions:

$$\mathbf{y_D} \sim [N(1, .01), N(10, .04), N(6, .01), N(4, .01)] \tag{2.34}$$

In this example, the distribution from the healthy EMA is the same as the distribution for the EMA with bearing defect except for components y_2 and y_3, which have a slightly different variance and a slightly different mean, respectively. The probability distributions for the healthy and defective sets are shown in Figure 2.10.

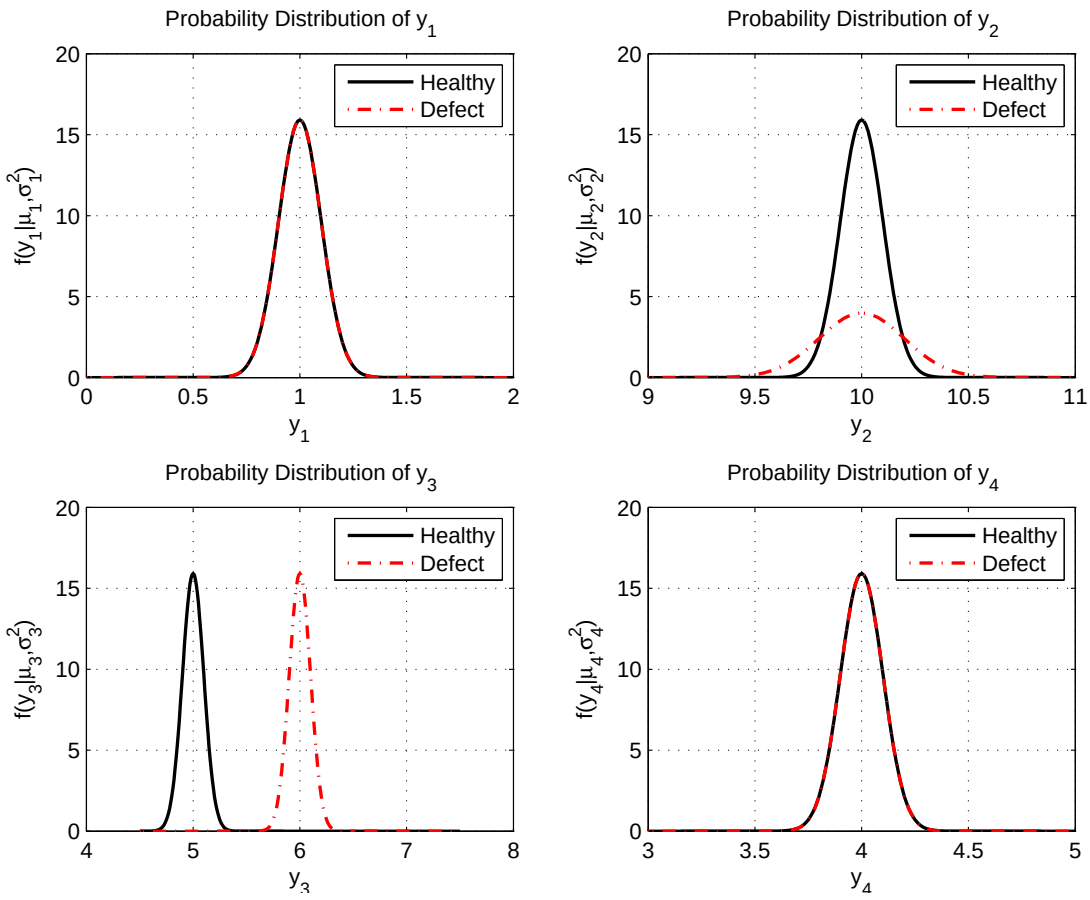

Figure 2.10: Probability Distributions for Healthy and Defective Sets

A set of 500 samples of training set data is generated according to the probability distributions for both the healthy and the defective distributions resulting in a training set vector that is 1000x4. The resulting eigenvalues and associated eigenvectors of the training set covariance matrix is shown in Table 2.1. The first eigenvalue contributes 86% of the total variance in the training set and the weighting of the y_3 component dominates. This result is expected since this component shows the greatest distinction between the healthy and defective data. The second eigenvalue contributes another 8% to the total training set variance, largely due to the second component y_2 which was the other distinguishing component. For all intents and purposes

Table 2.1: Computed Eigenvalues and Eigenvectors of Training Set Covariance Matrix

Eigenvector	e_1	e_2	e_3	e_4
Eigenvalue	0.261	0.024	0.010	0.009
Contribution %	85.7	7.9	3.4	3.1
y_1	-0.001	-0.053	0.596	-0.801
y_2	0.007	-0.997	-0.074	0.010
y_3	-0.999	-0.006	-0.009	-0.005
y_4	-0.010	-0.054	0.799	0.599

the last two principal components may be discarded since they contribute very little to the overall variation. Applying equation 2.31 to each of the 1000 data sets in the training set matrix using only the first two principal components results in the transformed data in Figure 2.11.

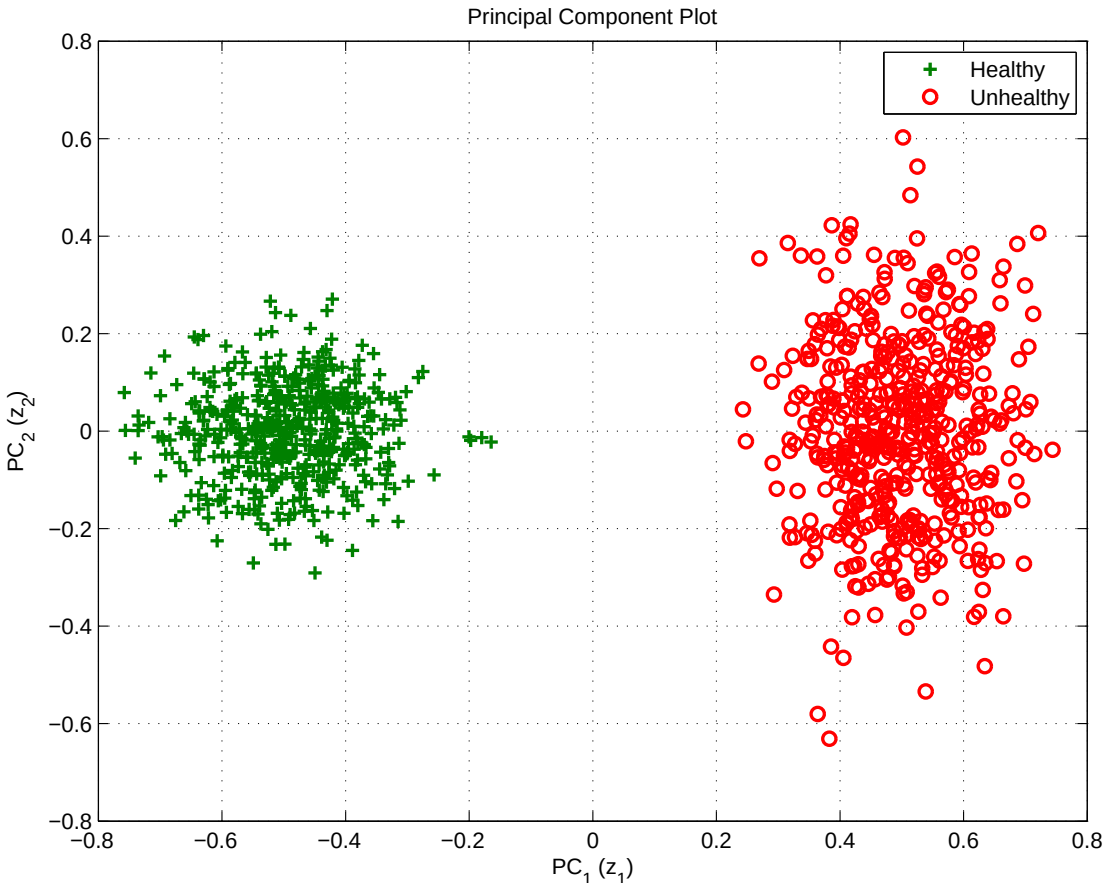

Figure 2.11: Principal Component Plot of Training Set Data

The principal component plot clearly shows a distinction between data from the healthy set and data from the defective set. Thus, the PCA technique has reduced the number of components from four to two (indeed only one component, PC_1 is really needed) without loss of the relevant information. Therefore, for a unit with unknown health status, the vector $\mathbf{y}$ can be transformed to the principal component space using the weight matrix computed from the first one or two eigenvectors. The data can then be used to classify the true state of health of the unit depending on the location of the data point in the transformed space.

2.2 Classification

In classification the objective is to assign a class label $\hat{w}$ to an object with true class w. The assignment is based on the measurement or feature vector $\mathbf{z}$. The set of possible classes is defined by the set of K classes

$$\Omega = \{w_1, \cdots, w_K\} \tag{2.35}$$

In this application, the object class relates to the health status of an EMA. For instance, the health status may be defined by the set $\Omega = \{$ "Healthy - Normal Operation", "Unhealthy - Defective Motor Bearing", "Unhealthy - Screw Defect", $\cdots$, "Unhealthy - Unknown" $\}$. This research uses Bayesian Classification as the health assessment technique. This type of Classifier uses Bayes' Theorem to select the class of an object from a set Ω which are assumed to be mutually exclusive. The class with the minimum amount of risk is the class selected by the Bayesian Classifier. According to Bayes' Theorem, the conditional probability of the object belonging to class w_k is given by

$$p(w_k|\mathbf{z_1}, \cdots, \mathbf{z_N}) = \frac{p(\mathbf{z_1}, \cdots, \mathbf{z_N}|w_k)P(w_k)}{p(\mathbf{z_1}, \cdots, \mathbf{z_N})} \tag{2.36}$$

where $\mathbf{z_1}, \cdots, \mathbf{z_N}$ are the feature variables computed from the feature extraction process. The prior probability that the object belongs to class w_k before any measurements are taken (unconditional) is $P(w_k)$. Since the classes are assumed to be mutually exclusive, the probability of each class must add up to 1:

$$\sum_{k=1}^{K} P(w_k) = 1 \tag{2.37}$$

The term $p(\mathbf{z_1}, \cdots, \mathbf{z_N}|w_k)$ is the prior conditional probability density of $\mathbf{z_1}, \cdots, \mathbf{z_N}$ given that the object belongs to class w_k. Conversely, the probability $p(\mathbf{z_1}, \cdots, \mathbf{z_N})$ represents the density of the feature variables with unknown class. The unconditional density $p(\mathbf{z_1}, \cdots, \mathbf{z_N})$ is related to the conditional densities $p(\mathbf{z_1}, \cdots, \mathbf{z_N}|w_k)$ and the prior probability $P(w_k)$, by

$$p(\mathbf{z_1}, \cdots, \mathbf{z_N}) = \sum_{k=1}^{K} p(\mathbf{z_1}, \cdots, \mathbf{z_N}|w_k)P(w_k) \tag{2.38}$$

The conditional risk associated with selecting class w_k given the feature variables is

$$R(\hat{w}_i|\mathbf{z_1}, \cdots, \mathbf{z_N}) = \sum_{k=1}^{K} C(\hat{w}_i|w_k)p(w_k|\mathbf{z_1}, \cdots, \mathbf{z_N}) \tag{2.39}$$

In this equation, the cost function $\mathbf{C}(\hat{w}_i|w_k)$ is the penalty of assigning the class $\hat{w}_i$ coming from an object with true class w_k. The decision function which minimizes the risk is expressed by

$$\hat{w}_{BAYES}(\mathbf{z_1}, \cdots, \mathbf{z_N}) = \underset{w\epsilon\Omega}{\operatorname{argmin}}\{R(\hat{w}_i|\mathbf{z_1}, \cdots, \mathbf{z_N})\} \tag{2.40}$$

which selects the class w_i that minimizes the argument in brackets from the set of possible classes $w\epsilon\Omega$. Substituting Equations 2.39 and 2.36 into Equation 2.40, yields

$$\hat{w}_{BAYES}(\mathbf{z_1}, \cdots, \mathbf{z_N}) = \underset{w\epsilon\Omega}{\operatorname{argmin}}\{\sum_{k=1}^{K} C(w|w_k)p(\mathbf{z_1}, \cdots, \mathbf{z_N}|w_k)P(w_k)\} \tag{2.41}$$

2.2.1 Single Vector Bayesian Classification

In this research the feature variables are lumped into a single vector, $\mathbf{z} = [z_1, z_2, \cdots, z_N]$. Thus Bayes' Theorem can be re-written as

$$p(w_k|\mathbf{z}) = \frac{p(\mathbf{z}|w_k)P(w_k)}{p(\mathbf{z})} \tag{2.42}$$

and the classifier decision function becomes

$$\hat{w}_{BAYES}(\mathbf{z}) = \underset{w\epsilon\Omega}{\operatorname{argmin}}\{\sum_{k=1}^{K} C(w|w_k)p(\mathbf{z}|w_k)P(w_k)\} \tag{2.43}$$

Assuming the conditional density, $p(\mathbf{z}|w_k)$ is normally distributed, it may be expressed by the parametric equation

$$p(\mathbf{z}|w_k) = \frac{1}{\sqrt{(2\pi)^D|\mathbf{S}_k|}} \exp\left(-\frac{1}{2}(\mathbf{z}-\mu_k)^T\mathbf{S}_k^{-1}(\mathbf{z}-\mu_k)\right) \tag{2.44}$$

The parameters, μ_k and $\mathbf{S}_k$ represent the expectation vector (mean) and covariance matrix, respectively, of the random feature vector $\mathbf{z}$ coming from an object with class w_k. Assuming that the mean and covariance matrix are unknown, they may be estimated from training set data by Equations 2.45 and 2.46, respectively.

$$\hat{\mu}_k = \frac{1}{N_k}\sum_{n=1}^{N_k}\mathbf{z}_n \tag{2.45}$$

$$\hat{\mathbf{S}}_k = \frac{1}{N_k - 1}\sum_{n=1}^{N_k}(\mathbf{z}_n - \hat{\mu}_k)(\mathbf{z}_n - \hat{\mu}_k)^T \tag{2.46}$$

The term N_k represents the number of training samples coming from class w_k.

Consider a two class problem, $\Omega\epsilon\{w_1, w_2\}$, with a feature vector containing two elements, $\mathbf{z} = [z_1, z_2]^T$. A training set of 1000 samples are obtained

from each of the two classes resulting in the data shown in Figure 2.12. Note that the data from both classes form two regions in the space $[z_1, z_2]$ but have some overlap. The data is assumed to behave according to a normal distribution described by the parameters $\mu_{\mathbf{k}}$ and $\mathbf{S_k}$ (Equation (2.44)). The mean and covariance parameters may be obtained from the training set data according to Equation (2.45) and (2.46), respectively.

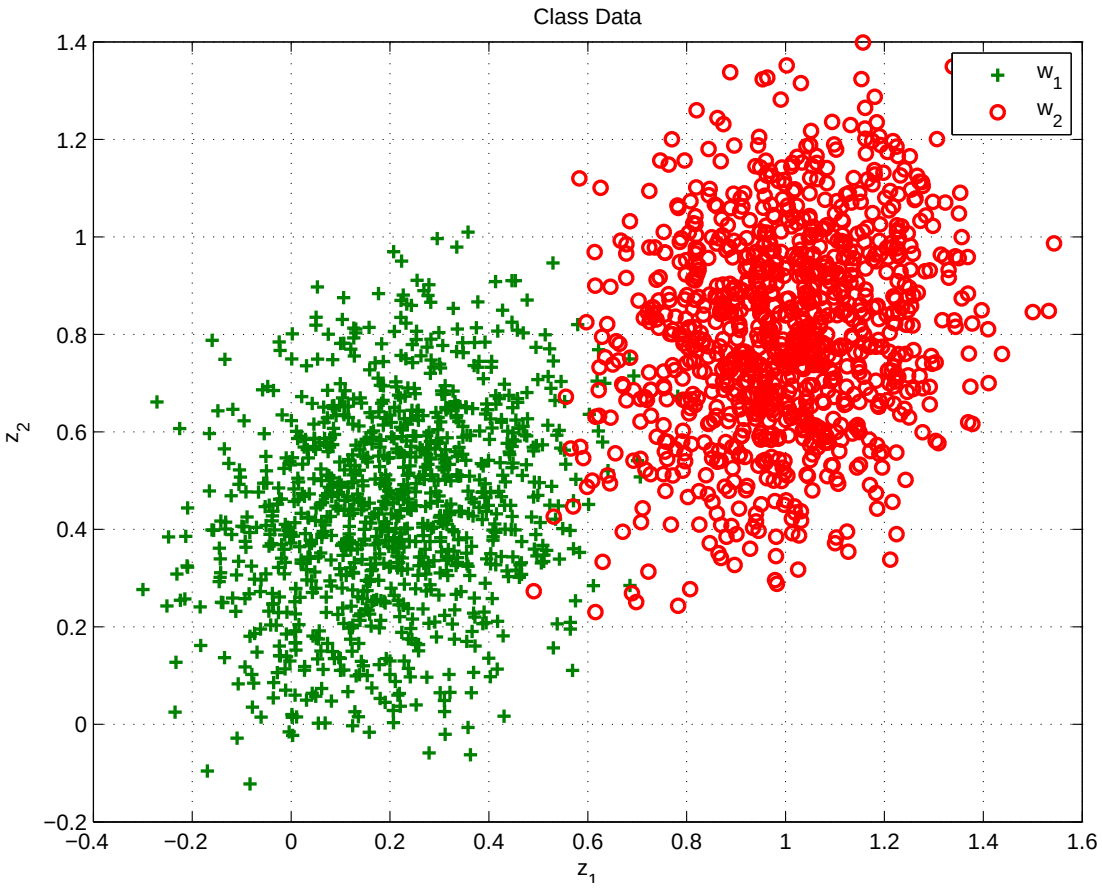

Figure 2.12: Principal Component Plot of Training Set Data for Classification Example

For the example it is assumed that there is an equal probability of selecting an object from either class resulting in equal prior probabilities: $P(w_1) = P(w_2) = 0.5$. In addition the identity cost matrix is applied which assigns a penalty of 1 for a misclassification and a penalty of zero for

a correct classification

$$\mathbf{C} = \begin{bmatrix} 0 & 1 \\ 1 & 0 \end{bmatrix} \tag{2.47}$$

Applying Equation 2.41 to each of the training samples results in the decision boundaries shown in Figure 2.13. This results in 12 out of 1000 samples incorrectly classified as w_1 and 11 out of 1000 samples incorrectly classified as class w_2. The mis-classifications are attributed to the overlap of data in the two classes.

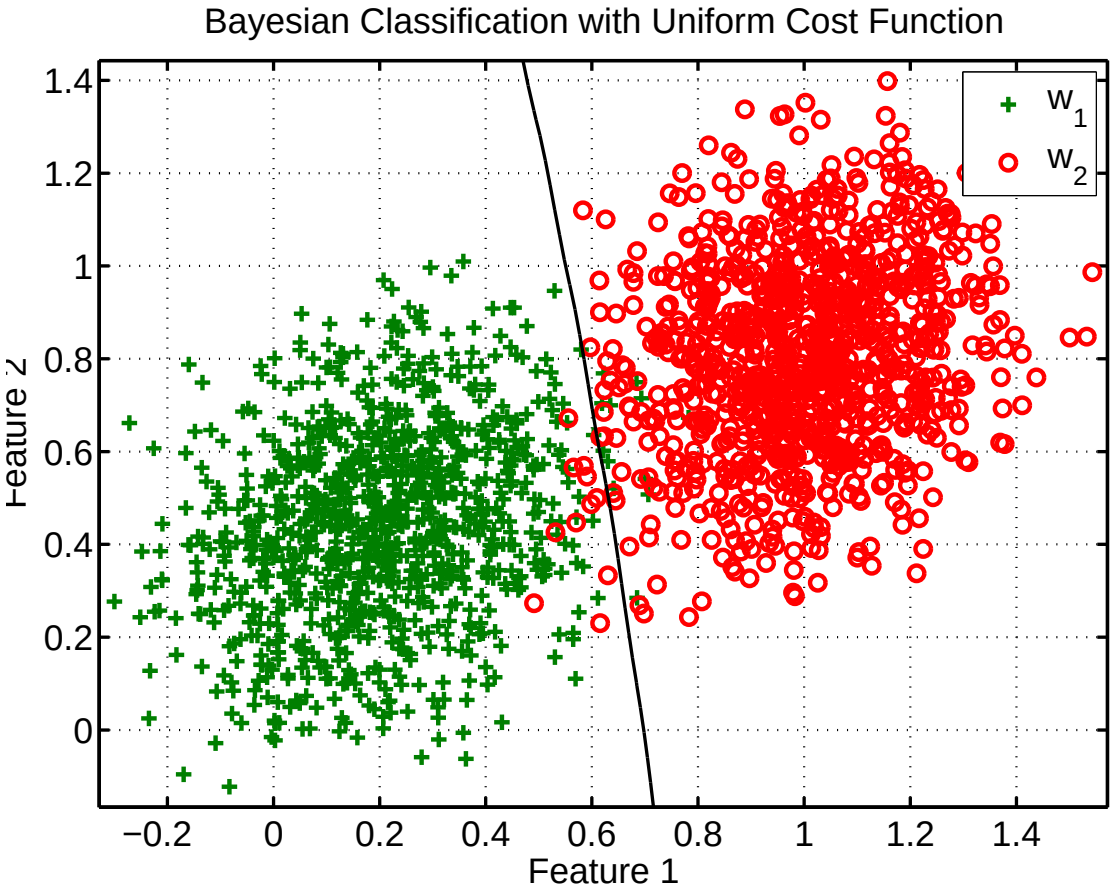

Figure 2.13: Bayesian Classification with Uniform Cost Function

Suppose that the cost matrix is modified so that there is a higher penalty

for selecting class w_2 when the true class is w_1:

$$\mathbf{C} = \begin{bmatrix} 0 & 10 \\ 1 & 0 \end{bmatrix} \tag{2.48}$$

The new decision boundary is shown in Figure 2.14 which results in only 2 out of 1000 samples misclassified as w_1, but 36 out of 1000 samples misclassified as w_2.

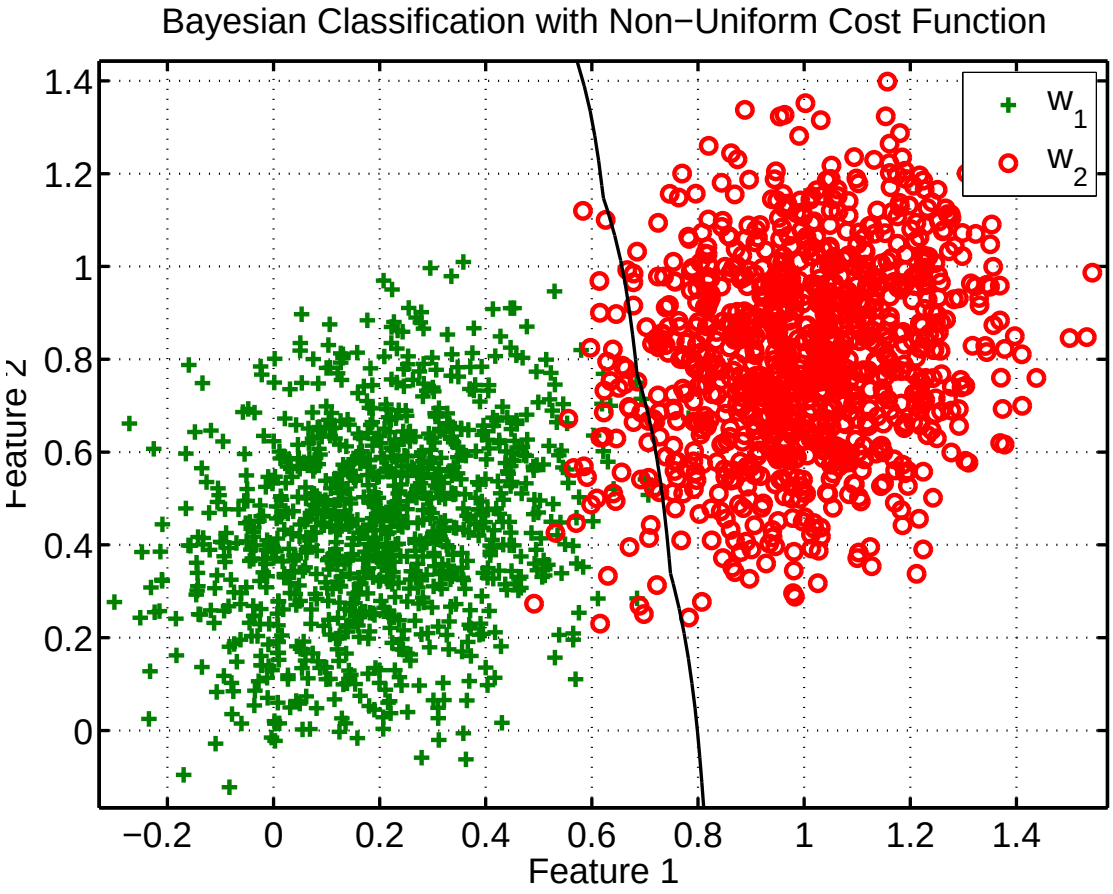

Figure 2.14: Bayesian Classification with Non-uniform Cost Function

Viewing the class w_1 as coming from an object that is "normal/healthy" and w_2 as "abnormal", these two examples demonstrate that (1) Overlap between classes will result in incorrect classifications and (2) The cost function

allows a trade off between missed detections (classified as normal when was truly abnormal) and false alarms (classified as abnormal when was normal).

Chapter 3

Simulation

In this section, the feature extraction and fault classification approach is demonstrated with simulated data. The data is generated for what will be considered a normal/healthy data set and from two other data sets with distinct fault frequency components. The signals are constructed to be similar to what would be expected from a motor current signal for a typical EMA with a Brushless Permanent Magnet Synchonous Motor (PMSM).

Consider the following fabricated motor velocity signal, ω_m, which is sinusoidal with a frequency of 5 Hz and a range of 0 to 40π rad/sec (1200 RPM) and the associated motor angle, θ_m:

$$\omega_m(t) = 20\pi\left(1+\sin(2\pi 5t)\right) \tag{3.1}$$

$$\theta_m(t) = 20\pi t - 2\cos(2\pi 5t) \tag{3.2}$$

Let a corresponding EMA current signal, x, be made up of three parts: (1) a fundamental signal, x_f which is characteristic of both a normal/healthy system and one in the presence of a defect. (2) A defect signal, x_d that is periodic with motor velocity, and (3) a normally distributed noise signal, x_n. The signal is represented by Equation (3.3):

$$x = x_f + x_d + x_n \tag{3.3}$$

where:

$$x_f = 5\sin(6\theta_m) + 0.1\sin(2\pi 100t) \tag{3.4}$$

$$x_d = \begin{cases} 0 & Healthy \\ 0.1\sin(3.125\theta_m) & Defect1 \\ 0.1\sin(10.5\theta_m) & Defect2 \end{cases} \tag{3.5}$$

$$x_n \sim \mathbf{N}(0, .25) \tag{3.6}$$

The individual and composite signals for the healthy and defective signals are simulated with a sampling frequency of 2 kHz and are shown in Figures 3.1, 3.2, and 3.3, respectively over a one second interval.

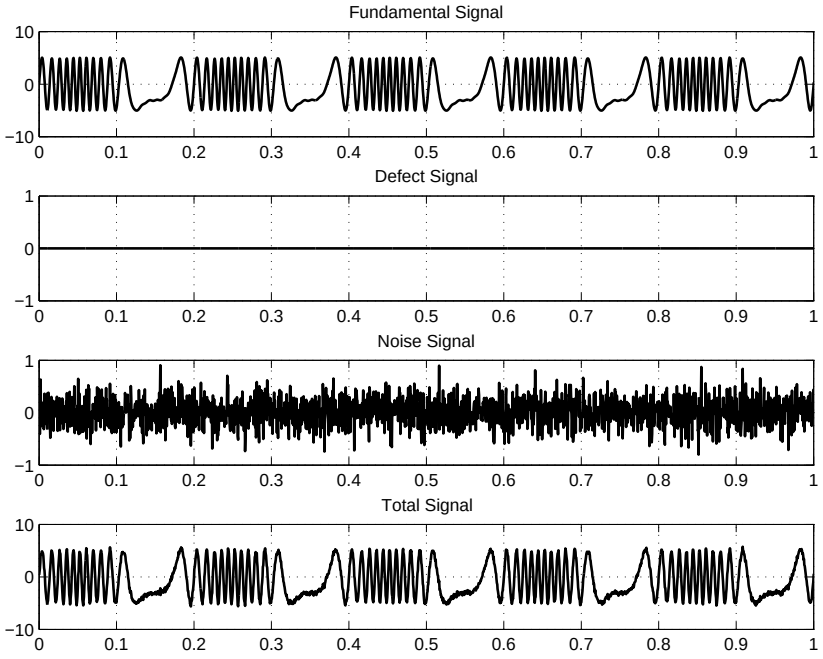

Figure 3.1: Healthy Generated Data

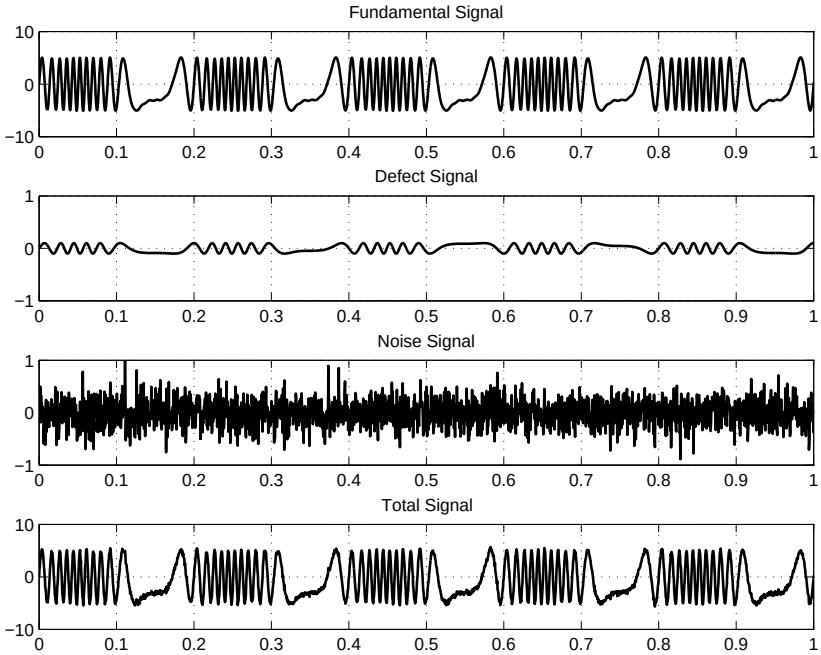

Figure 3.2: Defect 1 Generated Data

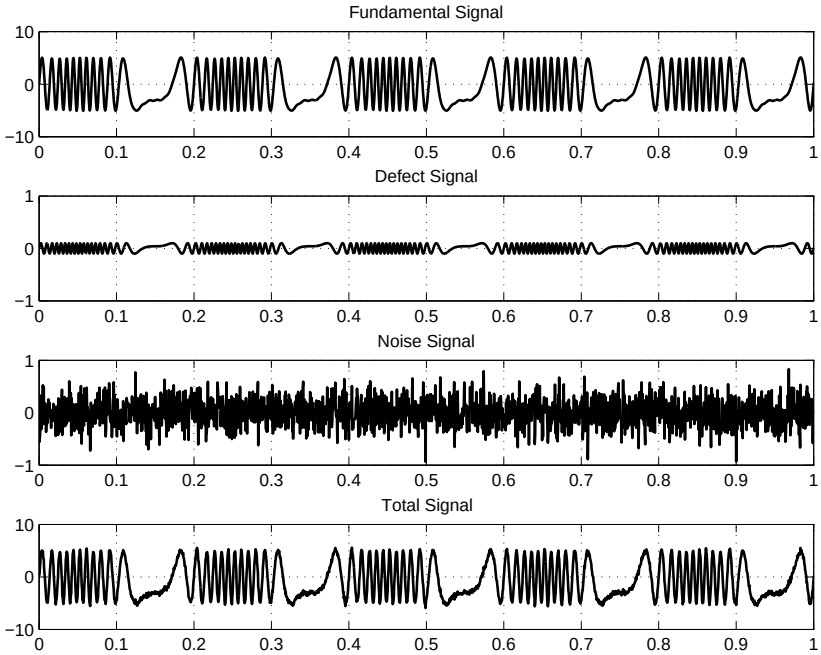

Figure 3.3: Defect 2 Generated Data

3.1 Feature Extraction

The PSD of the composite signal is computed prior to and after resampling and is shown in Figure 3.4. The PSD prior to resampling was computed using a single Hanning window of 4096 points, resulting in a frequency resolution of 0.49 Hz. In this case, the PSD does not appear to be different between the healthy and defective signals. This is due to the fundamental frequency being a multiple of the motor speed which spreads the frequency content of the signal over the frequency range. Since the fundamental signal dominates, the defective frequency (which is also spread over the frequency range) is not apparent.

The re-sampled signals were computed with a sampling interval of $\theta_s = 0.001$ revolutions per sample (1000 samples per revolution). In this case the PSD was computed using a single Hanning window of 2^{14} points, resulting in a frequency resolution of 0.06 orders. The fundamental signal appears at 6 orders for the healthy and defective signals as expected. In addition, the defective components can also been seen for defect 1 (3.1 orders) and defect 2 (10.5 orders), from Equation 3.5.

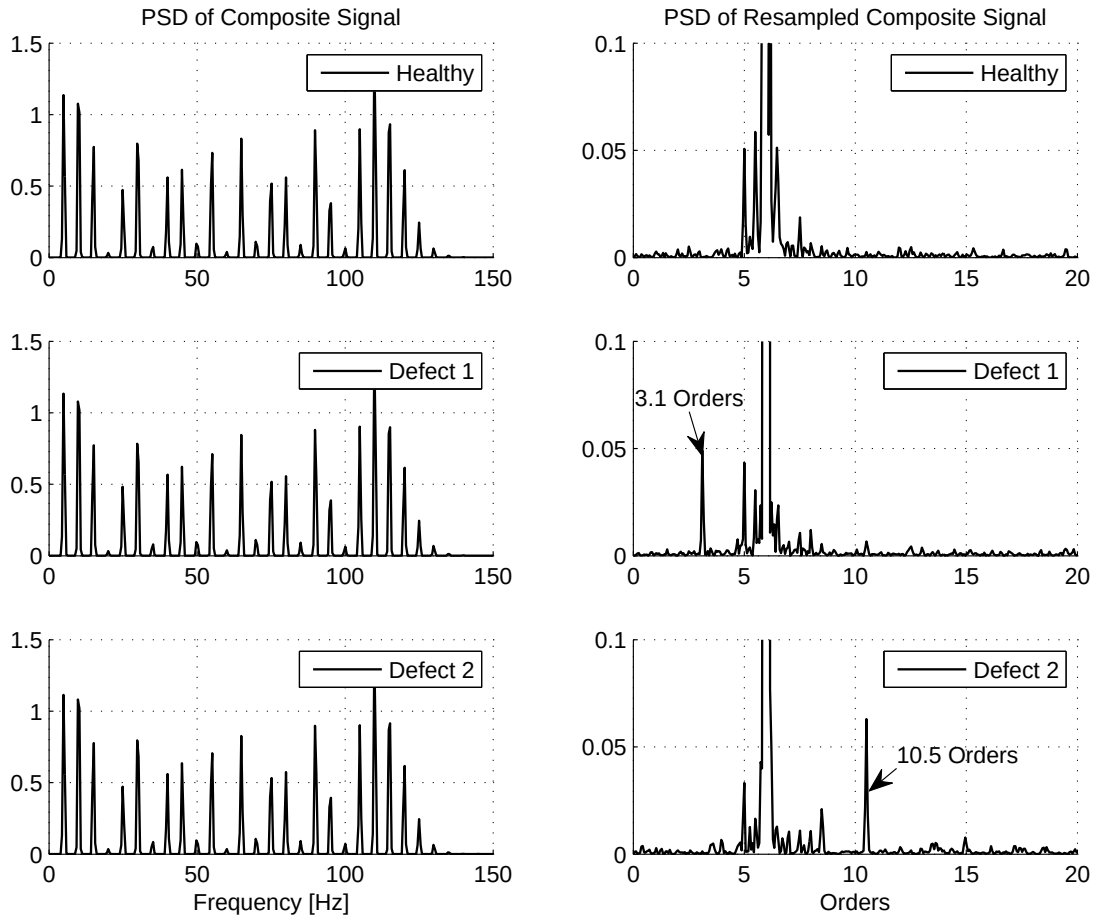

Figure 3.4: Simulated PSD Comparisons. Left - prior to resampling. Right - after resampling

Since the signal contains a fundamental component of 6 orders, an ideal bandpass filter is utilized with a stop band from 5.6 to 6.4 Orders to account for leakage. Next the re-sampled PSD is grouped into bins of size $\delta b = 1$ orders over the range of 0 to 50 orders ($N_b = 50$), and the remaining orders are discarded. The filtered PSD and the binned PSDs are shown in Figure 3.5.

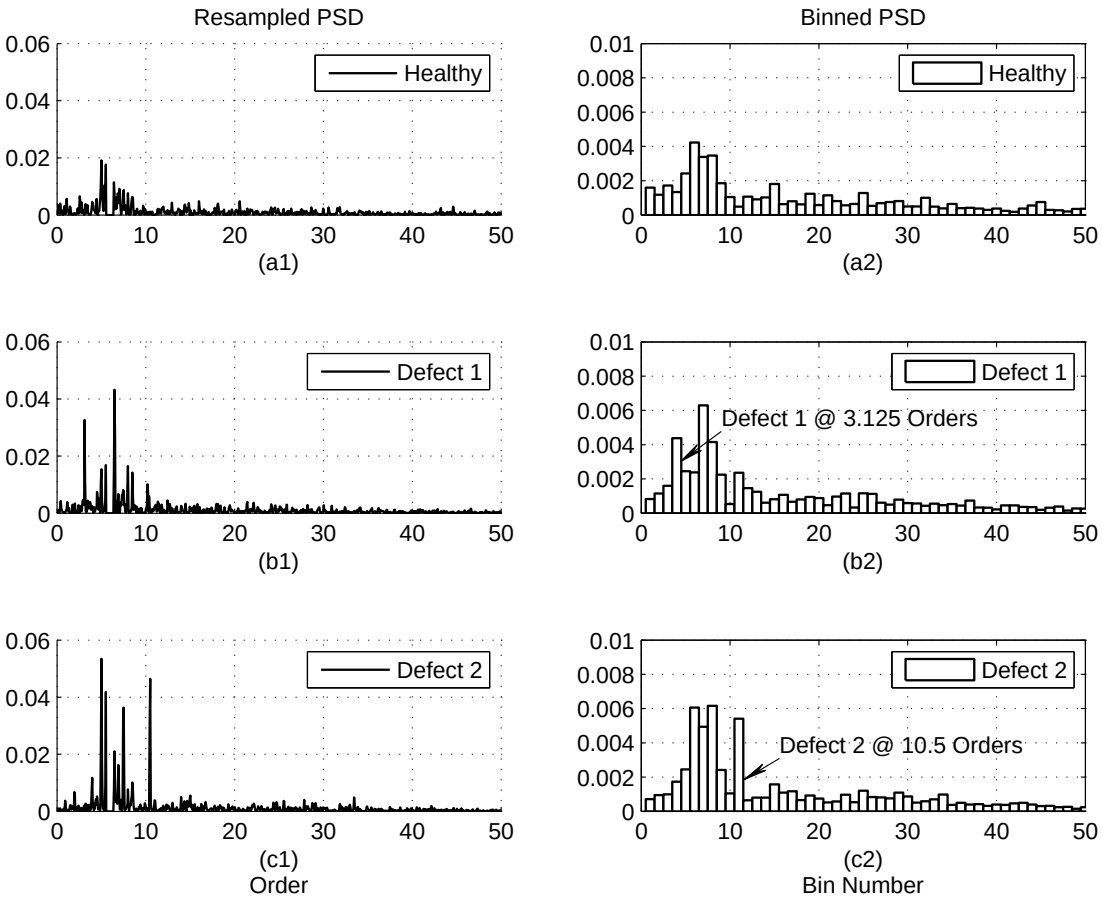

Figure 3.5: Simulated PSD Comparisons. Left - Resampled PSD. Right - Binned PSD

The binned data must be transformed to a lower dimensional space through the transformation matrix $\mathbf{W}$. The matrix is obtained by forming a training set matrix, $\mathbf{T}$ consisting of multiple runs of data for each of the three data sets and then performing the PCA on the training set matrix. For the simulation, a total of 40 sets of data is generated for each of the three signals - Healthy, Defect 1, and Defect 2. This results in a training set matrix of size 120 x N_b. The PCA results in 50 eigenvalues and 50 eigenvectors. The contribution of each eigenvector to the total variance in the training set can be determined by the size of the eigenvalues. The percent contribution of each eigenvector to the total variance is shown in Figure 3.6.

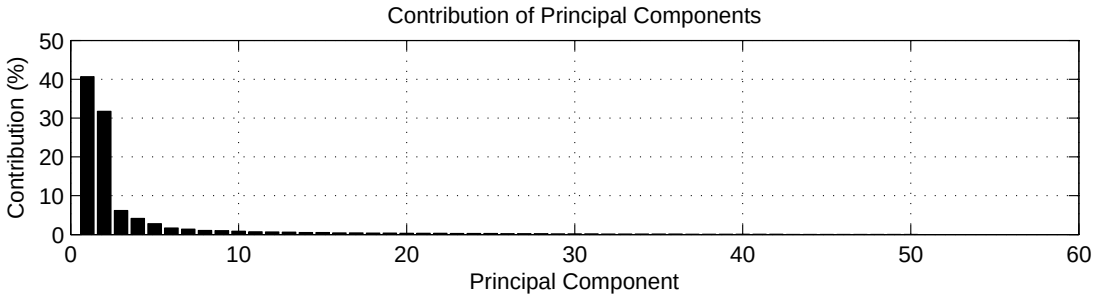

Figure 3.6: Principal Component Contributions to Total Training Set Variance

The first two principal components account for about 72% of the total variance so the remaining 48 principal components are discarded. The magnitude of the eigenvector components give an indication of the relative importance of the bins to each principal component. The percent contribution of each bin to the principal component for the first two principal components are shown in Figure 3.7

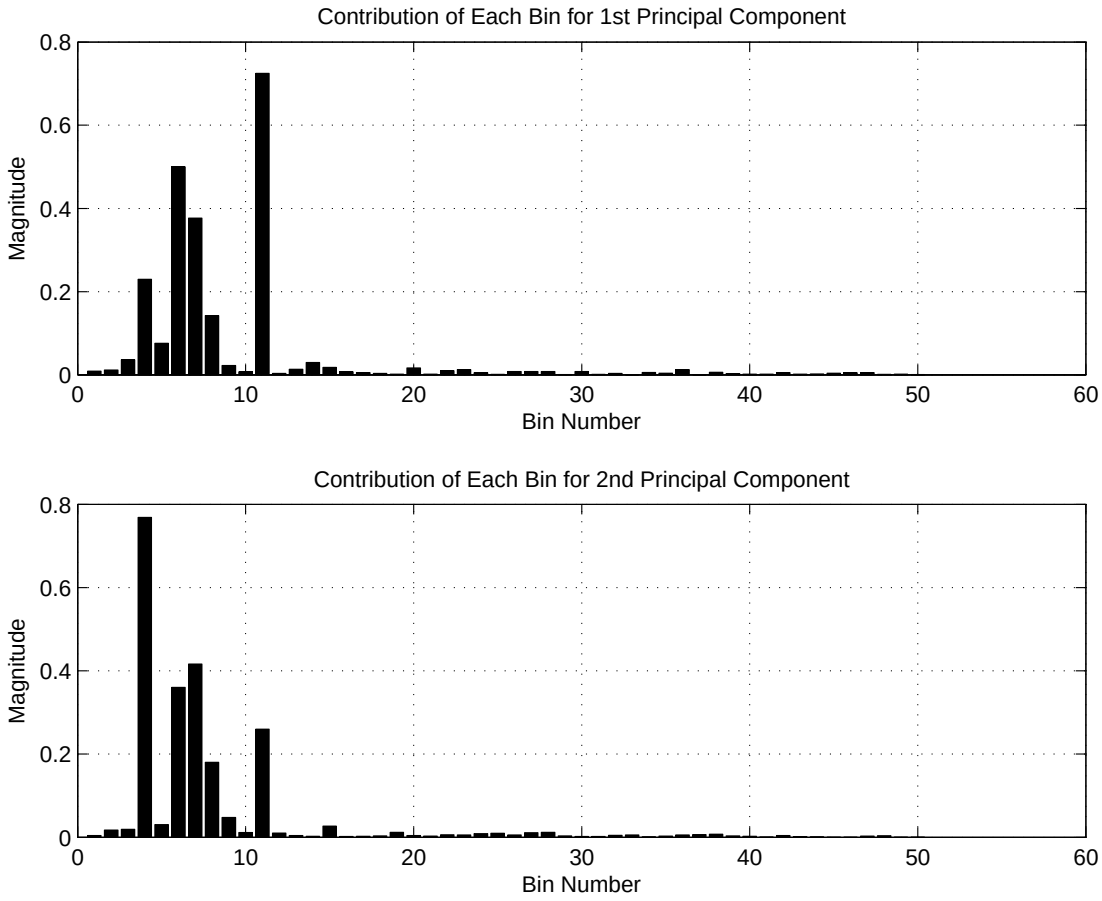

Figure 3.7: Eigenvector Magnitudes for the First Two Principal Components

The largest contributing bin to the first principal component is the 11th bin (0.72). This bin has a range from 10 to 11 orders and contains defect 2 (10.5 orders). Bin number 4 is the largest contributor to the second principal component (0.77), having a range of 3 to 4 orders, thus containing defect 1 (3.125 orders). This result is expected since the values in these bins will be larger when the defect is present, creating a larger variance in the training set. Note that bins 6, 7, and 8 are also moderate contributors to each principal component. This is likely due to the leakage of the fundamental component into neighboring bins. The contribution of these bins may be reduced by using a different windowing function or increasing the stop band

range of the filter. However, the filter stop band range must not be so wide as to cancel out the orders containing the defects.

Since the first two principal components were selected, the transformation matrix $\mathbf{W}$ is 50×2. Multiplying the bin values by the transformation matrix for each of the training set runs reduces the feature vector from $N = 50$ to $D = 2$ components and results in the scatter plot shown in Figure 3.8. The class of each data point is indicated in the figure and shows that each class largely occupies a distinct region in the feature space. The defect 1 training set population mainly occupies the upper left portion of the space since the order of defect 1 was the main contributor to the second principal component (y axis). Likewise, the defect 2 training set population occupies the far right hand side of the plot since the main contributor for this defect was the first principal component (x axis). The healthy samples mainly populate the lower left region, but some samples do spread out between the defect 1 and 2 populations. The distinctive regions is a desired result since it will enhance classifier accuracy.

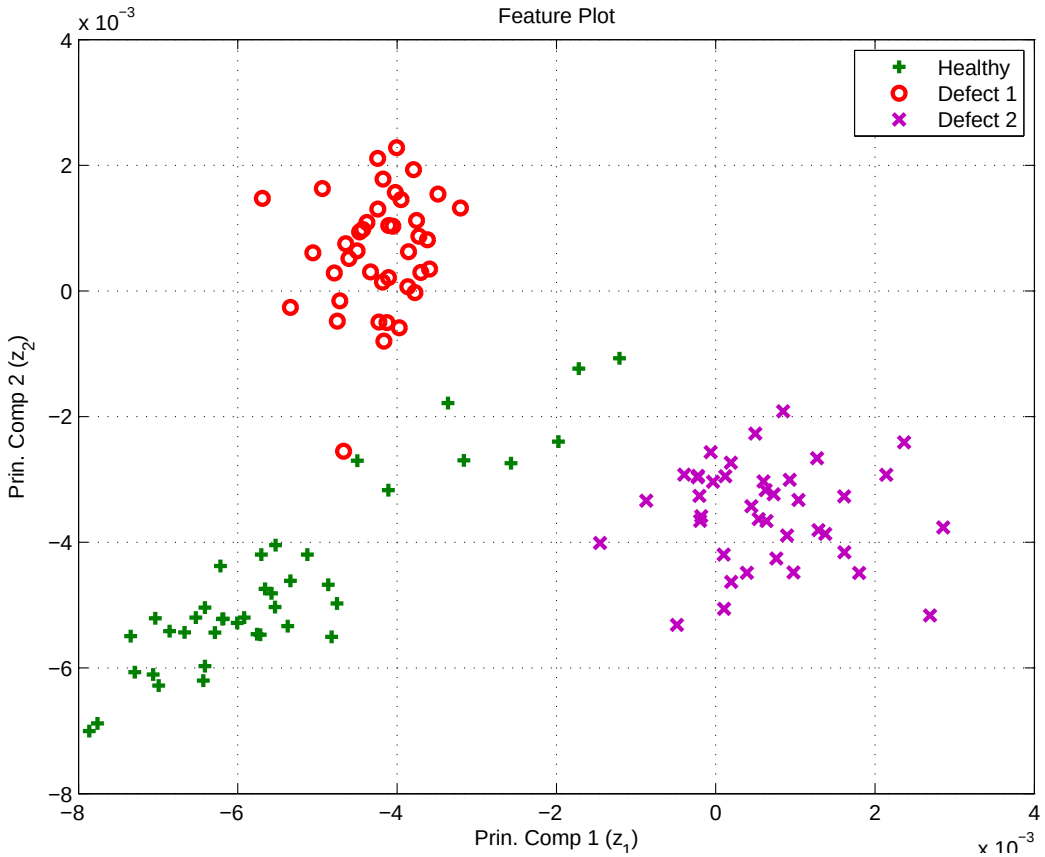

Figure 3.8: Feature Plot of Simulated Training Set Data

3.2 Classification

The feature data obtained in the previous section is used to determine whether the data is healthy or contains defect 1 or defect 2. This is done using the Bayesian Classification approach presented in Chapter 3. In order to perform the Bayesian algorithm, two probabilities must be determined: $P(w_k)$ and $P(\mathbf{z}|w_k)$. For the simulation there is equal probability of having a signal that is healthy, or contains defect 1 or defect 2. As a consequence the prior probabilities are set equal:

$$P(w_1) = P(w_2) = P(w_3) = 1/3 \tag{3.7}$$

The subscripts 1, 2, and 3 denote Healthy, Defect 1, or Defect 2, respectively. The conditional density, $p(\mathbf{z}|w)$ is determined using parametric learning where it is assumed that the distribution is gaussian with unknown parameters μ_k, and $\mathbf{S}_k$. The parameters are determined from the training set data using Equations 2.45 and 2.46. Two dimensional contour plots of the prior probability densities for the training set data are shown in Figure 3.9.

The Bayesian Classifier predicts the class of an object by assigning the class with the minimum risk according to Equation 2.41. Using a uniform cost function results in the decision boundaries shown in Figure 3.10. The feature extraction method combined with the Bayesian Classification results in Bayes decision boundaries that appear to accurately classify the three healthy class types for the training set data. 100% of the healthy and defect 2 samples are correctly isolated, and 39/40 or 97.5% of the defect 1 samples are correctly classified. The one mis-classified defect 1 sample was classified as healthy.

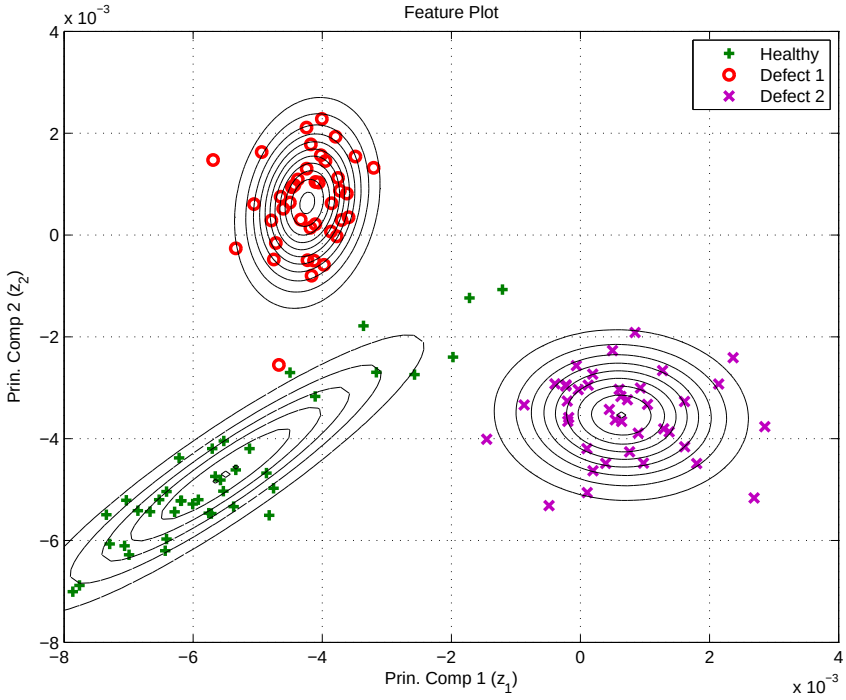

Figure 3.9: Simulated Data Feature pdf Contour Plot of Training Set Data

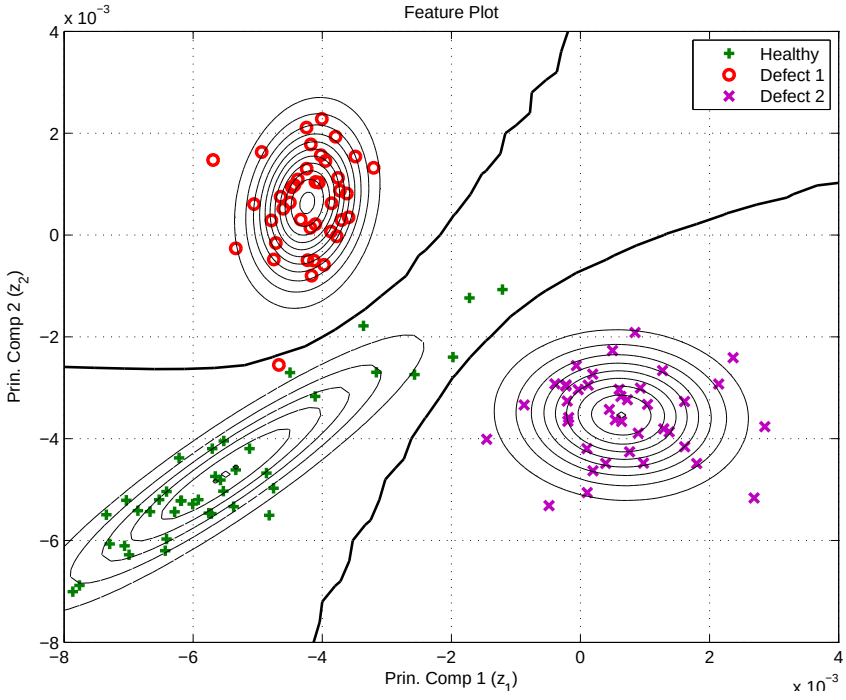

Figure 3.10: Simulated Data Bayes Classifier Boundaries

Chapter 4

Test Demonstration

The approach presented in Chapter 2 and demonstrated in Chapter 3 will now be applied using data from two Moog Industrial Max Force EMAs in a laboratory environment. The first EMA is considered normal/healthy and the other (which will be referred to as the degraded EMA) has an angular contact bearing with an inner ring defect and 75% of the normal grease applied to it. The corresponding mechanical defect frequency for the inner ring defect is $f_{IR}/f_r = 6.123$. The objective is to show whether the proposed health monitoring architecture is capable of distinguishing between the two EMAs when tested over a range of operating conditions.

This section is organized as follows: First, a description of the Max Force EMA and the major sub-assemblies that are critical to its operation are given. This is followed by a description of the test system and the environment in which data is collected. This description includes the test fixture, sensors, signal conditioners, and data collection equipment. Next, the test profile used for the data collection on the EMAs is given along with plots showing the sensor output data. Finally, the signal data is transformed using the proposed health monitoring approach and the results are presented and compared using two different training methods.

4.1 EMA Description

Electro-Mechanical Actuators convert electromagnetic energy into mechanical energy to provide a position output. In flight control applications, EMAs may be used to position flight control surfaces for controlling the motion of an aircraft. The Max Force EMA includes a three phase permanent magnet synchronous motor that responds to voltage commands to provide rotational output of a screw rigidly coupled to the rotor. A nut is coupled to the screw by steel balls that circulate along the single race of the screw. Rotational motion of the screw is converted to translational motion by constraining the ball-nut so that it may only traverse along the screw. This translation of the nut provides the output motion of the piston rod. A simplified cross sectional view of the EMA is shown in Figure 4.1 and the EMA specifications are given in Table 4.1. Note that according to Equation (2.3), the fundamental current frequency for this motor is, $f_e/f_r = 6$. The key sensing element inherent to the EMA is a resolver for sensing motor angle for feedback control.

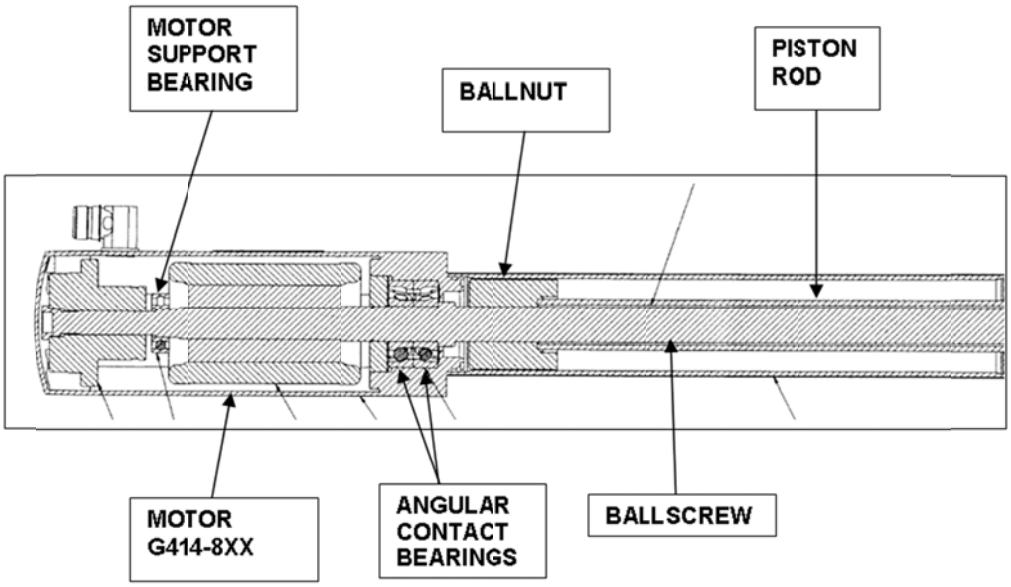

Figure 4.1: Max Force EMA Cross Section

Table 4.1: Max Force EMA Technical Specifications

Stroke	6 inches
Force Capability	3700 lbf @ 15.6 Arms
Peak Motor Velocity	4572 RPM at 220 VAC
Number of Motor Poles	12

4.2 Laboratory Setup

The laboratory setup consists of the following elements:

- The EMA itself
- A hydraulic load actuator
- Position and load sensing devices

- A test fixture
- A Moog T200 Motor Controller
- Signal Conditioning Equipment
- A windows based computer with dSpace software and hardware

The EMA is suspended vertically in the test fixture with the piston rod end attached to a rotating clevis near the top of the fixture. The hydraulic load actuator is also suspended vertically and attached at the opposite end of the clevis. The hydraulic load actuator contains an Electrohydraulic Servovalve (EHSV) which is commanded in a closed loop fashion to control the load applied to the EMA. A load cell is included in the test fixture to measure the actuator load. The test fixture with EMA installed is shown in Figure 4.2.

The dSpace computer with Matlab/Simulink is used for implementing the EMA position and load actuator controller, and also provides the data acquisition and signal scaling. Position feedback is provided by an externally mounted LVDT, and the load feedback is accomplished by a differential pressure transducer on the hydraulic load actuator which senses the pressure at the actuator piston. An Accelerometer is mounted to the EMA housing near the degraded motor bearing for vibration measurement. The sampling rate of the data acquisition is set to 48kHz and signal conditioning filters set at 15kHz are used prior to analog to digital conversion for preventing signal aliasing. The position controller outputs a velocity command which is used as the input to the T200 motor velocity controller. The controller uses the resolver and motor phase current feedback signals to produce compensated voltage commands to the motor coil windings. A signal diagram is shown in Figure 4.3 with sensor characteristics listed in Table 4.2.

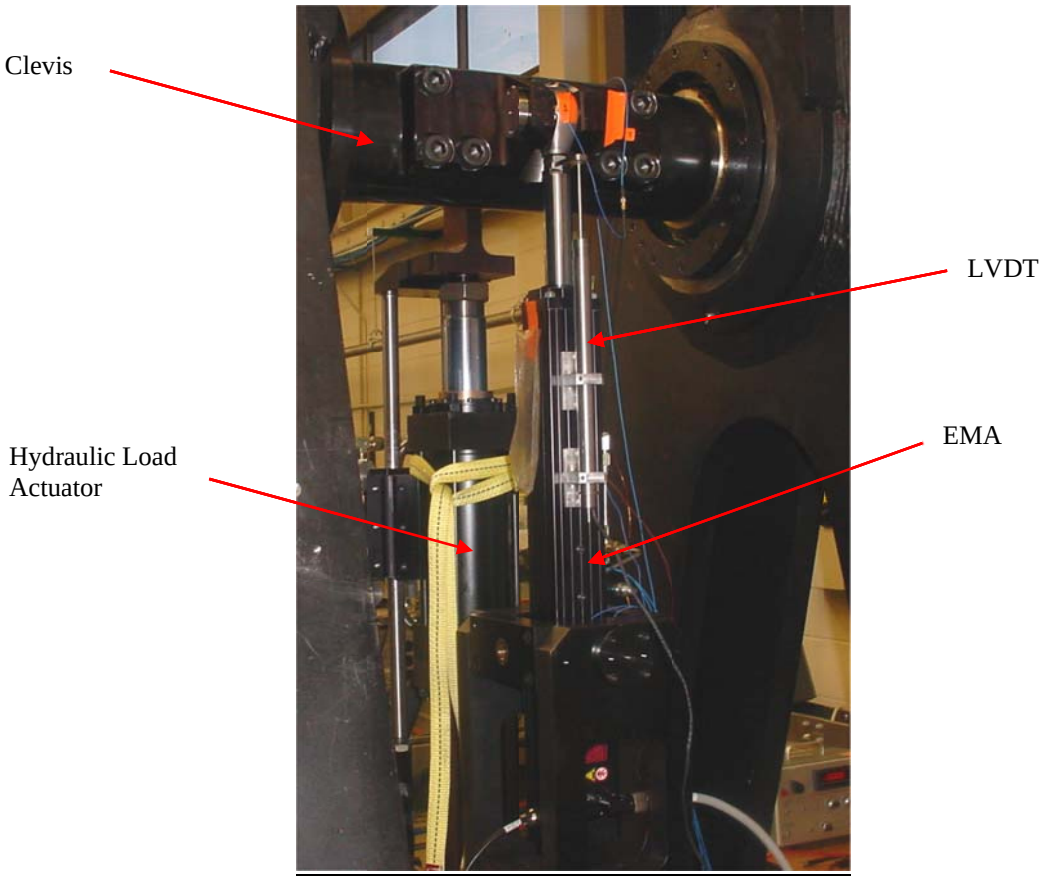

Figure 4.2: EMA Test Fixture

Table 4.2: Transducer Signal Scaling

Transducer	Sensor	Scale	Peak
Accelerometer	PCB 352A24	1 g/Volt	10 g's full scale
Motor Phase Current	LEM LA 25-P	5 Amps/Volt	+/-50 Amps
Load Cell	Model 75 Sensotec	1000 lbs/Volt	+/-5500 lbs Max Test
Motor Velocity	T200 Output	500 RPM/Volt	+/- 4700 RPM
LVDT	Penny Giles	0.5 in/Volt	+/- 3 in

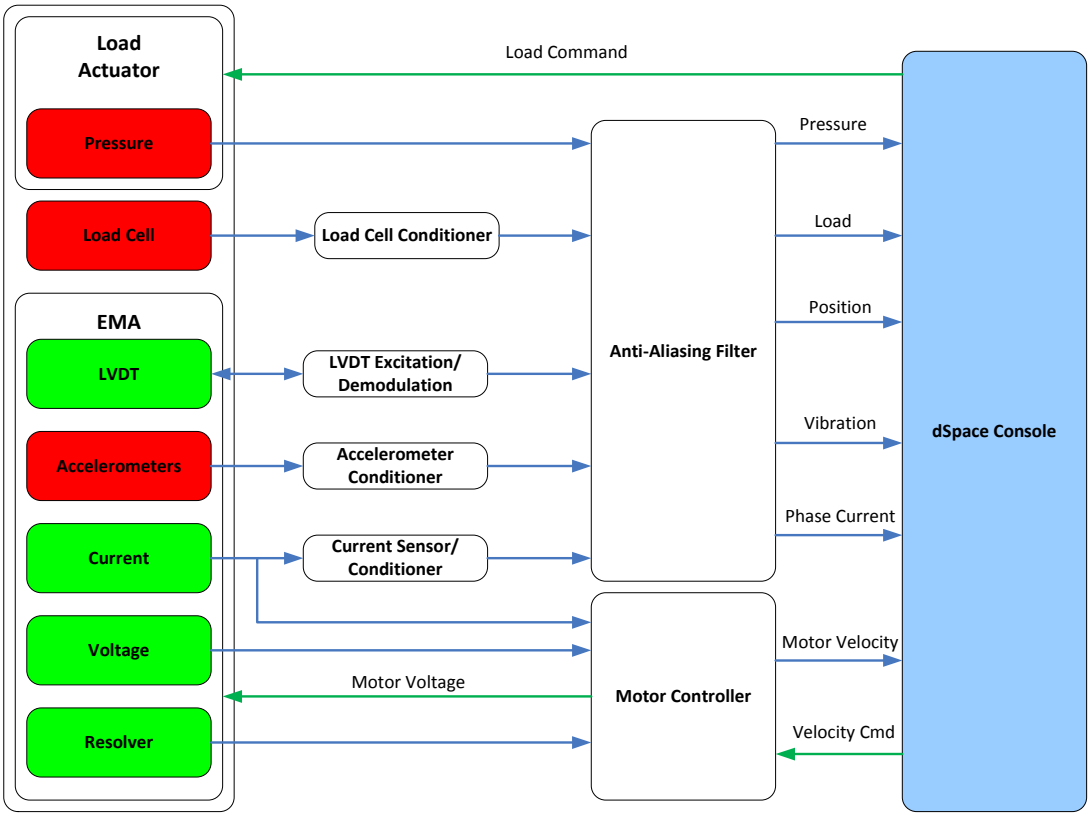

Figure 4.3: EMA Laboratory Signal Diagram

4.3 Results

In order to demonstrate the performance of the health monitoring scheme, data from the EMA is collected over the operating conditions shown in Table 4.3, which are typical of conditions for an Aircraft Spoiler EMA duty cycle scaled for the Max Force EMA. Data is collected from each condition 20 times for both the healthy and degraded EMAs. The first ten data sets for each condition are used for training to obtain the transformation matrix and estimating the parameters of the probability densities for the Bayesian

Classification. The remaining ten data sets are used for validation and testing. Two different training schemes are employed: In the first case training is done on a per condition basis, i.e. training is done separately for each condition so that Bayesian decision boundaries are tailored to the operating condition. This type of training scheme is suitable when the operating condition (e.g. position command and load) is known or when it is possible to determine the operating condition so that the appropriate classifier parameters can be applied. In the second case, training is done by combining the training data for each of the conditions so that only one Bayesian classifier can be used under any operating condition. This type of classification scheme is more suitable when the operating condition is unknown. For each of the test conditions, the parameter settings shown in Table 4.4 are used. The angular sampling period was chosen so that the PSD would contain a maximum of 100 orders and is also small enough to prevent signal aliasing.

The approach will be evaluated separately using the following input signals: motor phase A current, motor bearing housing vibration, motor velocity and EMA position as shown in Figure 4.4. This approach was chosen to assess which signals give the best insight into EMA condition. The results will be displayed for each signal over each operating condition in the following order:

1. Position and Load command and feedback plots
2. Time sampled signal data (LVDT position, motor velocity, motor current, and vibration)
3. Resampled and filtered PSD plots of signal data
4. Binned PSD plots of signal data

5. Feature data scatter plots with Bayesian decision boundaries for condition based training scheme

6. Feature data scatter plots with Bayesian decision boundaries for condition independent training scheme

In items 1-4, the healthy EMA data is plotted first followed by degraded EMA data for one run in each condition. Items 5-6 summarize the final feature data and classification results for both training and test/validation data sets.

Table 4.3: Max Force EMA Test Profile

Condition No.	Actuator Command				Load Command		Data Set Uses	
	Command Type	Bias [in]	Amp. [in]	Freq. Hz	Spring Rate [lbf/in]	Bias [lbf]	Training	Test
1	Sine	1.90	0.10	0.70	0	116	1-10	11-20
2	Triangle	1.40	-0.90	1.00	0	278	1-10	11-20
3	Triangle	0.25	2.05	2.14	0	660	1-10	11-20
4	Sine	0.10	-2.20	0.70	-1210	-1867	1-10	11-20
5	Triangle	1.15	-1.55	0.41	-550	255	1-10	11-20

Table 4.4: Feature Extraction and Classification Parameters

Parameter	Description	Value
θ_s	Spatial Sampling Period	.02 π rad/Sample
δ_b	Bin Size	1 order
$\mathbf{C}(w\|w_k)$	Cost Function	Uniform
$P(w_k)$	Prior Probability	0.5 (Equal)

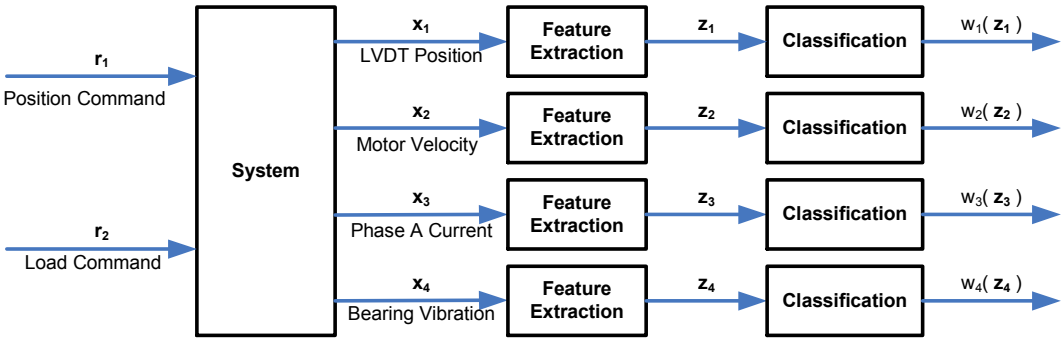

Figure 4.4: EMA Laboratory Fault Detection Scheme

4.3.1 Condition 1

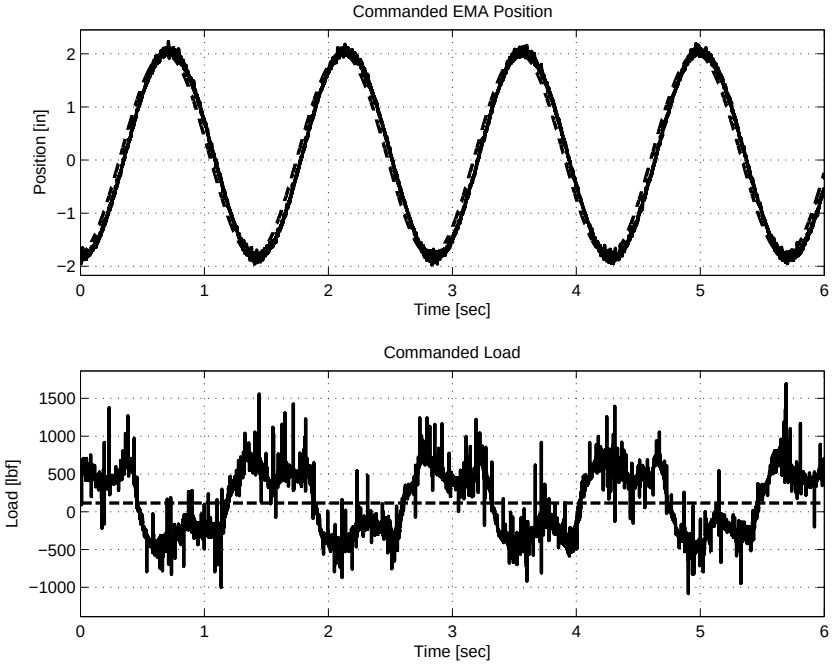

Figure 4.5: Condition 1 Healthy Command Signals.

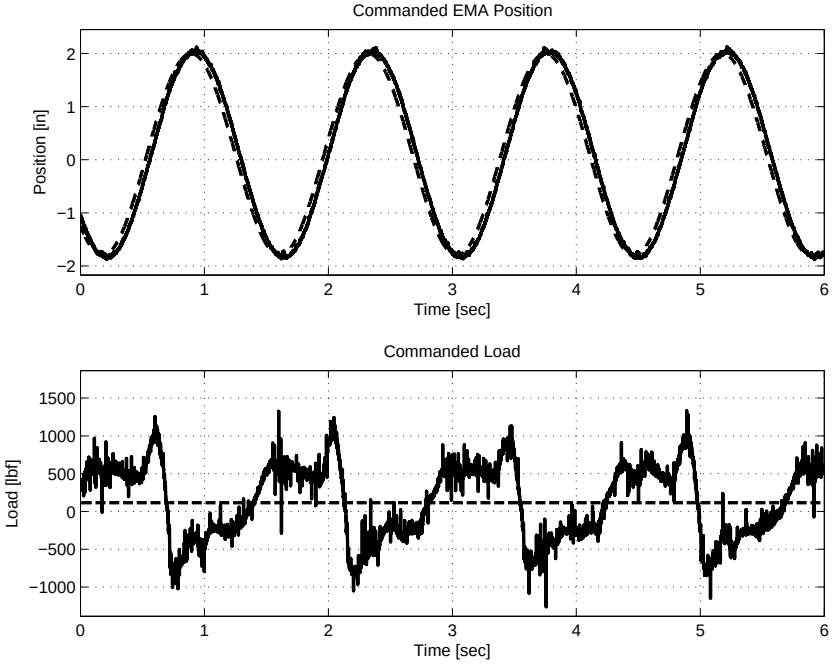

Figure 4.6: Condition 1 Degraded Command Signals.

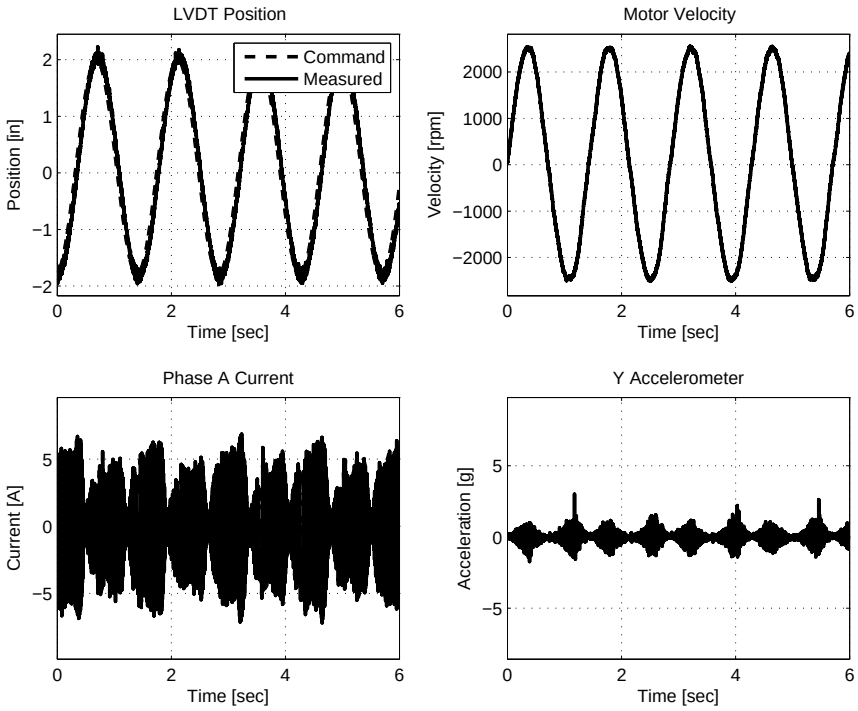

Figure 4.7: Condition 1 Healthy EMA Data.

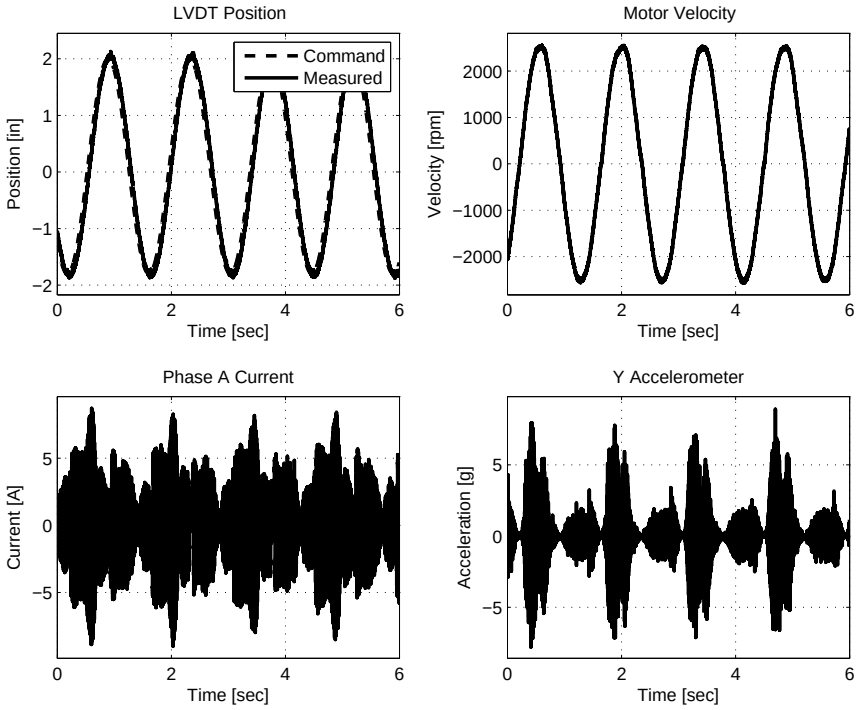

Figure 4.8: Condition 1 Degraded EMA Data.

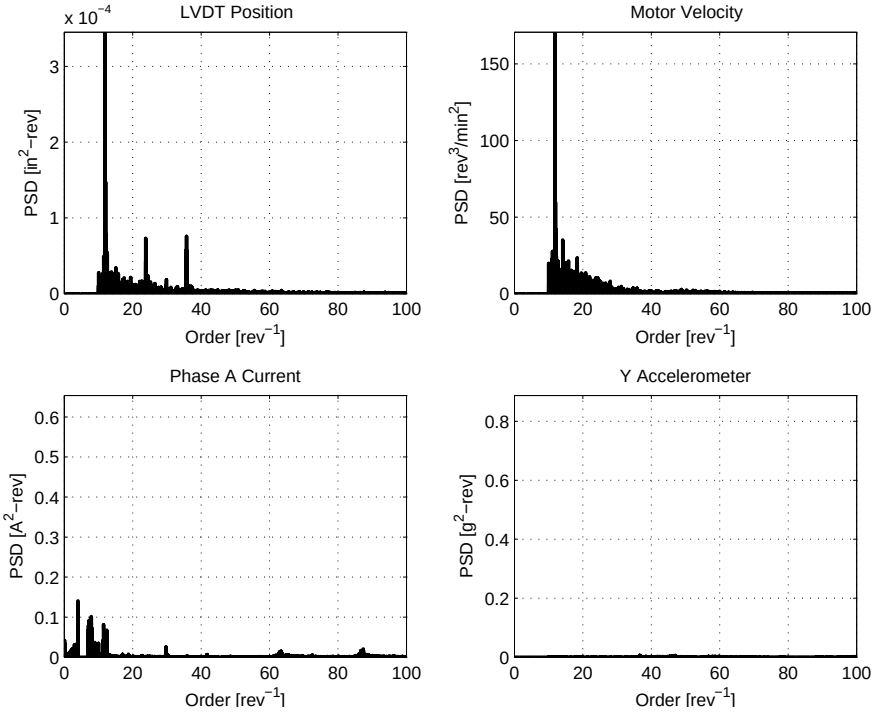

Figure 4.9: Condition 1 Healthy EMA Resampled PSD Data.

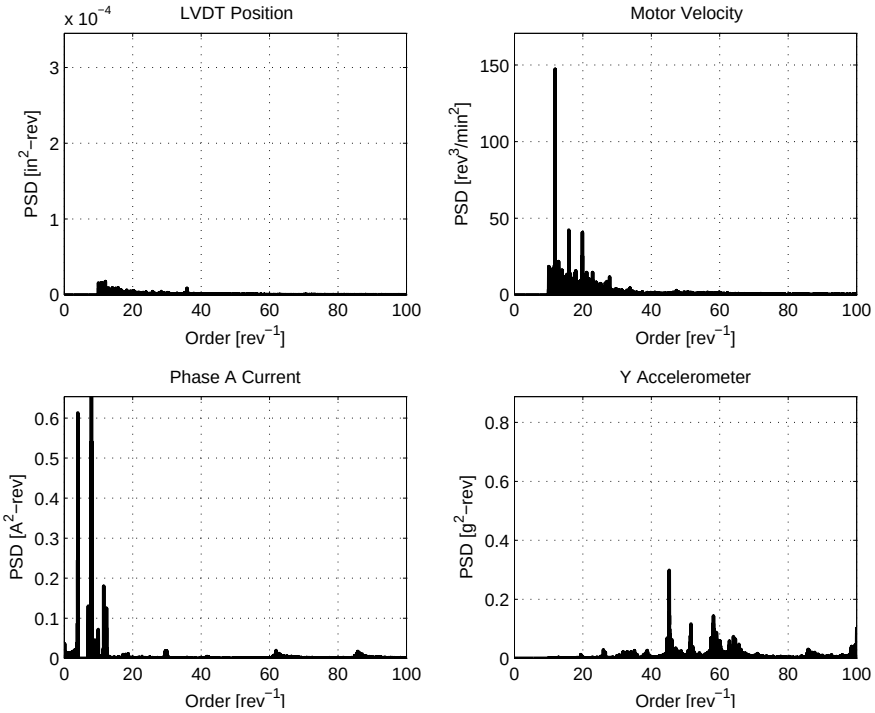

Figure 4.10: Condition 1 Degraded EMA Resampled PSD Data.

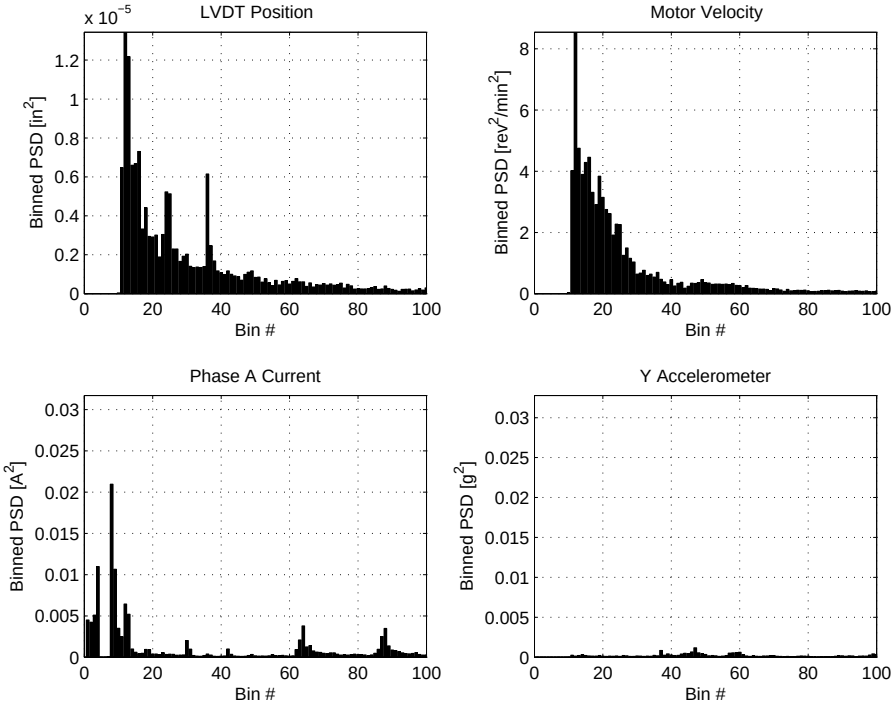

Figure 4.11: Condition 1 Healthy EMA Binned PSD Data.

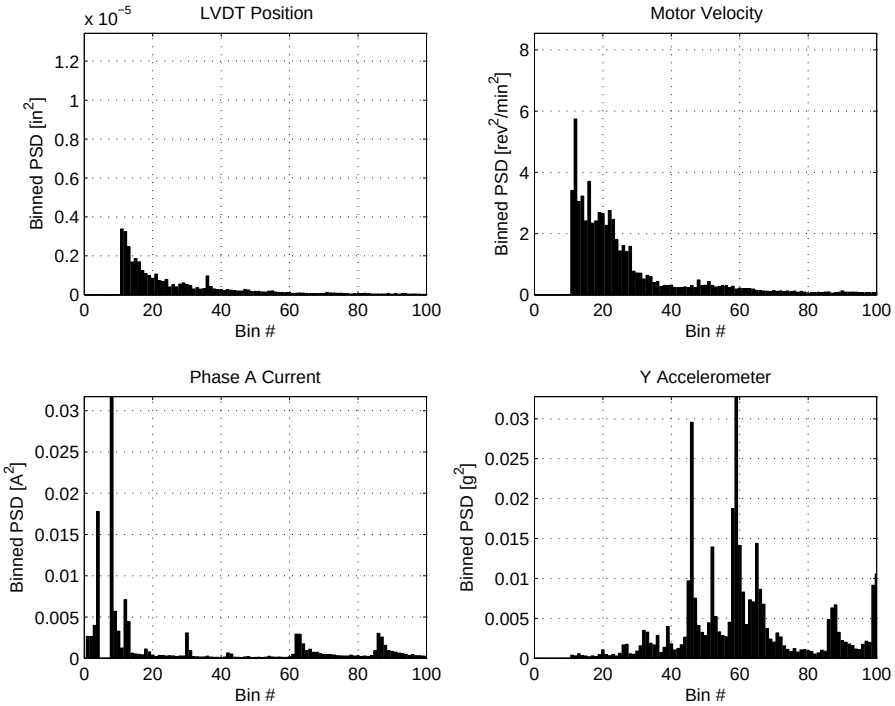

Figure 4.12: Condition 1 Degraded EMA Binned PSD Data.

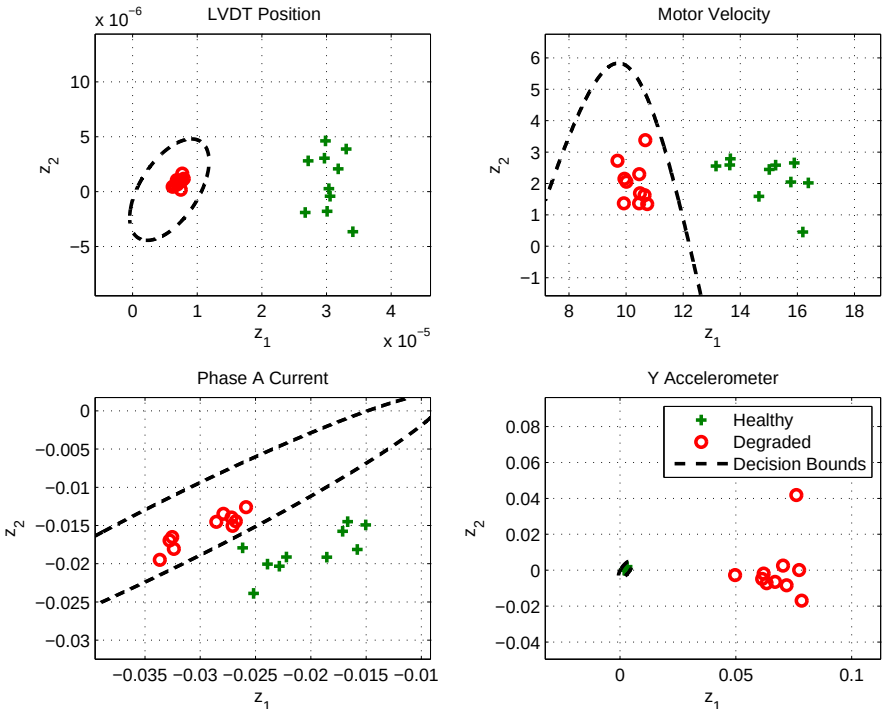

Figure 4.13: Condition 1 Training Set Data Feature Plots - Condition Dependent Training Method

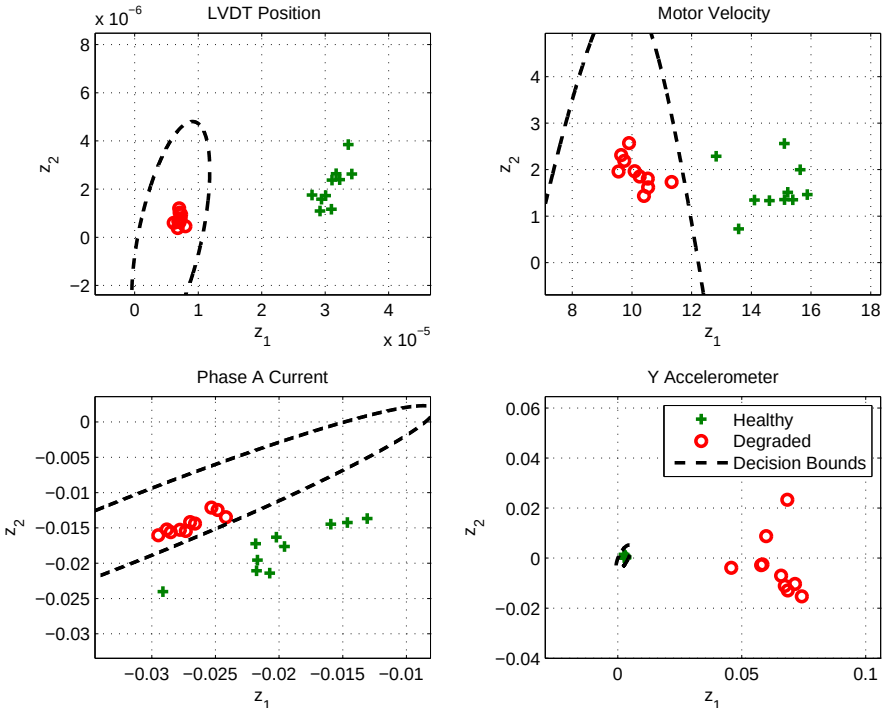

Figure 4.14: Condition 1 Test Set Data Feature Plots - Condition Dependent Training Method

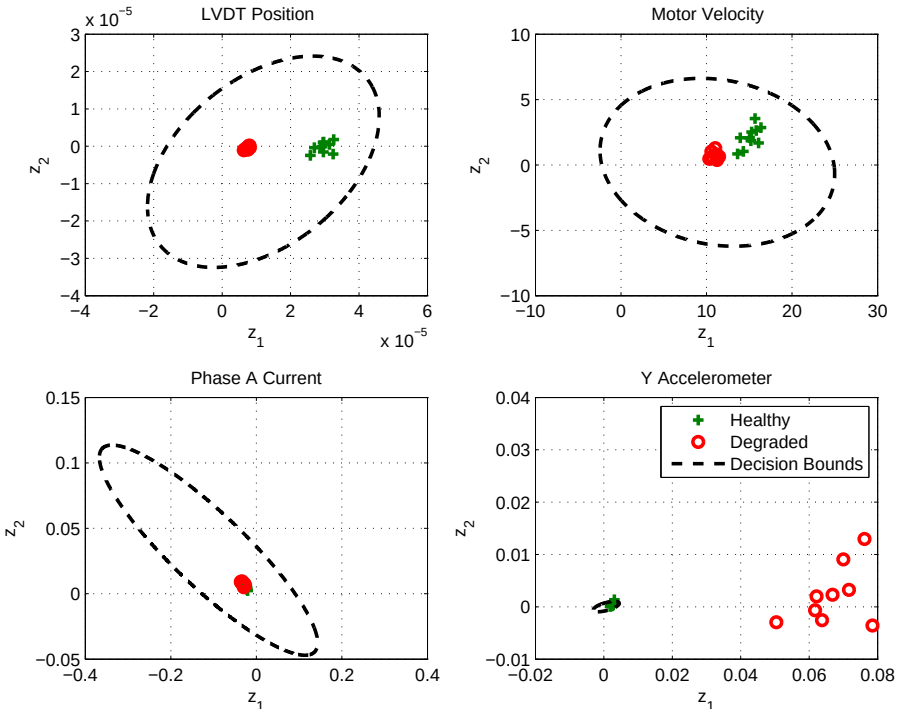

Figure 4.15: Condition 1 Training Set Data Feature Plots - Condition Independent Training Method

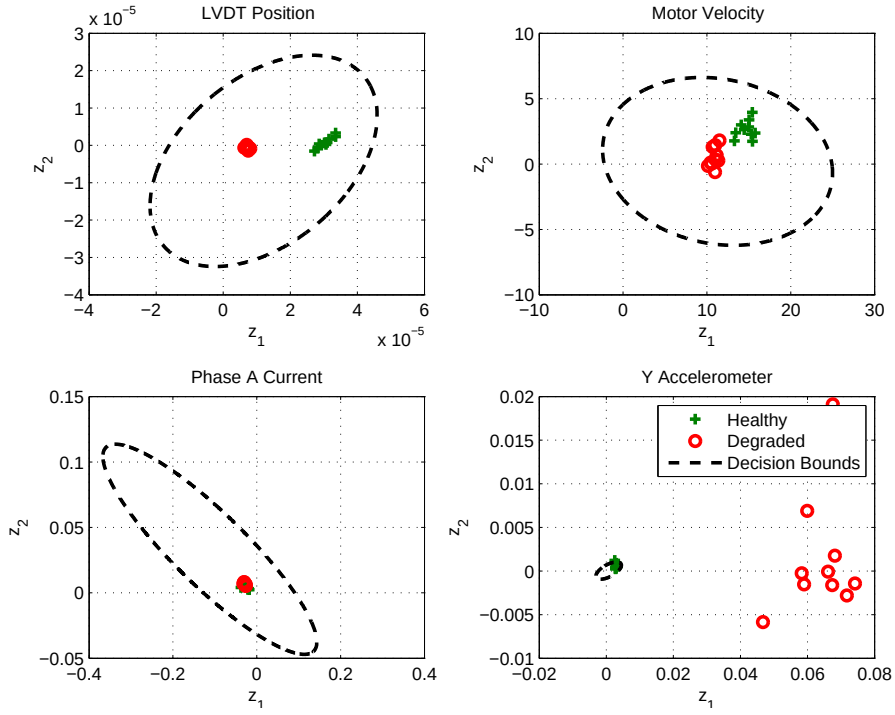

Figure 4.16: Condition 1 Test Set Data Feature Plots - Condition Independent Training Method

4.3.2 Condition 2

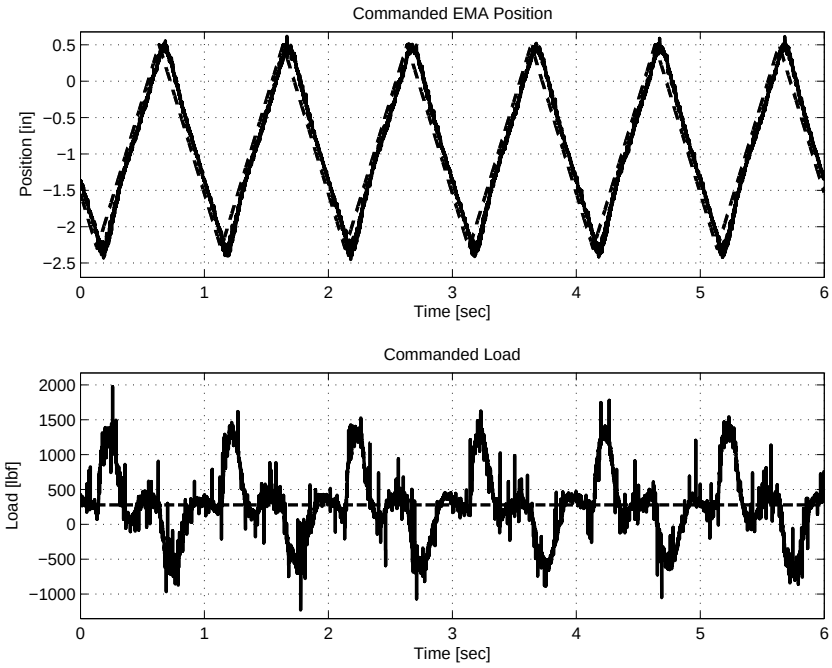

Figure 4.17: Condition 2 Healthy Command Signals.

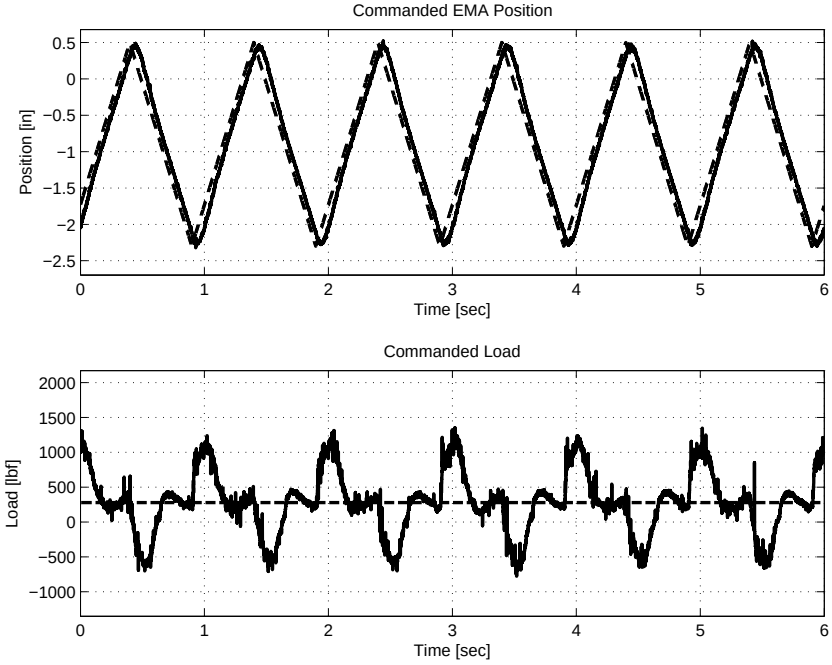

Figure 4.18: Condition 2 Degraded Command Signals.

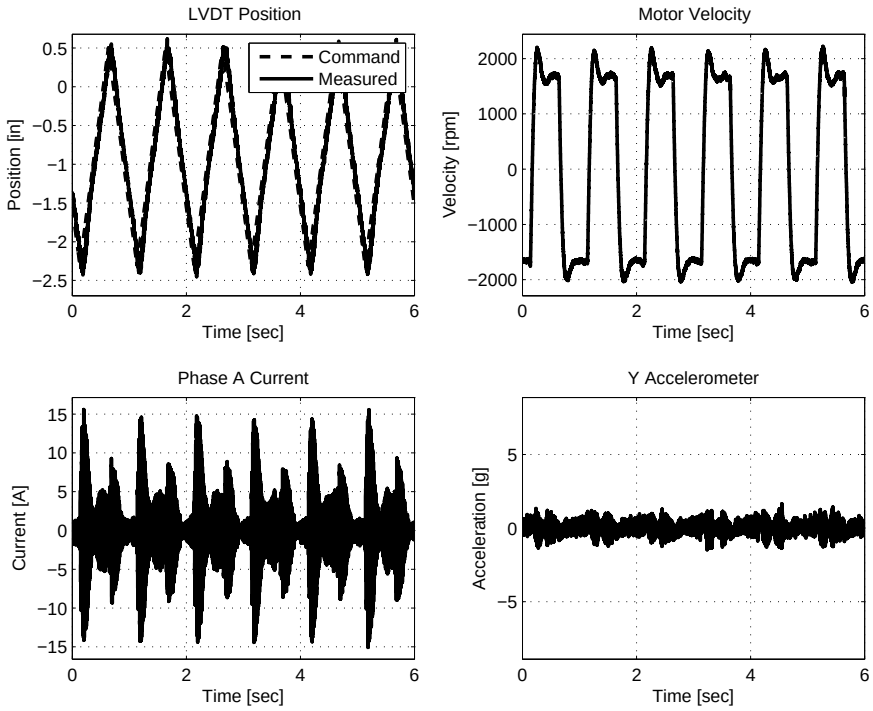

Figure 4.19: Condition 2 Healthy EMA Data.

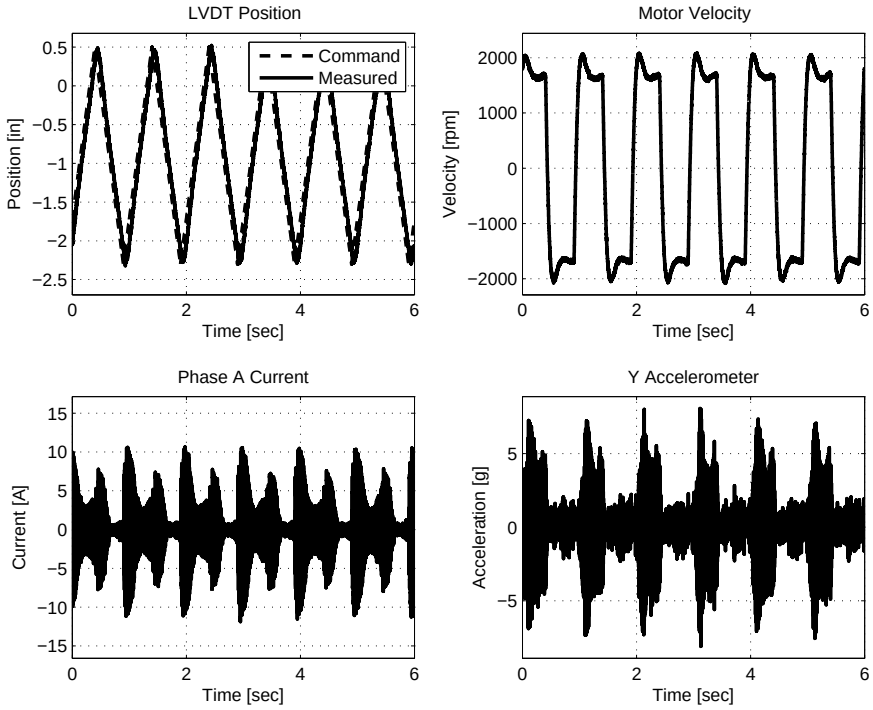

Figure 4.20: Condition 2 Degraded EMA Data.

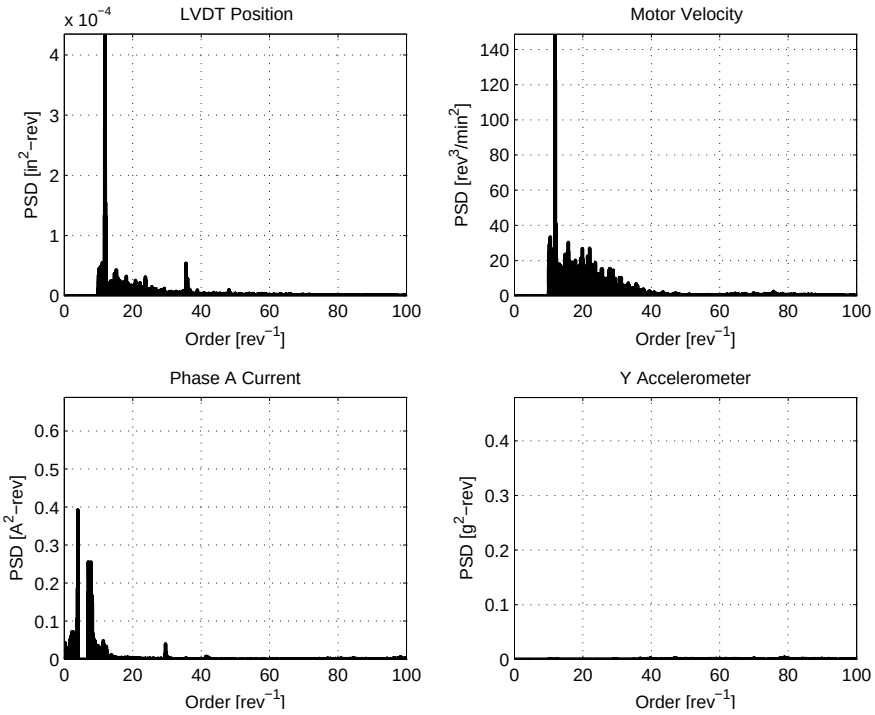

Figure 4.21: Condition 2 Healthy EMA Resampled PSD Data.

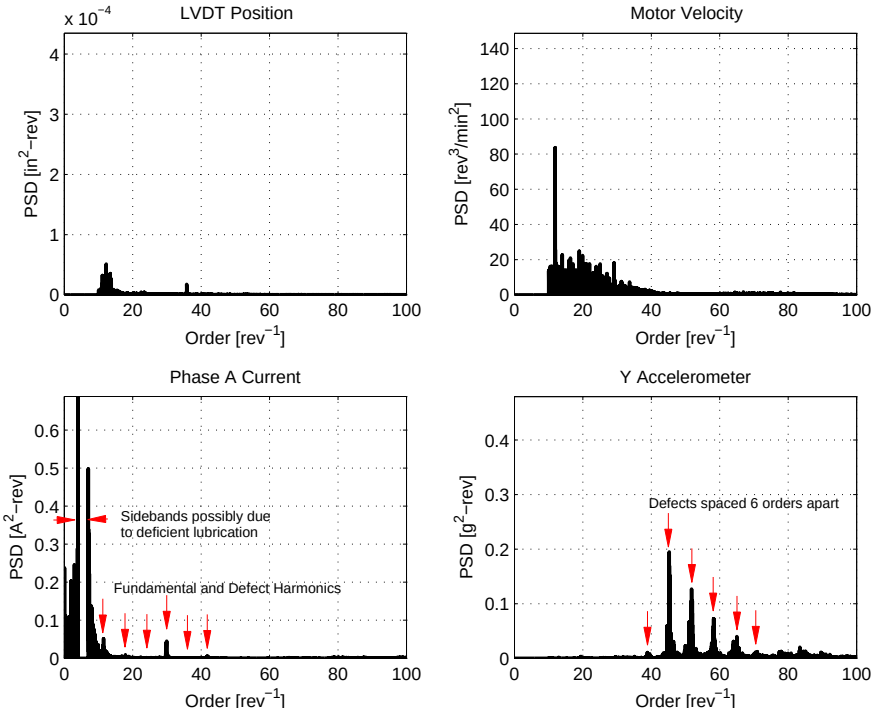

Figure 4.22: Condition 2 Degraded EMA Resampled PSD Data.

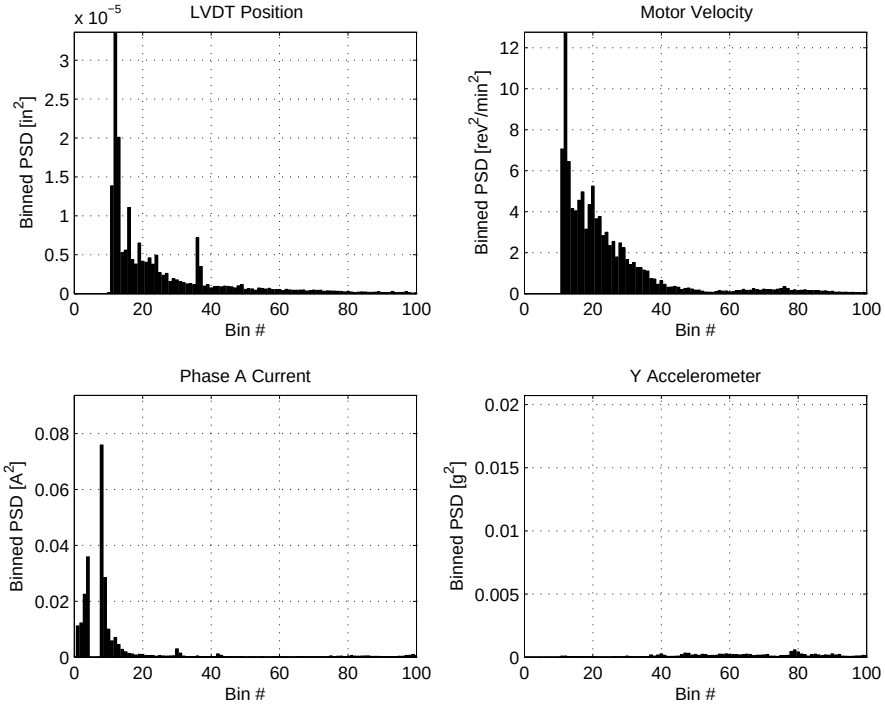

Figure 4.23: Condition 2 Healthy EMA Binned PSD Data.

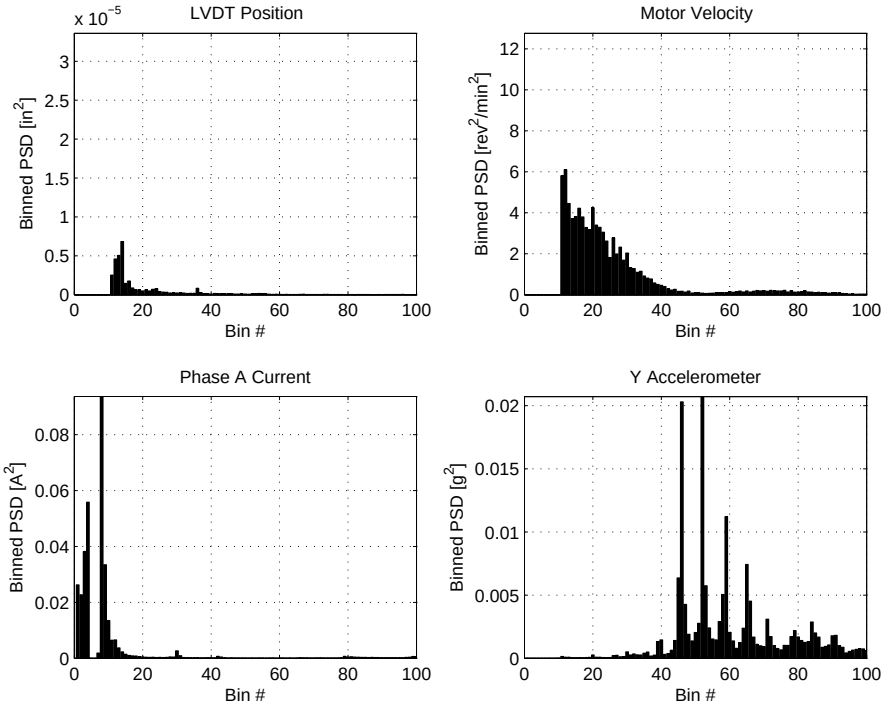

Figure 4.24: Condition 2 Degraded EMA Binned PSD Data.

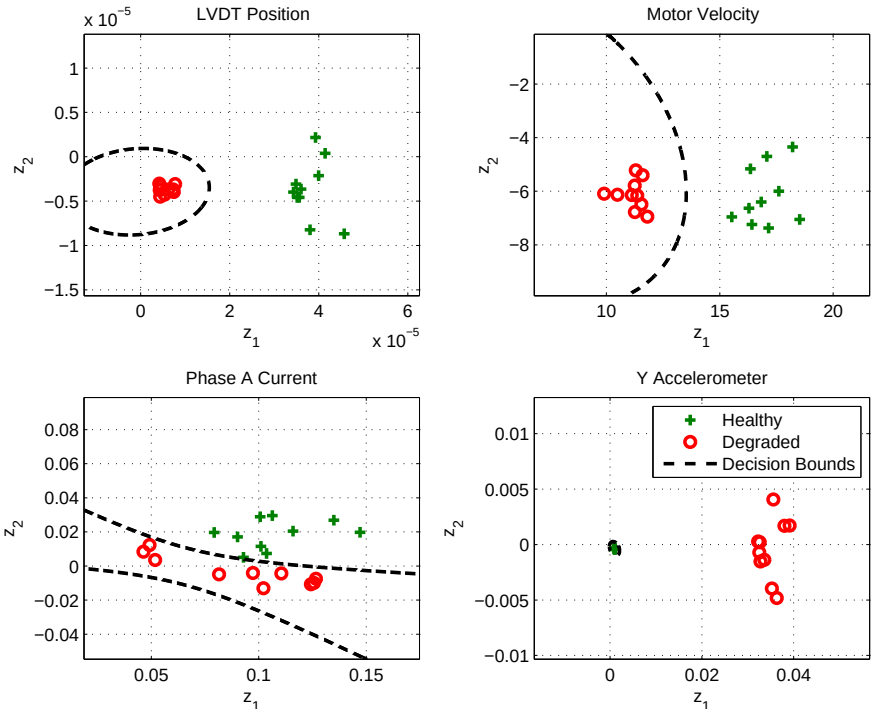

Figure 4.25: Condition 2 Training Set Data Feature Plots - Condition Dependent Training Method

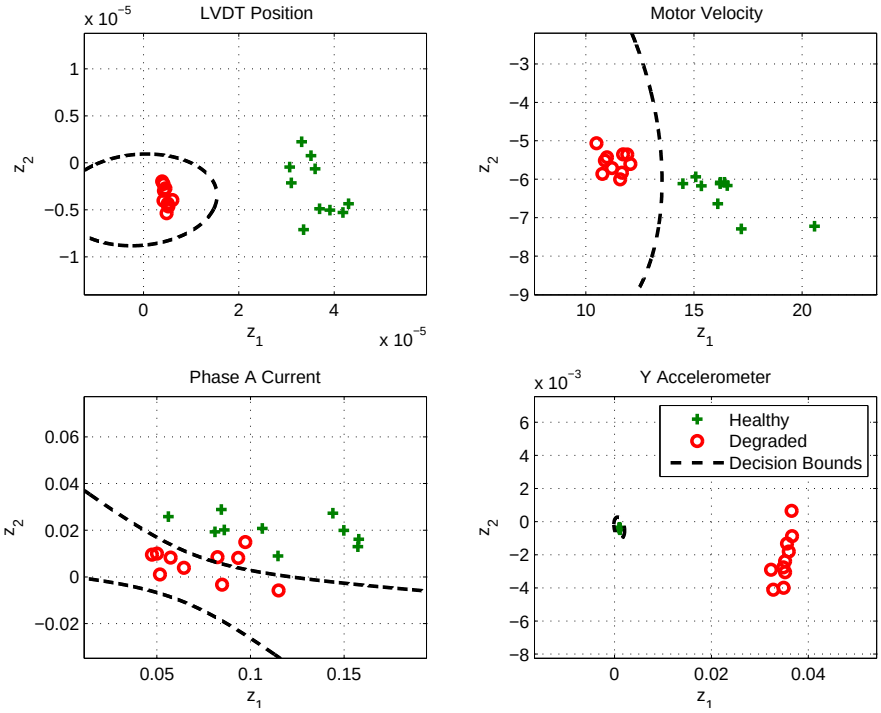

Figure 4.26: Condition 2 Test Set Data Feature Plots - Condition Dependent Training Method

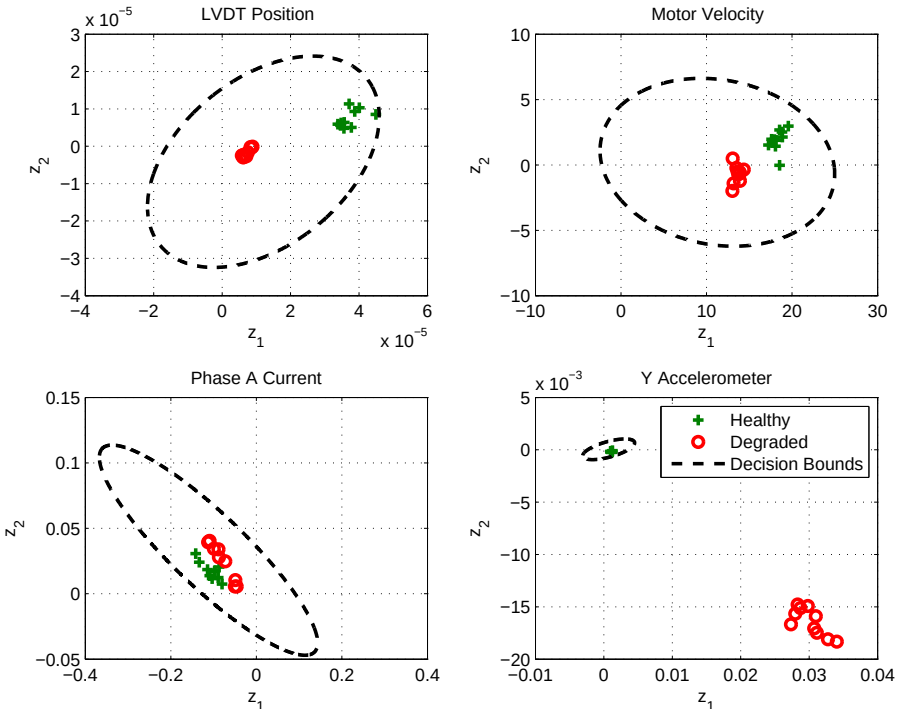

Figure 4.27: Condition 2 Training Set Data Feature Plots - Condition Independent Training Method

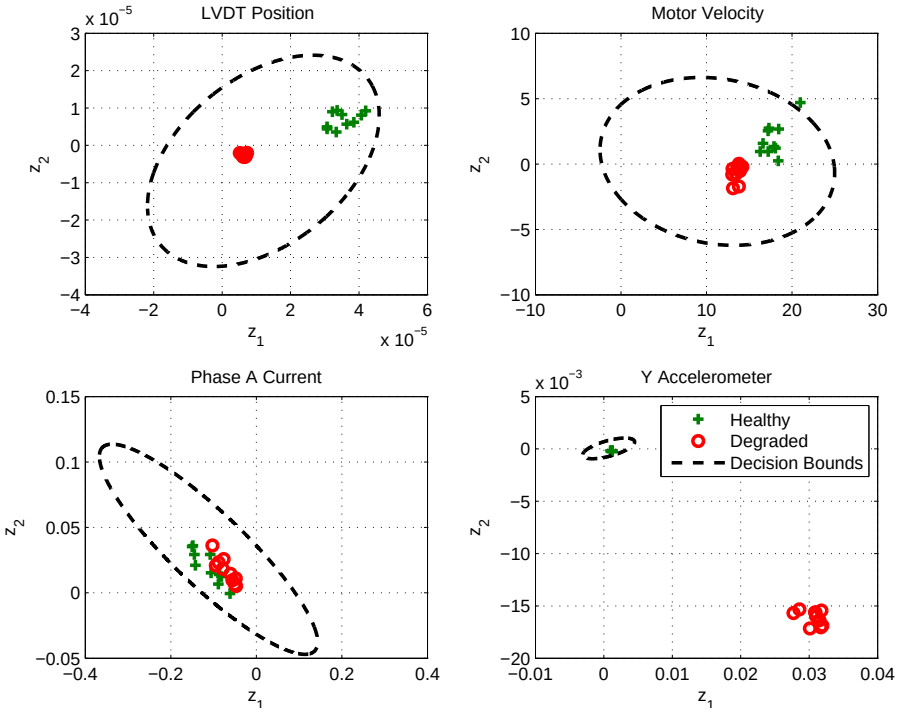

Figure 4.28: Condition 2 Test Set Data Feature Plots - Condition Independent Training Method

4.3.3 Condition 3

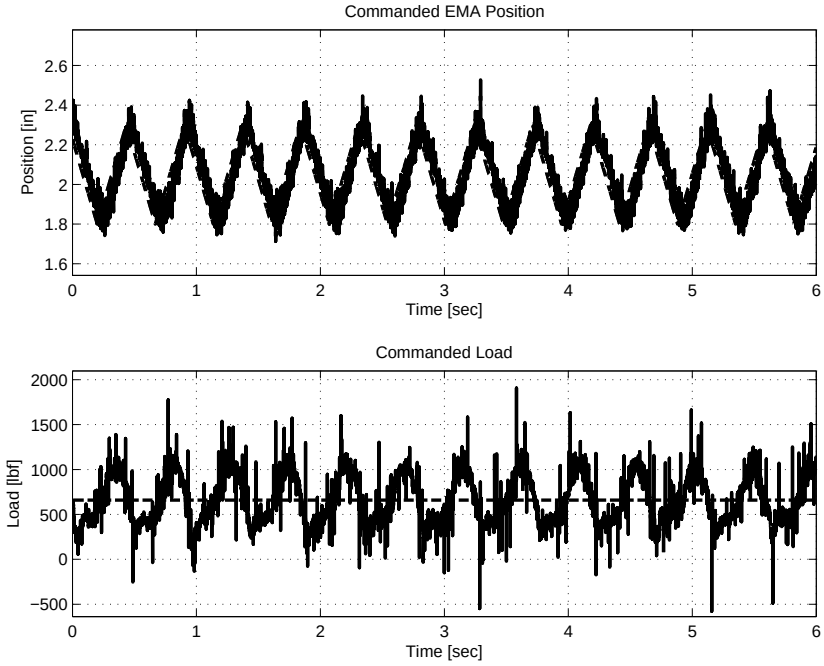

Figure 4.29: Condition 3 Healthy Command Signals.

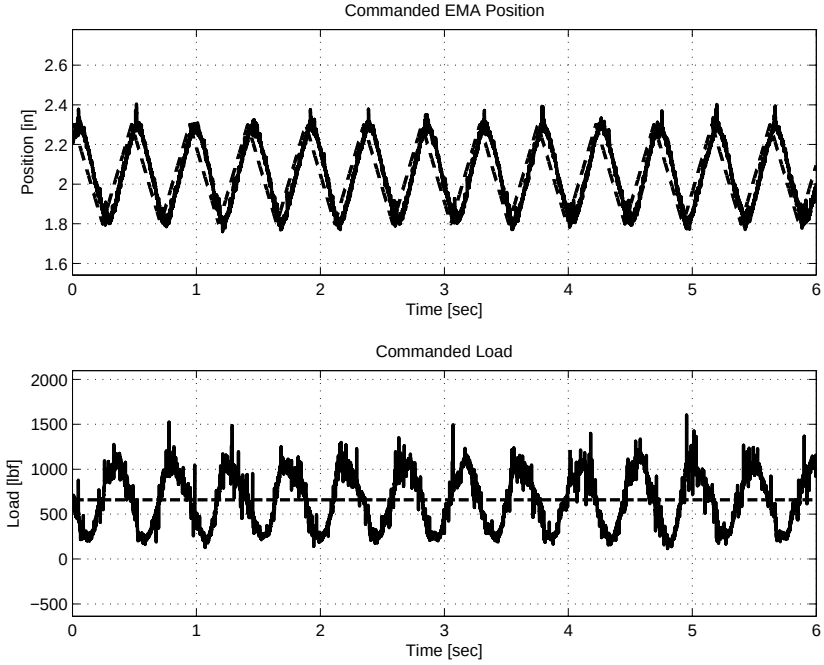

Figure 4.30: Condition 3 Degraded Command Signals.

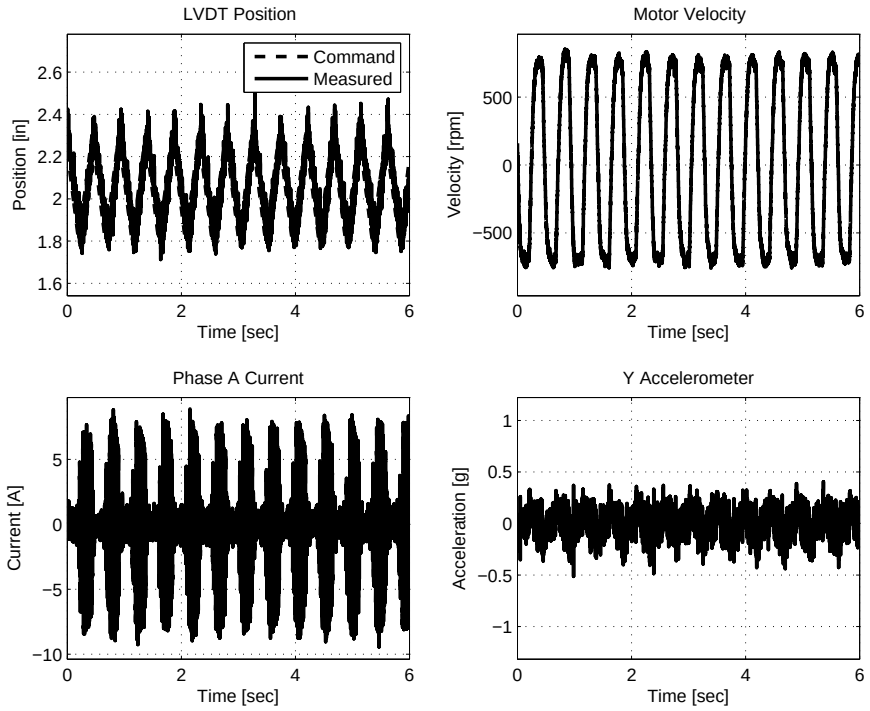

Figure 4.31: Condition 3 Healthy EMA Data.

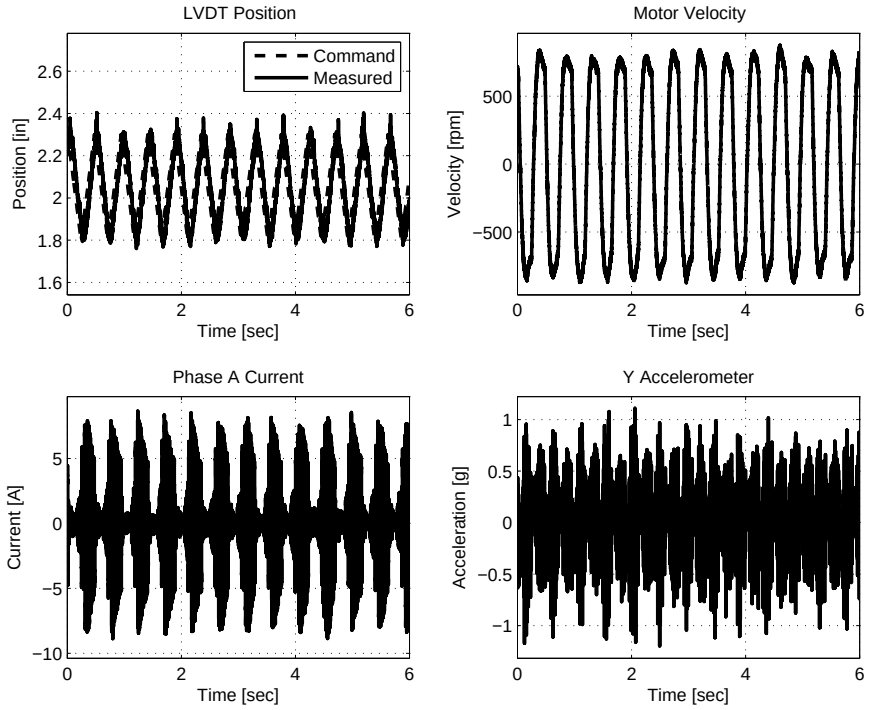

Figure 4.32: Condition 3 Degraded EMA Data.

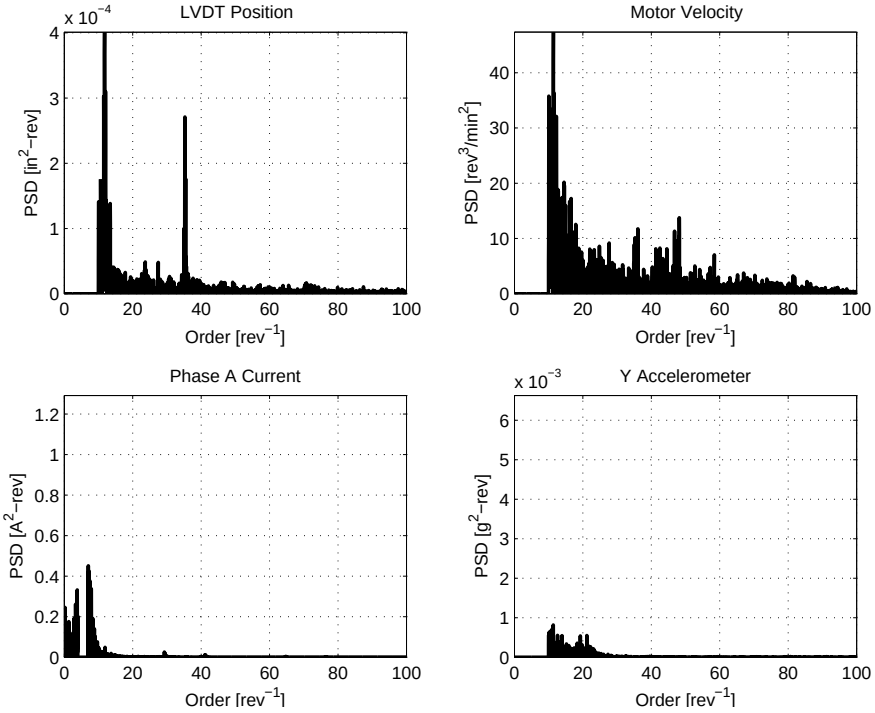

Figure 4.33: Condition 3 Healthy EMA Resampled PSD Data.

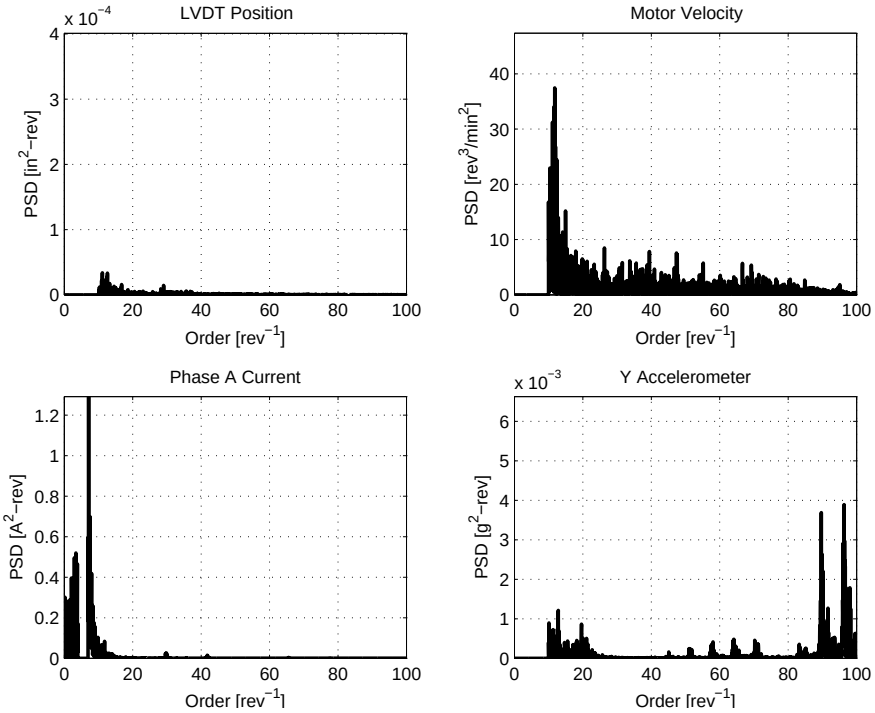

Figure 4.34: Condition 3 Degraded EMA Resampled PSD Data.

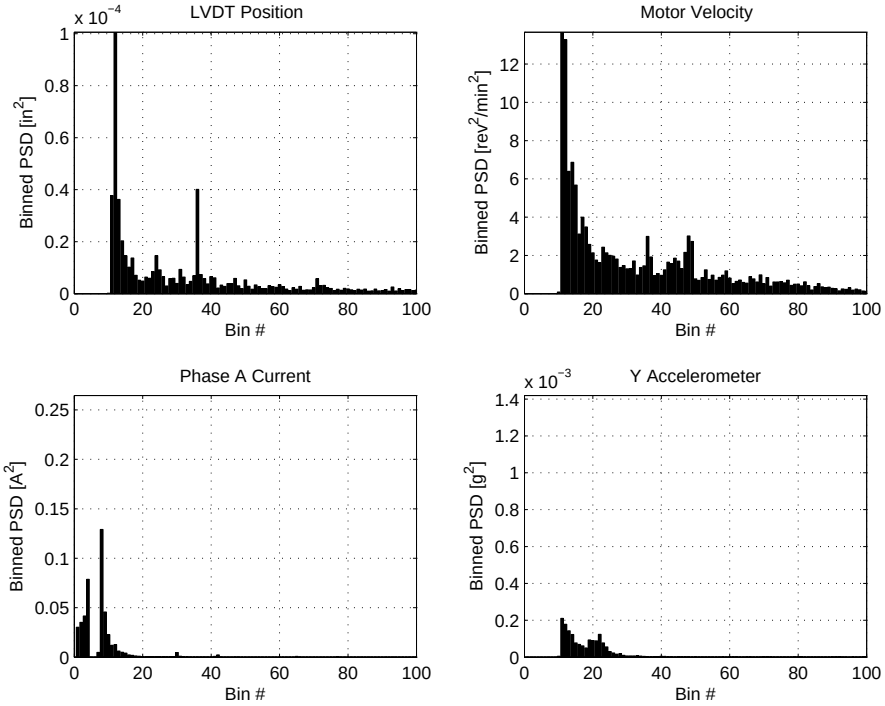

Figure 4.35: Condition 3 Healthy EMA Binned PSD Data.

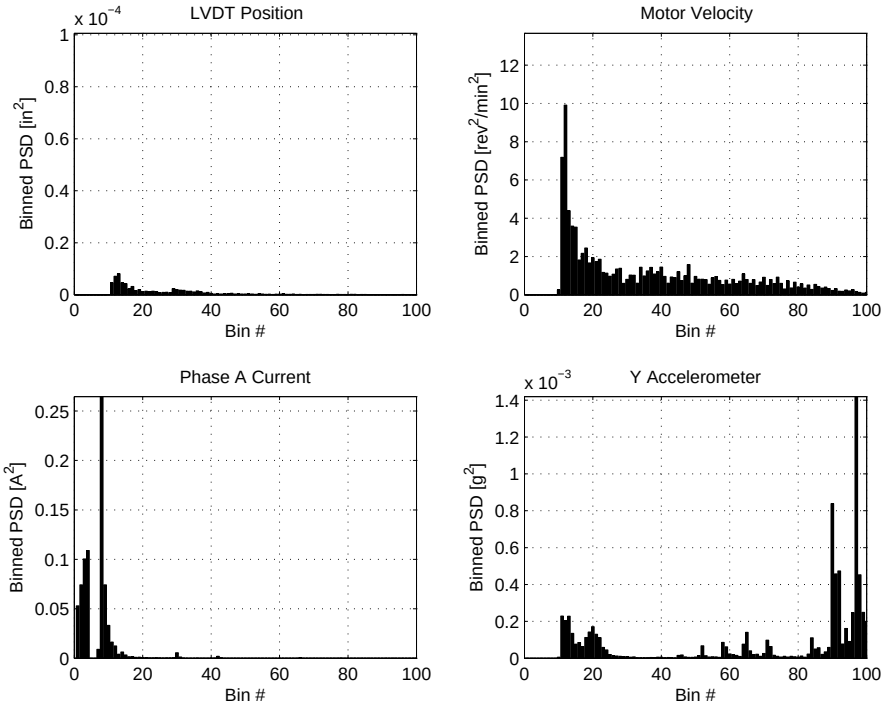

Figure 4.36: Condition 3 Degraded EMA Binned PSD Data.

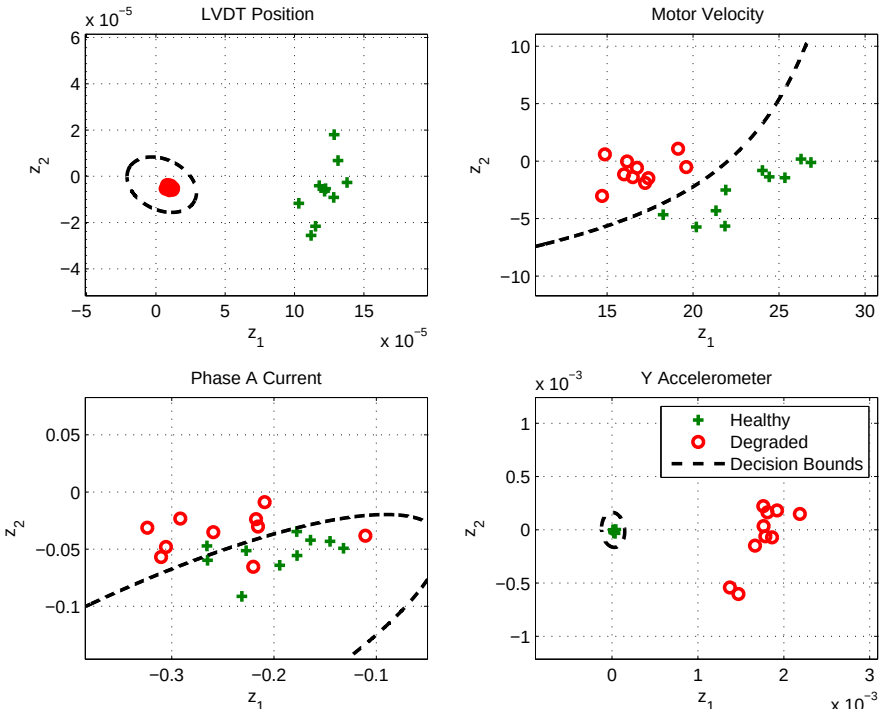

Figure 4.37: Condition 3 Training Set Data Feature Plots - Condition Dependent Training Method

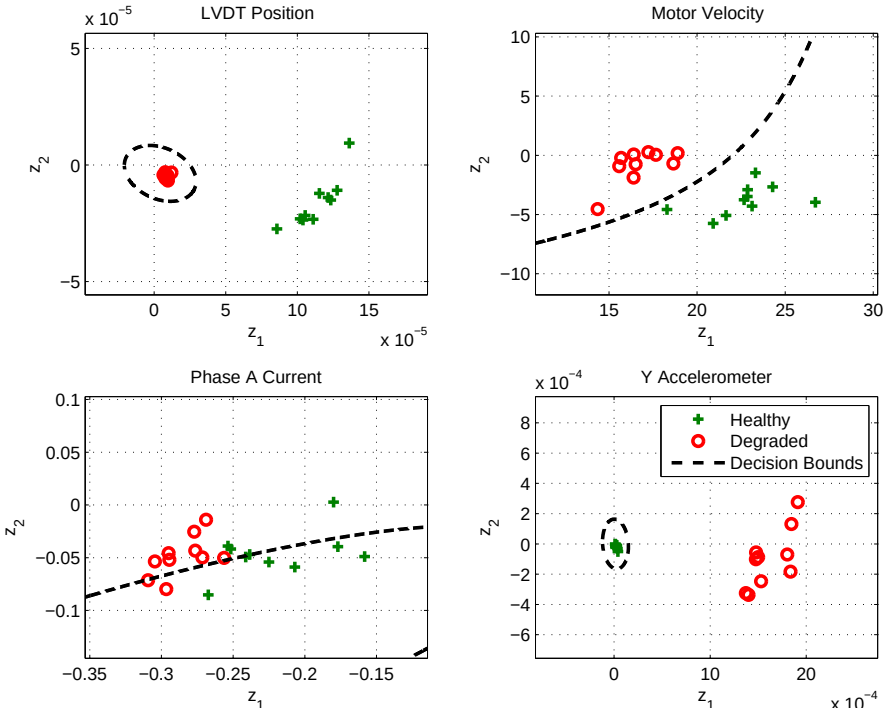

Figure 4.38: Condition 3 Test Set Data Feature Plots - Condition Dependent Training Method

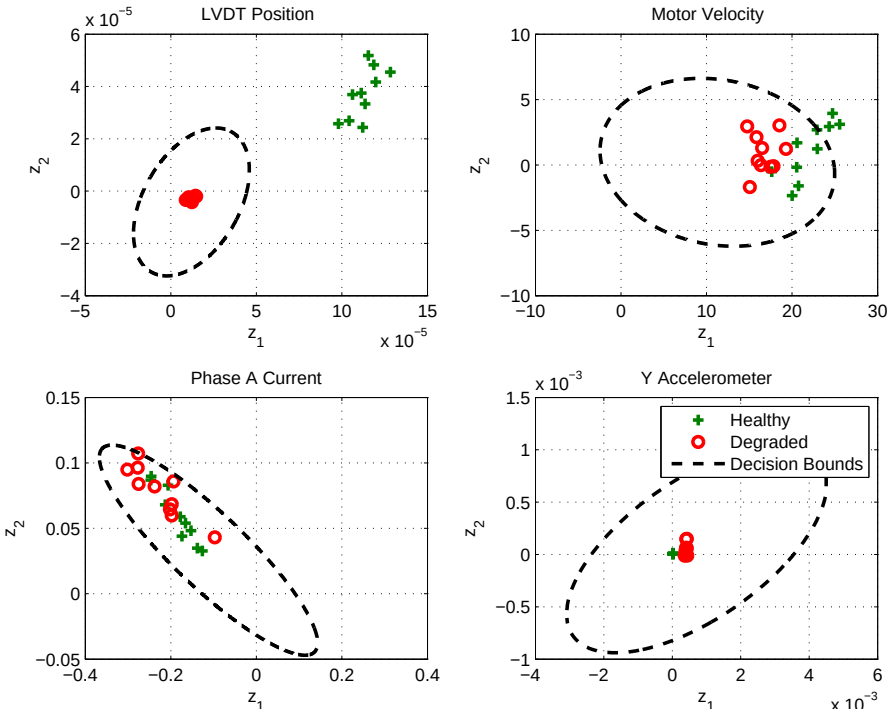

Figure 4.39: Condition 3 Training Set Data Feature Plots - Condition Independent Training Method

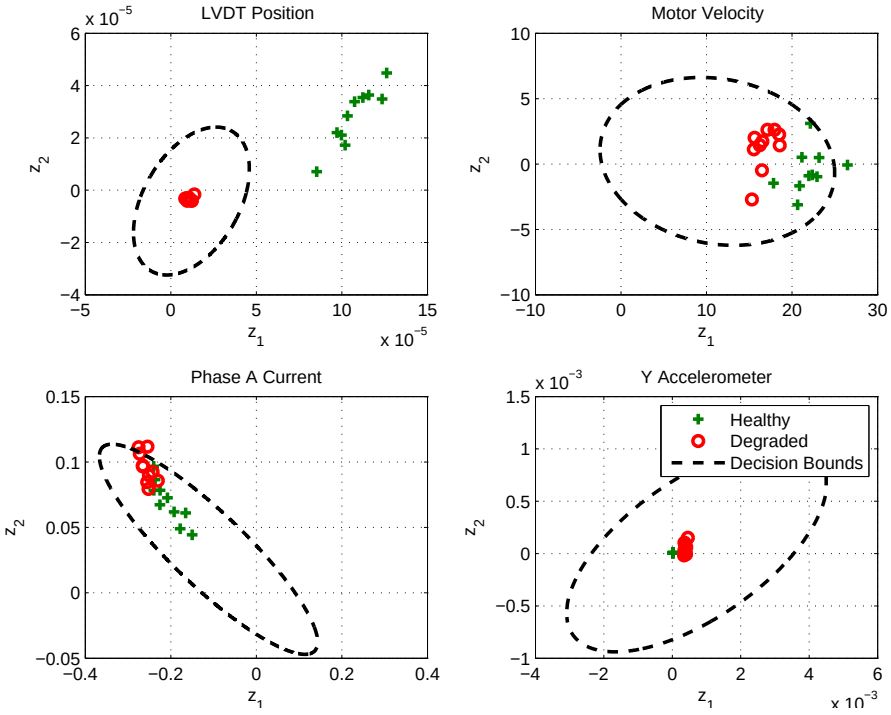

Figure 4.40: Condition 3 Test Set Data Feature Plots - Condition Independent Training Method

4.3.4 Condition 4

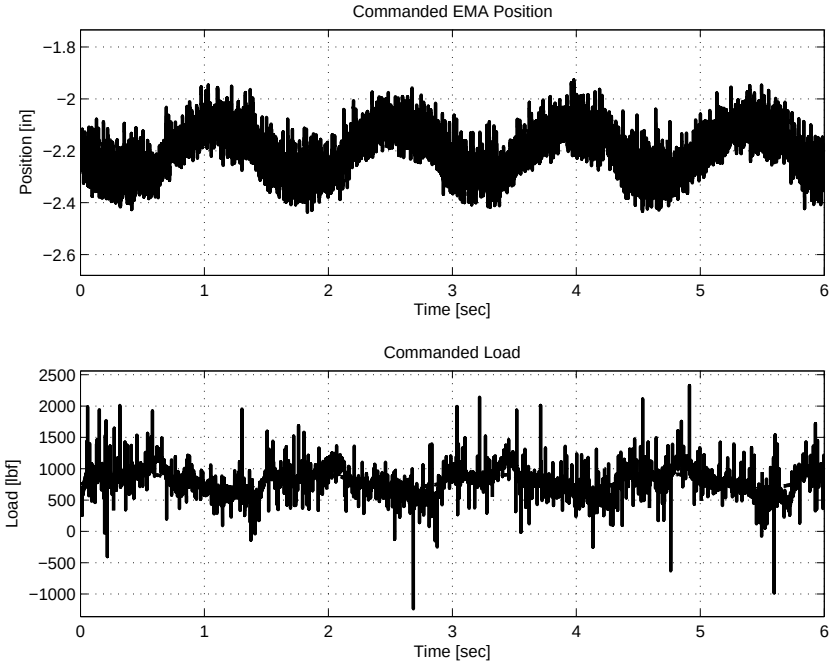

Figure 4.41: Condition 4 Healthy Command Signals.

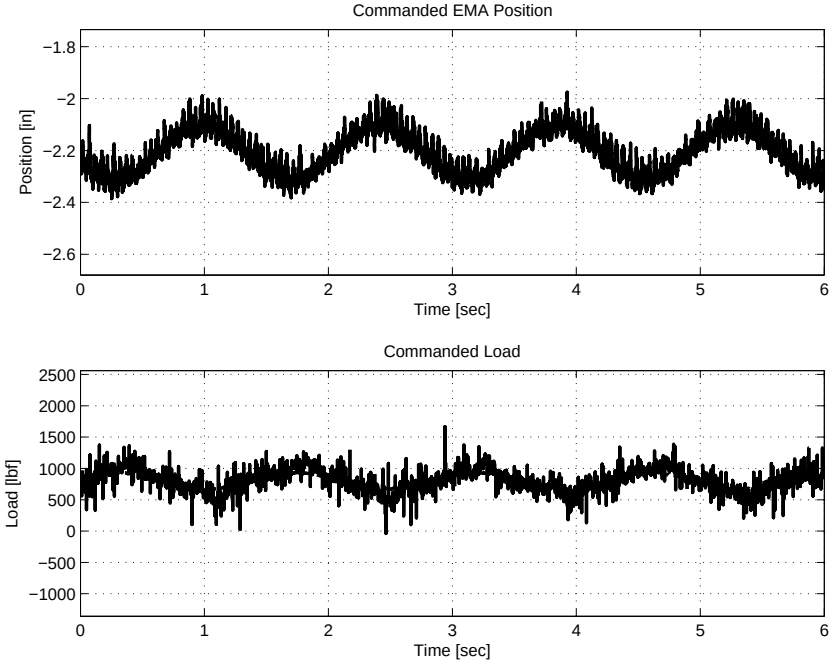

Figure 4.42: Condition 4 Degraded Command Signals.

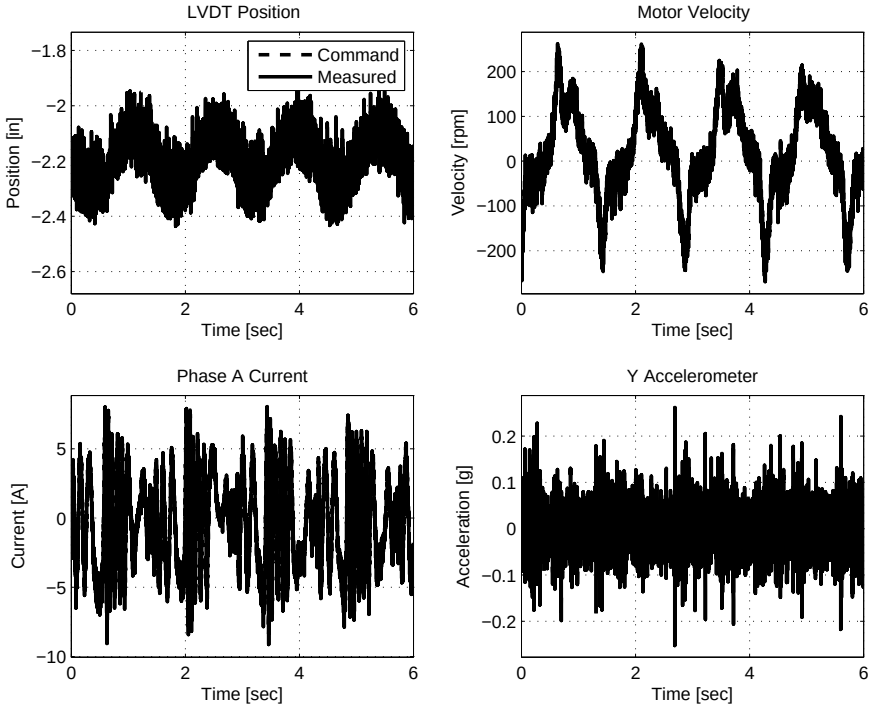

Figure 4.43: Condition 4 Healthy EMA Data.

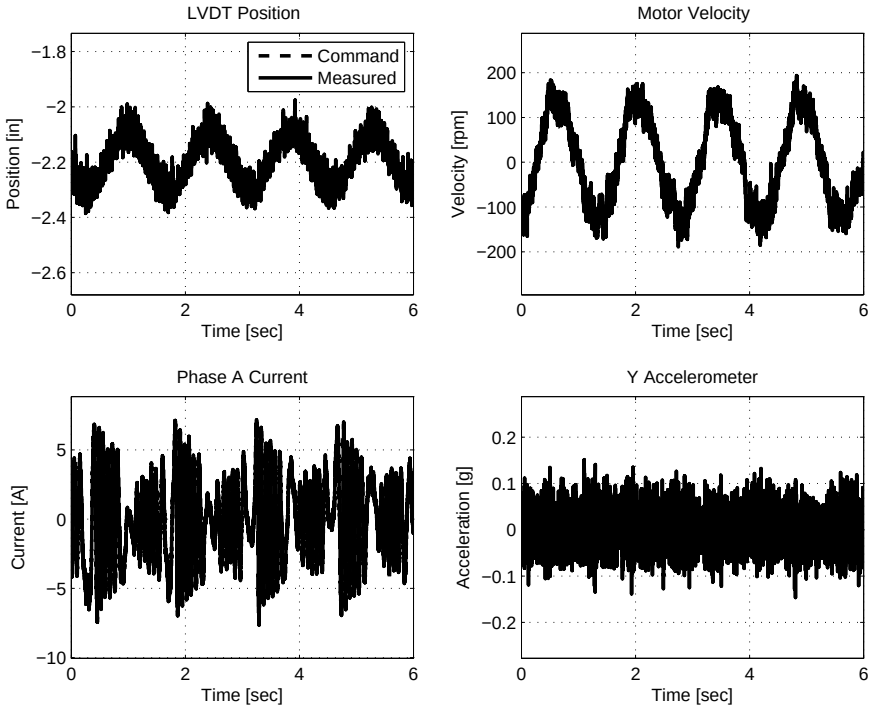

Figure 4.44: Condition 4 Degraded EMA Data.

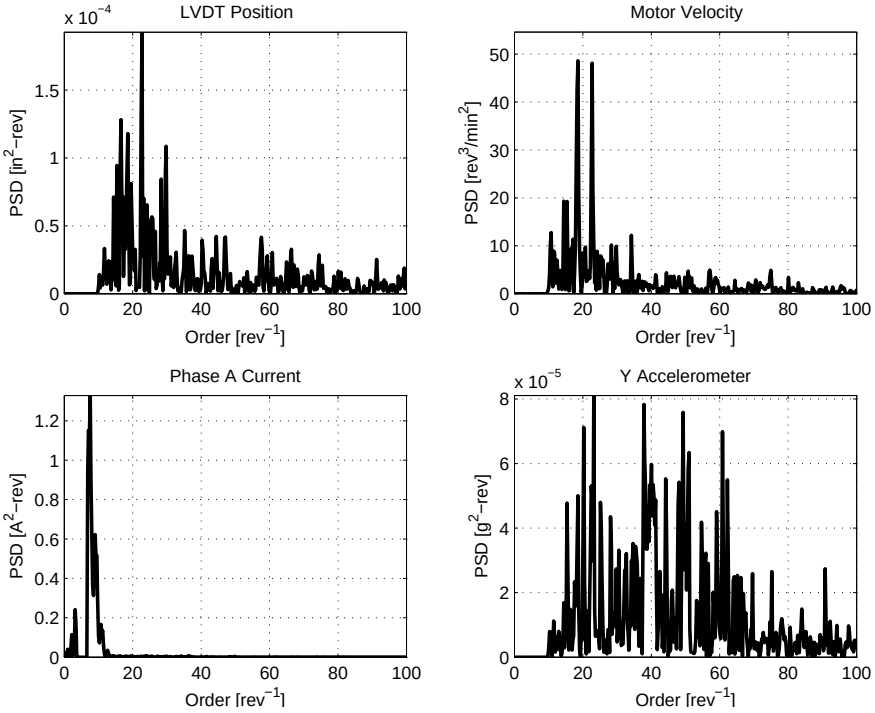

Figure 4.45: Condition 4 Healthy EMA Resampled PSD Data.

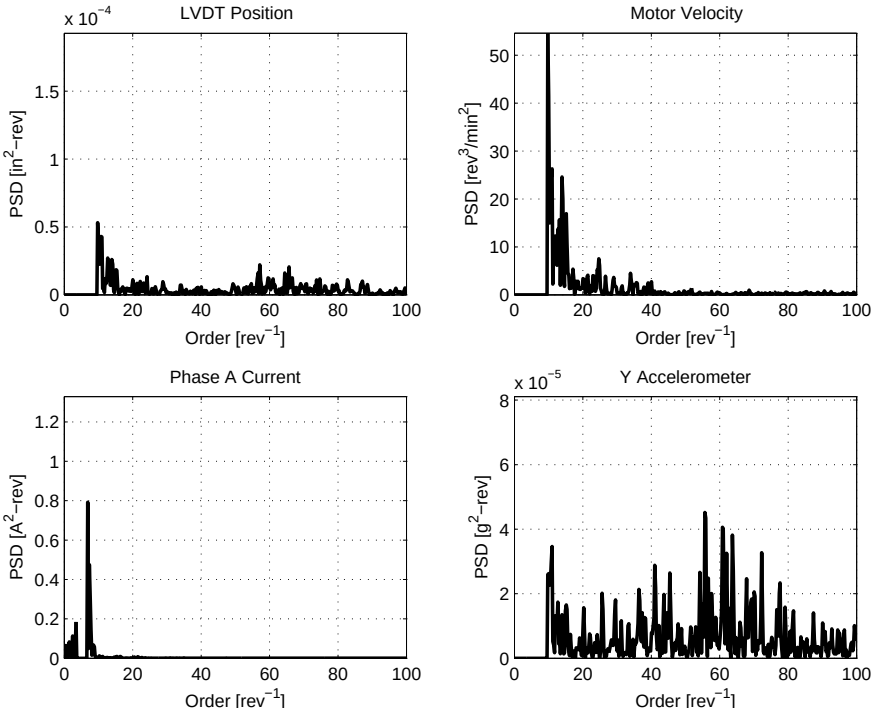

Figure 4.46: Condition 4 Degraded EMA Resampled PSD Data.

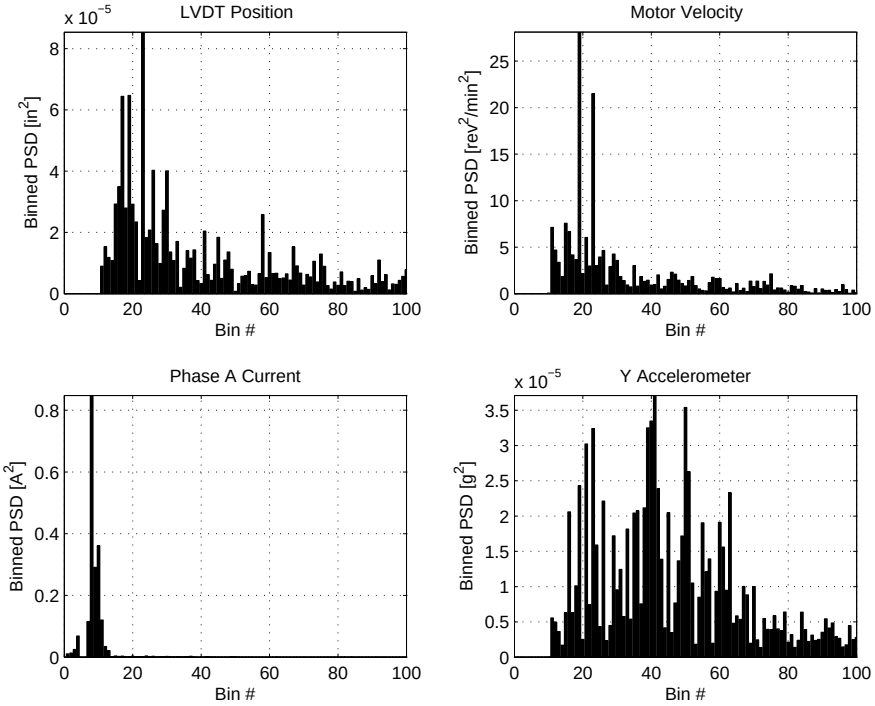

Figure 4.47: Condition 4 Healthy EMA Binned PSD Data.

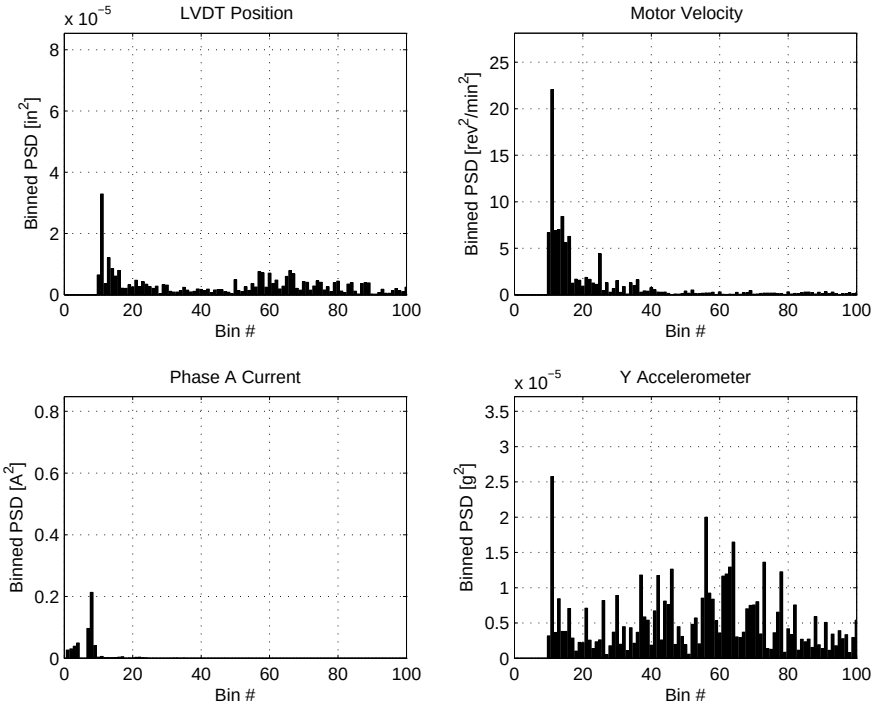

Figure 4.48: Condition 4 Degraded EMA Binned PSD Data.

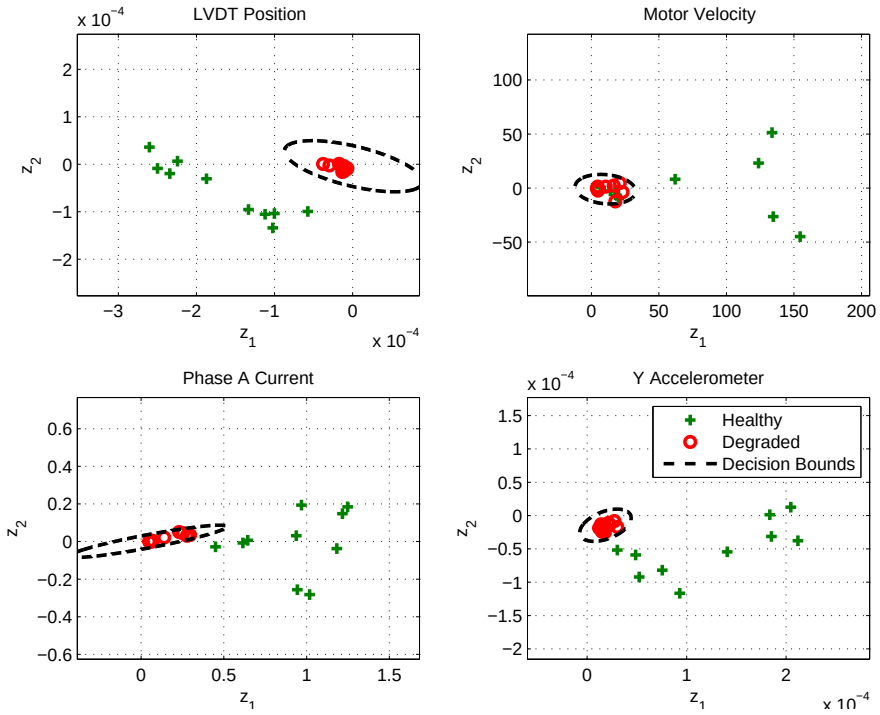

Figure 4.49: Condition 4 Training Set Data Feature Plots - Condition Dependent Training Method

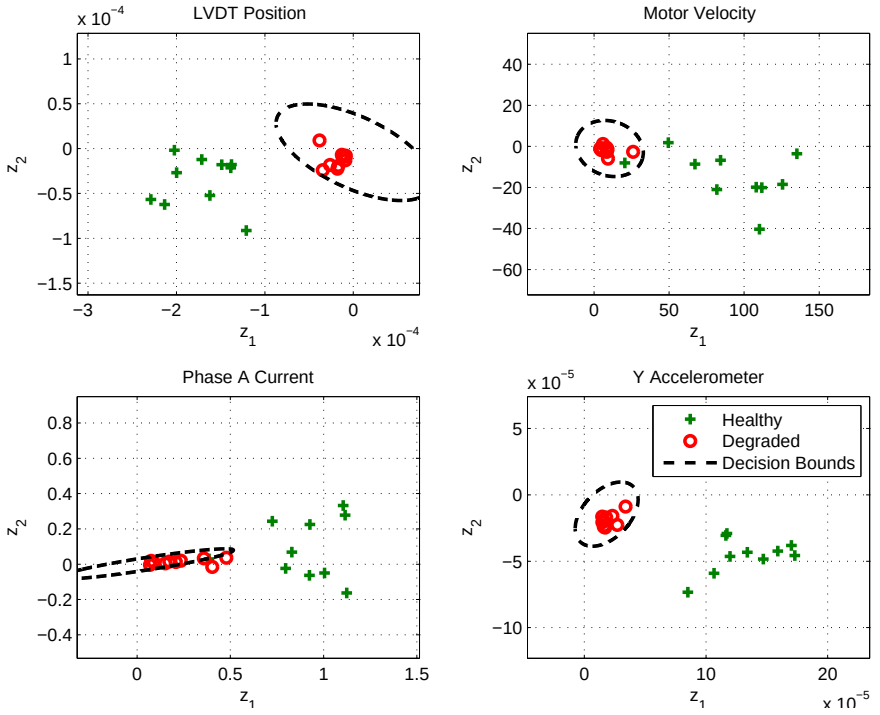

Figure 4.50: Condition 4 Test Set Data Feature Plots - Condition Dependent Training Method

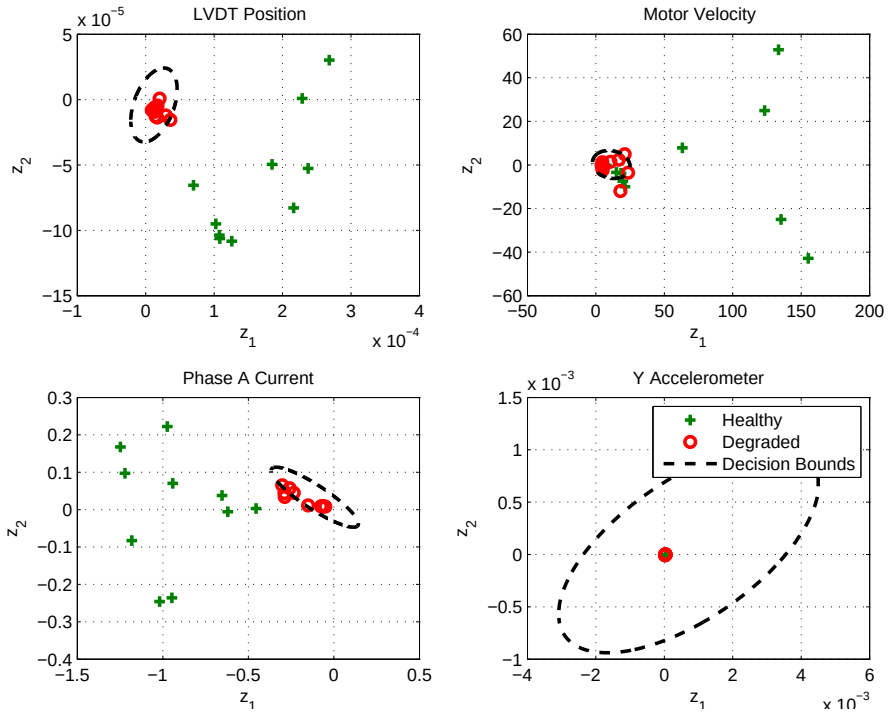

Figure 4.51: Condition 4 Training Set Data Feature Plots - Condition Independent Training Method

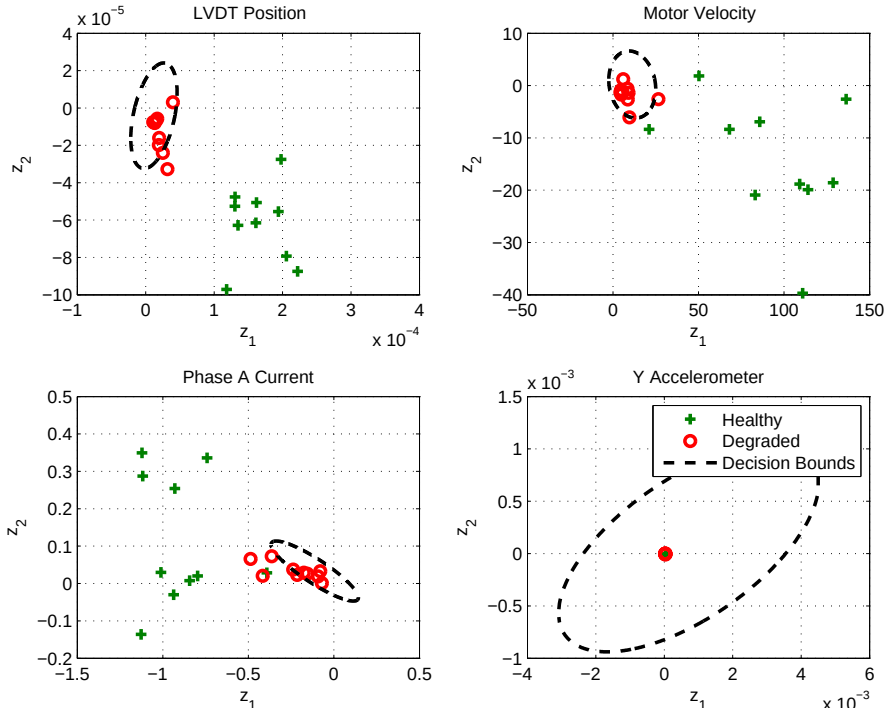

Figure 4.52: Condition 4 Test Set Data Feature Plots - Condition Independent Training Method

4.3.5 Condition 5

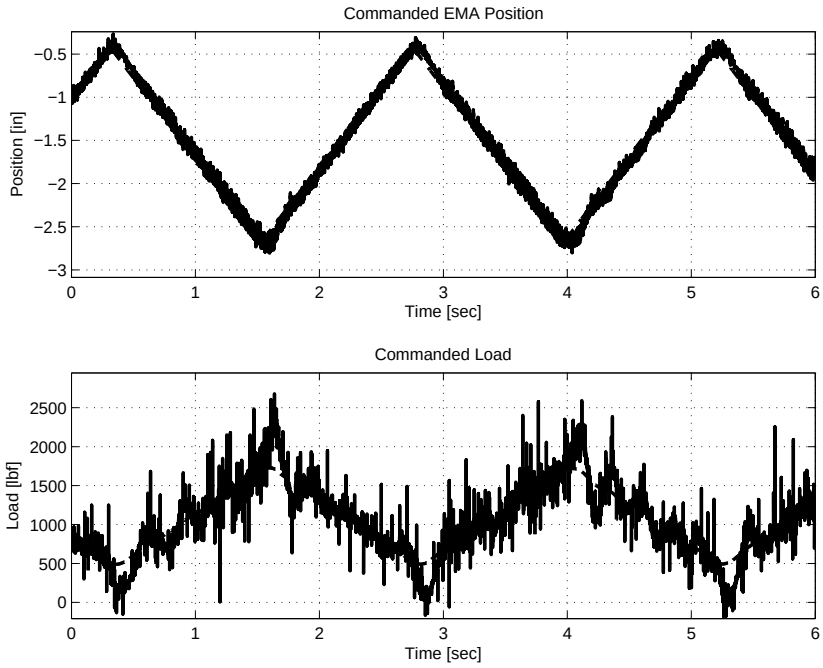

Figure 4.53: Condition 5 Healthy Command Signals.

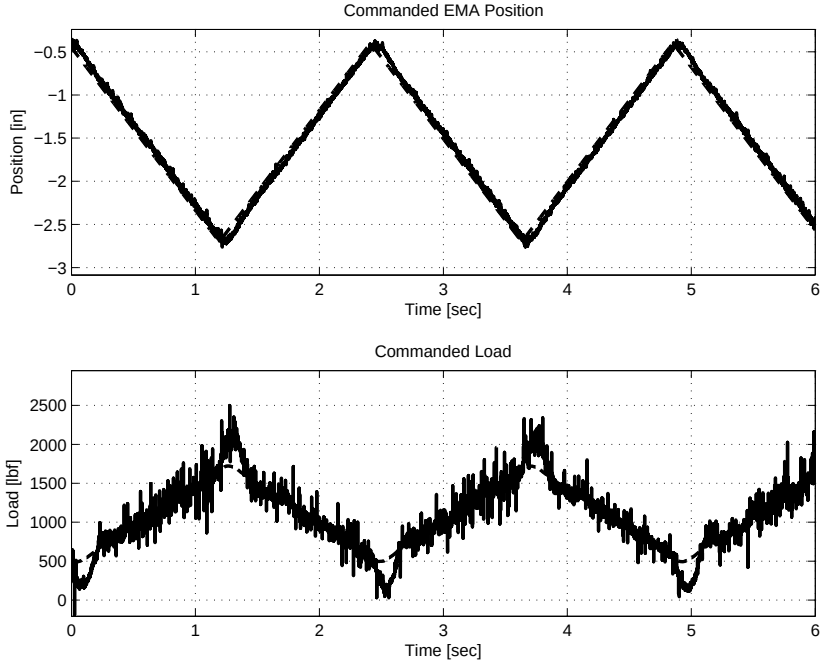

Figure 4.54: Condition 5 Degraded Command Signals.

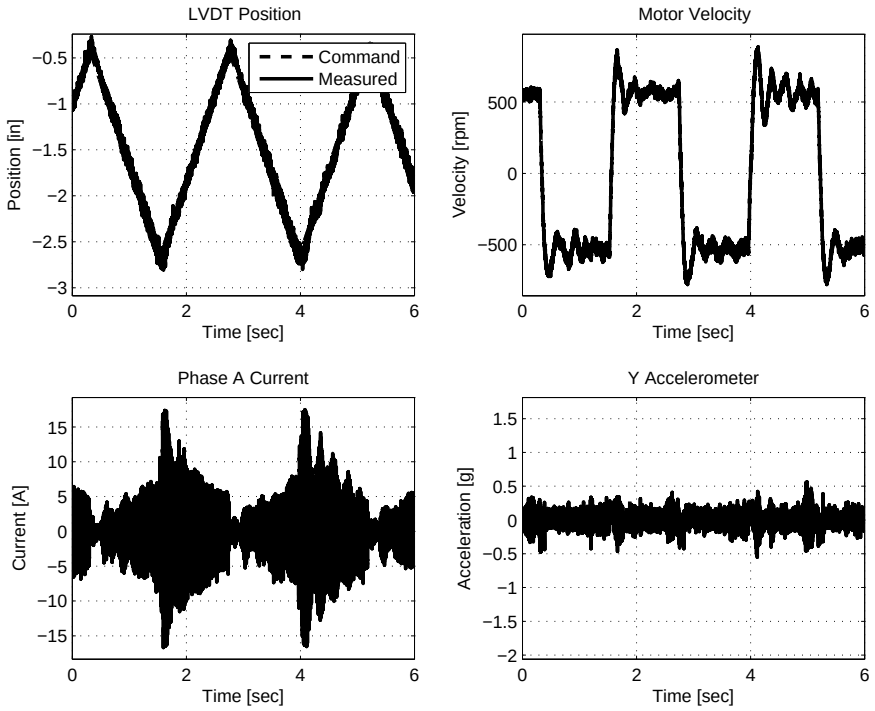

Figure 4.55: Condition 5 Healthy EMA Data.

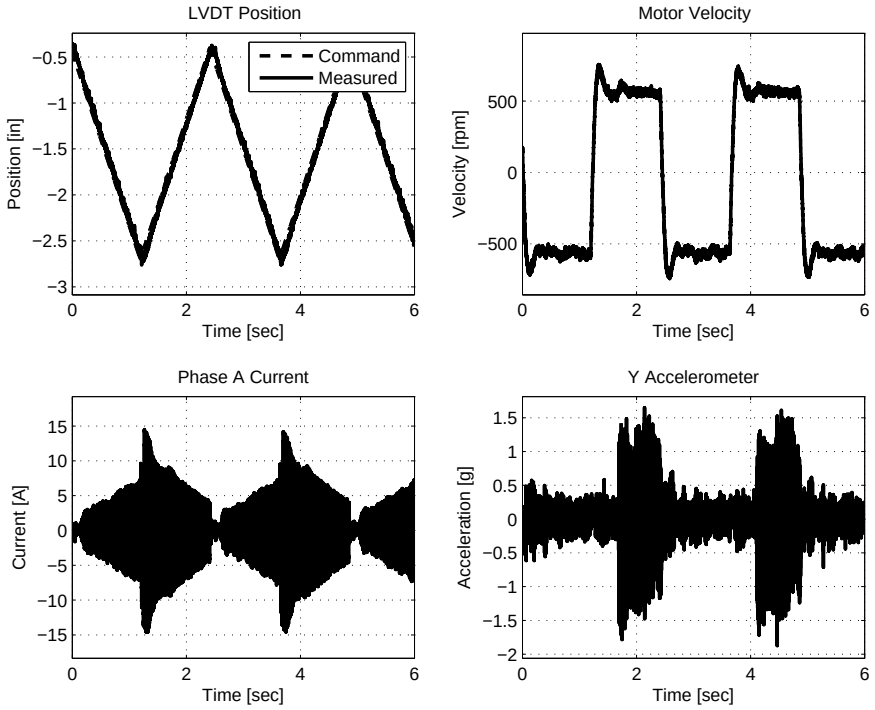

Figure 4.56: Condition 5 Degraded EMA Data.

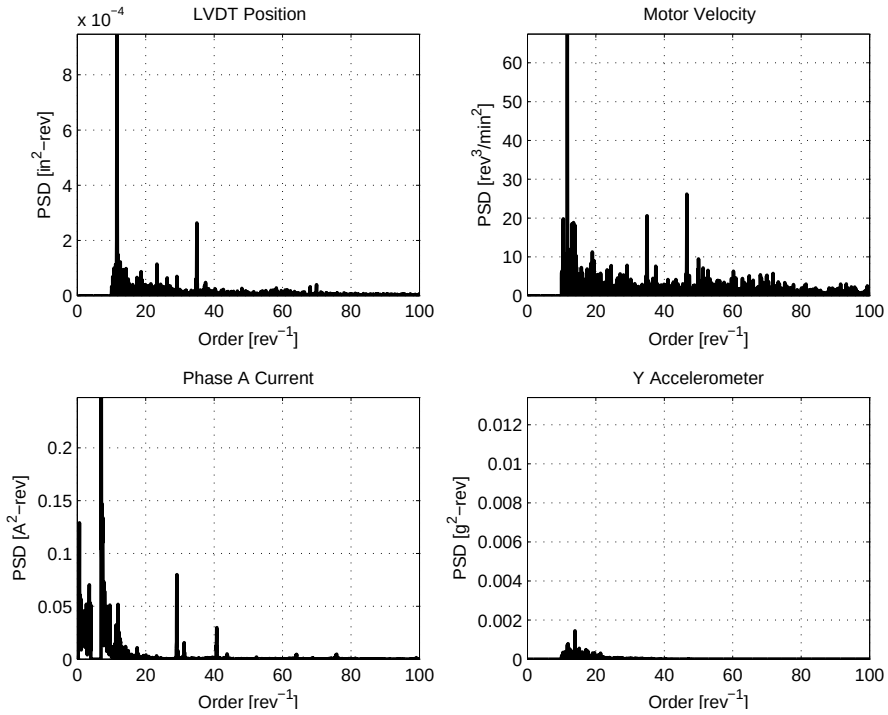

Figure 4.57: Condition 5 Healthy EMA Resampled PSD Data.

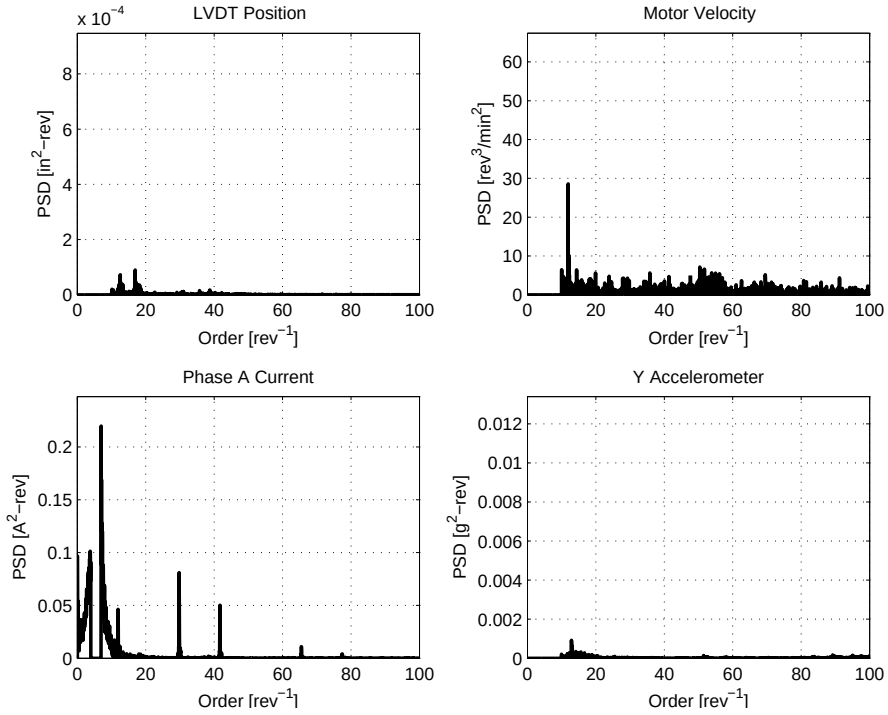

Figure 4.58: Condition 5 Degraded EMA Resampled PSD Data.

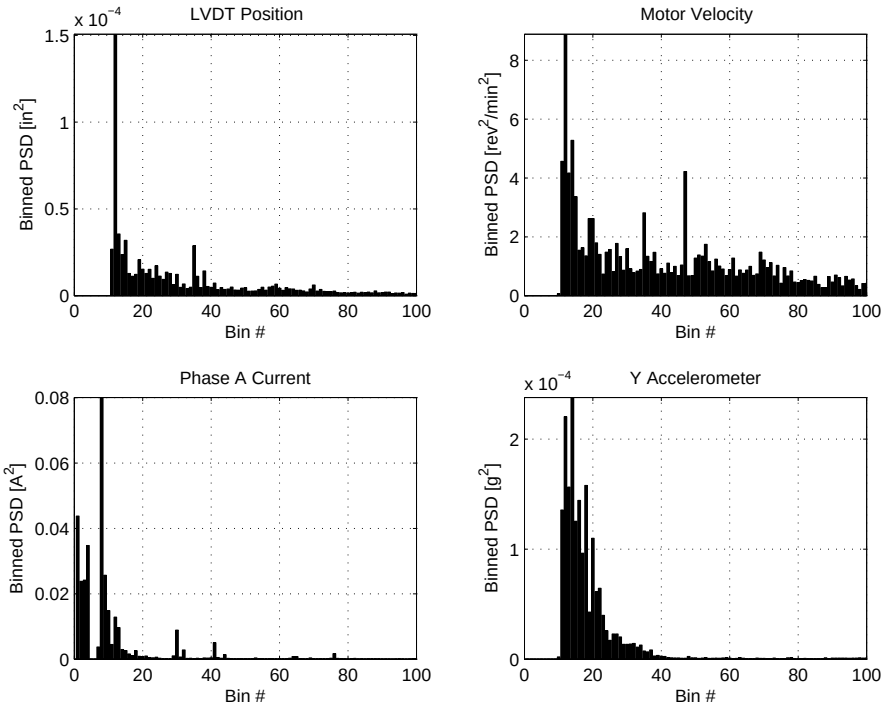

Figure 4.59: Condition 5 Healthy EMA Binned PSD Data.

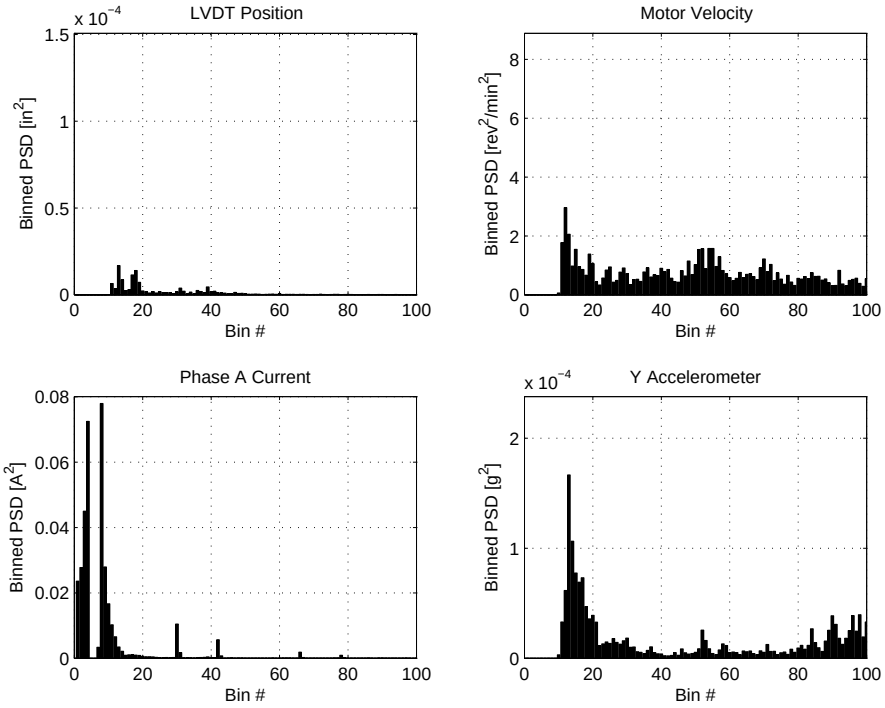

Figure 4.60: Condition 5 Degraded EMA Binned PSD Data.

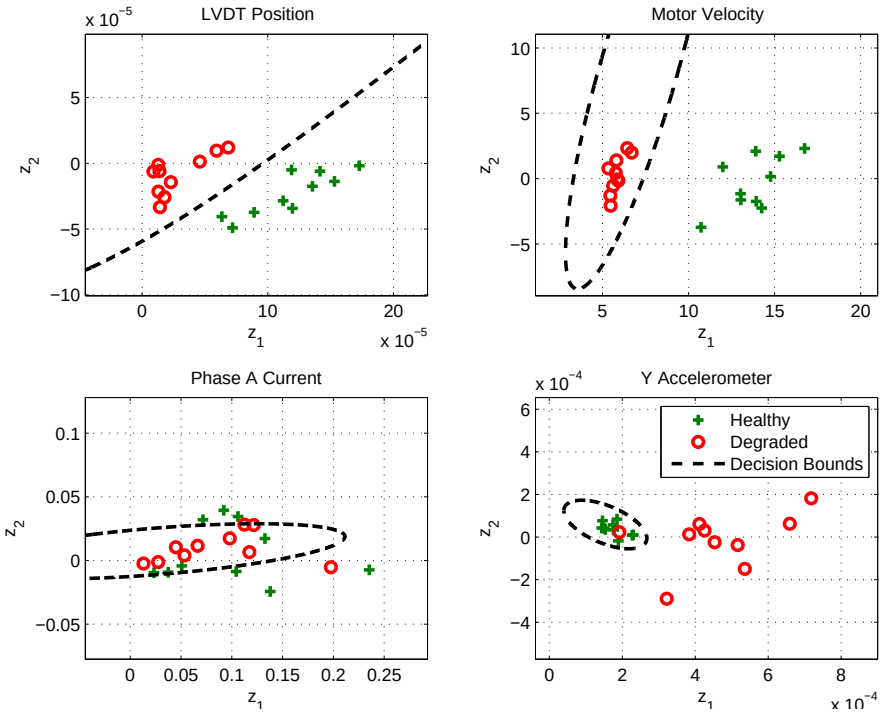

Figure 4.61: Condition 5 Training Set Data Feature Plots - Condition Dependent Training Method

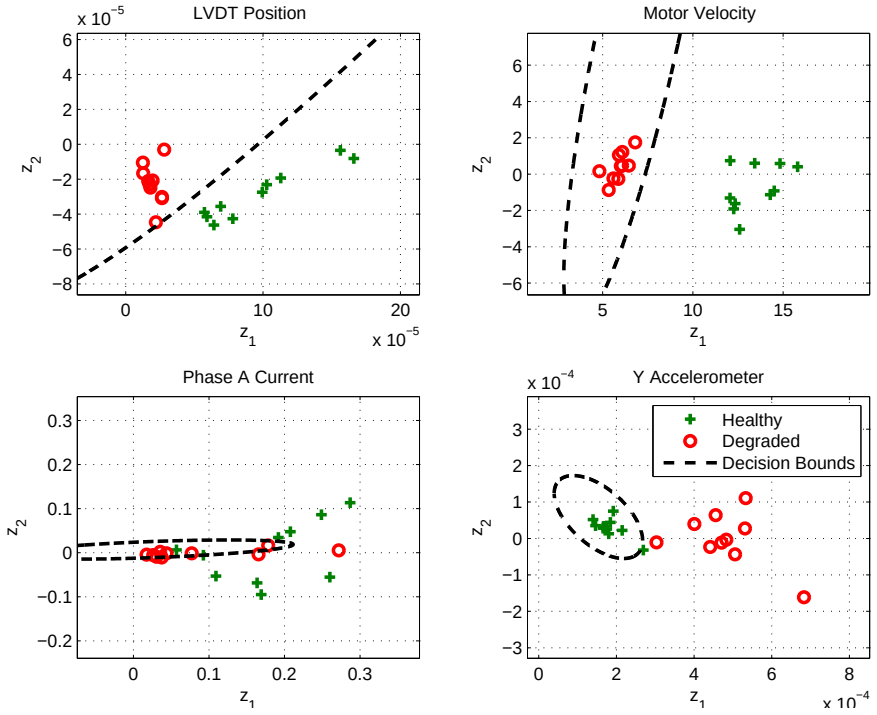

Figure 4.62: Condition 5 Test Set Data Feature Plots - Condition Dependent Training Method

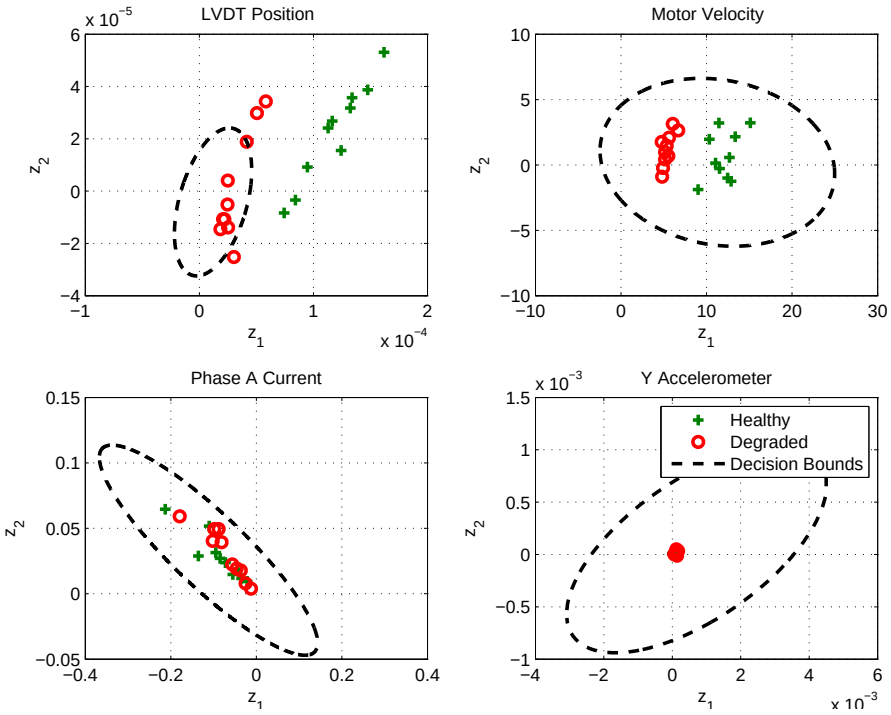

Figure 4.63: Condition 5 Training Set Data Feature Plots - Condition Independent Training Method

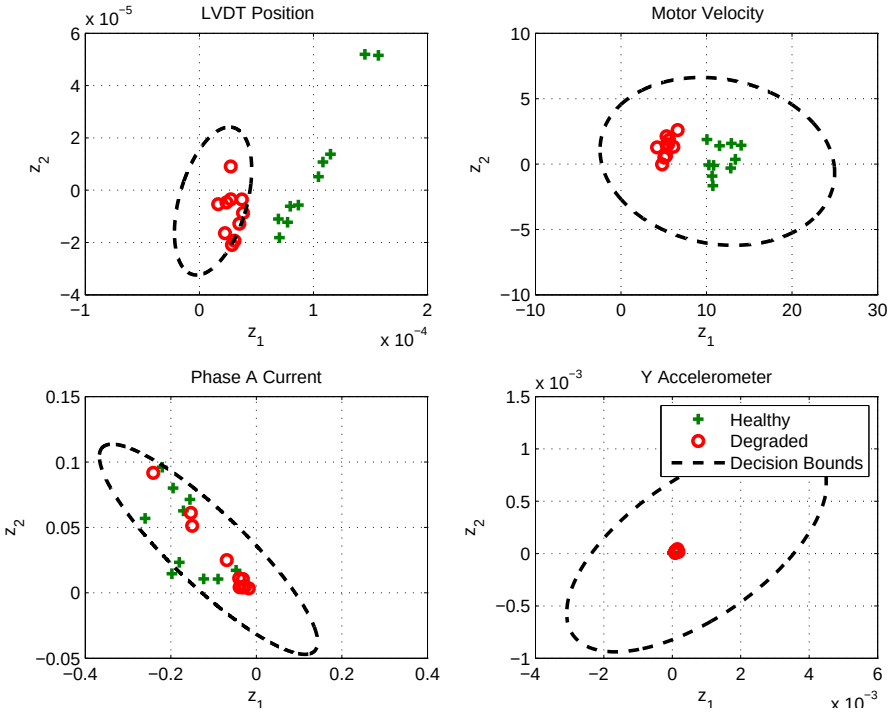

Figure 4.64: Condition 5 Test Set Data Feature Plots - Condition Independent Training Method

4.4 Results Summary

The overall performance of the feature extraction and classification technique may be summarized by the number of correct, false positive, and false negative classifications. A classification is counted as correct when data from the healthy unit is classified as ”healthy” or when the data from the degraded unit is classified as ”degraded”. A false positive is when data from the healthy EMA is classified as ”degraded”, and a false negative is when degraded EMA data is classified as ”healthy”. Figures 4.65 through 4.68 show the performance metrics for each signal over the five operating conditions for the case where training was performed separately for each condition. Table 4.5 summarizes the total number of correct classifications, false negatives and false positives for each signal. For this training case, the results show a high correct classification percentage with very few false positives and false negatives for each signal. The results with the LVDT, Motor Velocity and Accelerometer signals all have correct classification percentages of 99% or greater when summarized over all conditions. The Phase A current had a slightly less correct classification rate with 5% false positions and 10% false negatives.

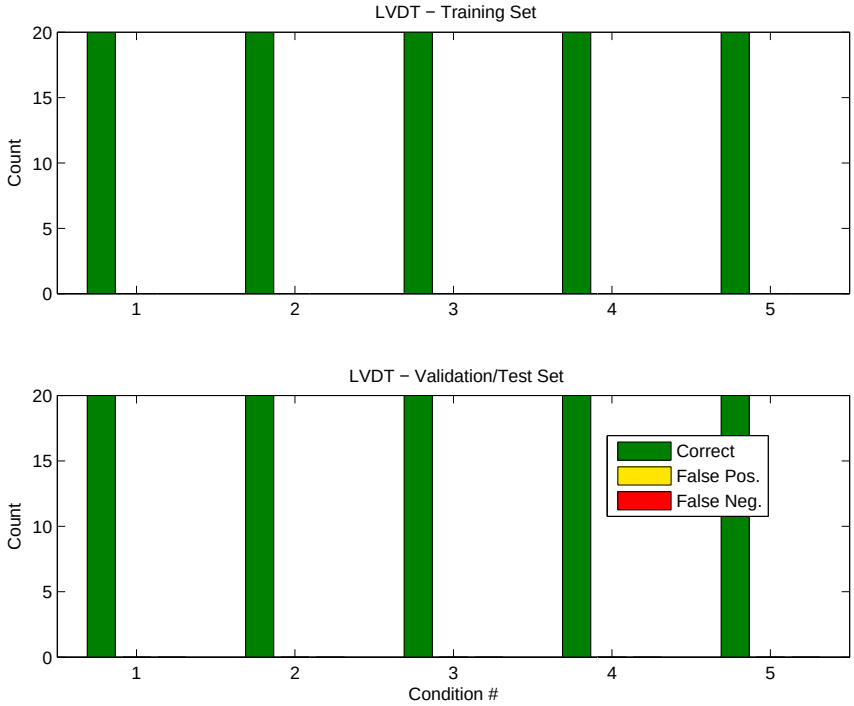

Figure 4.65: LVDT Performance Metrics - Condition Based Training

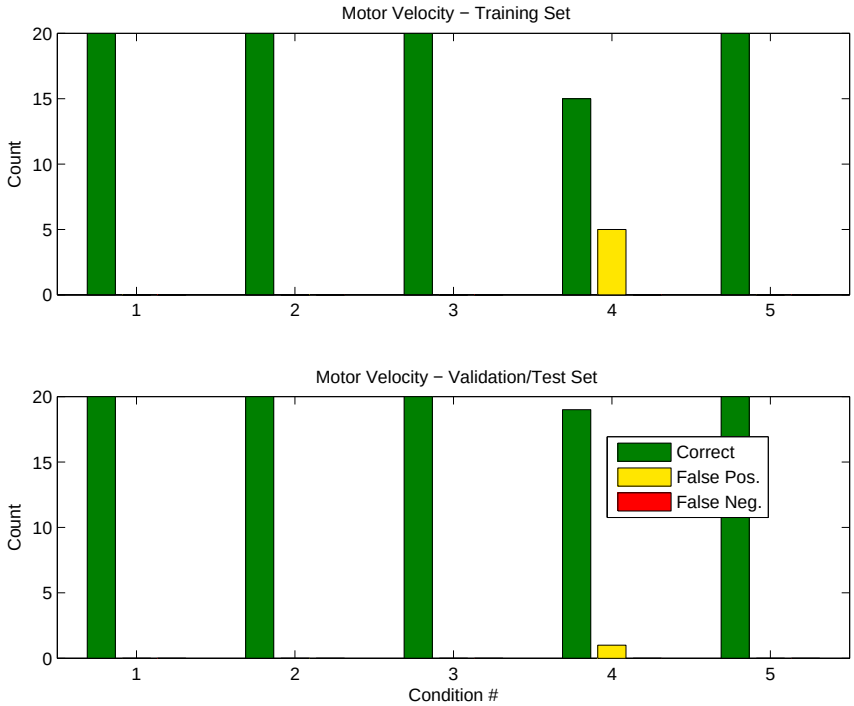

Figure 4.66: Motor Velocity Performance Metrics - Condition Based Training

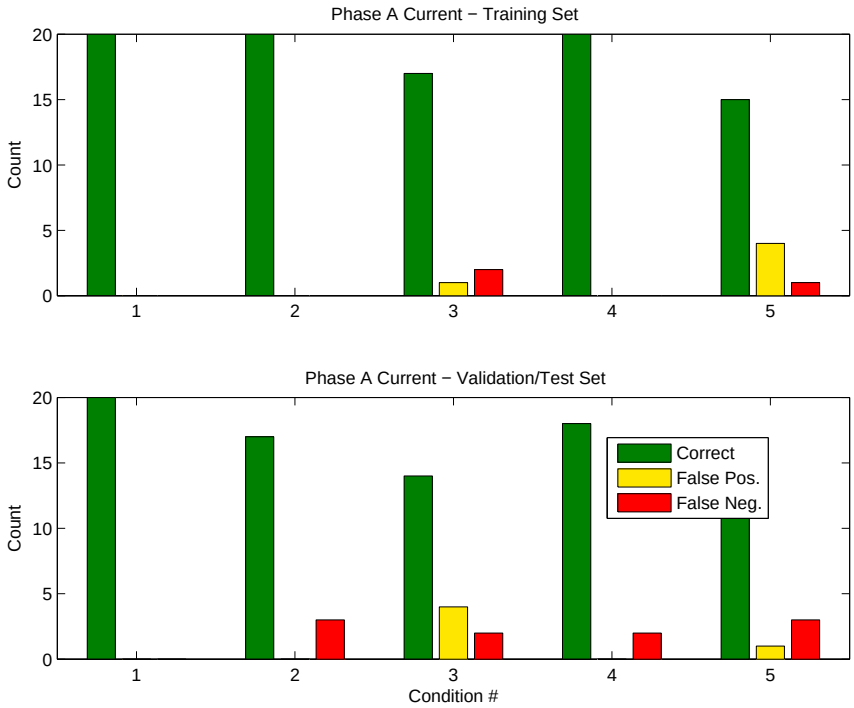

Figure 4.67: Phase A Current Performance Metrics - Condition Based Training

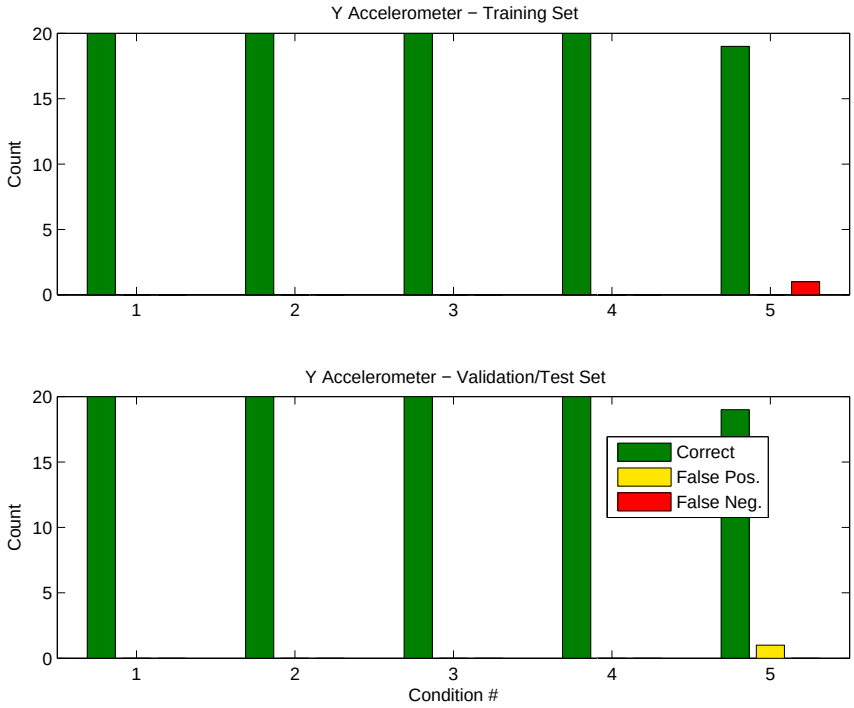

Figure 4.68: Y Axis Accelerometer Performance Metrics - Condition Based Training

Table 4.5: Classification Statistics with a Classifier per Condition

Signal	% Correct	% False Positives	% False Negatives
LVDT	100	0	0
Motor Velocity	99	1	0
Current	85	5	10
Y Accelerometer	99	1	0

Similarly, the classification results with the condition independent training method are plotted in Figures 4.69 through 4.72 and summarized in Table 4.6. Although the results are less impressive compared to training method 1, a decrease in classifier performance is expected since each operating condition will produce different signal characteristics and some conditions are more likely to expose a defect than others. For instance, conditions with higher speeds and loads will produce greater vibrations in the presence of a defect than in conditions where speeds and/or loads are lower.

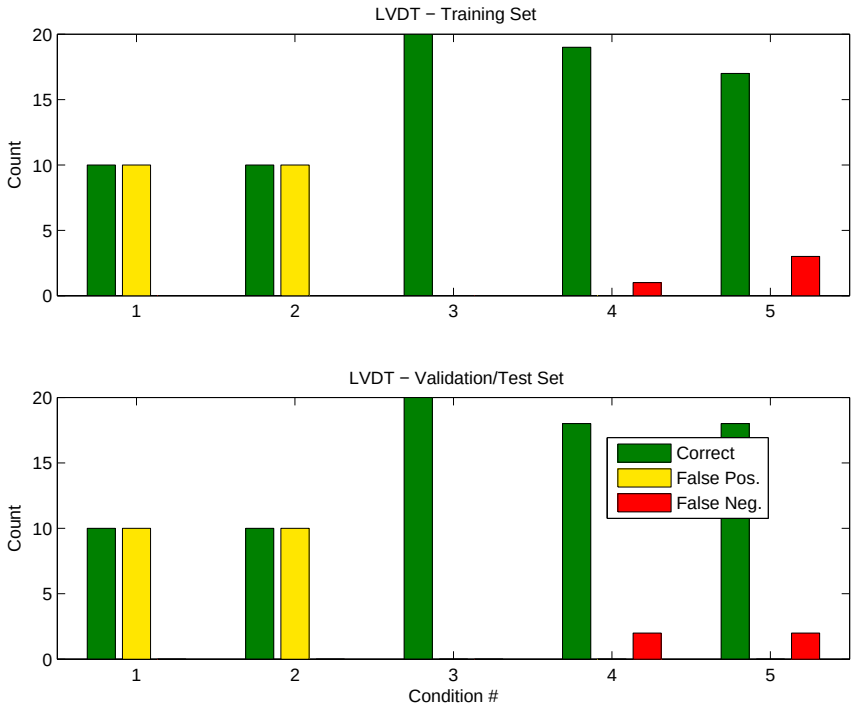

Figure 4.69: LVDT Performance Metrics - Condition Independent Training

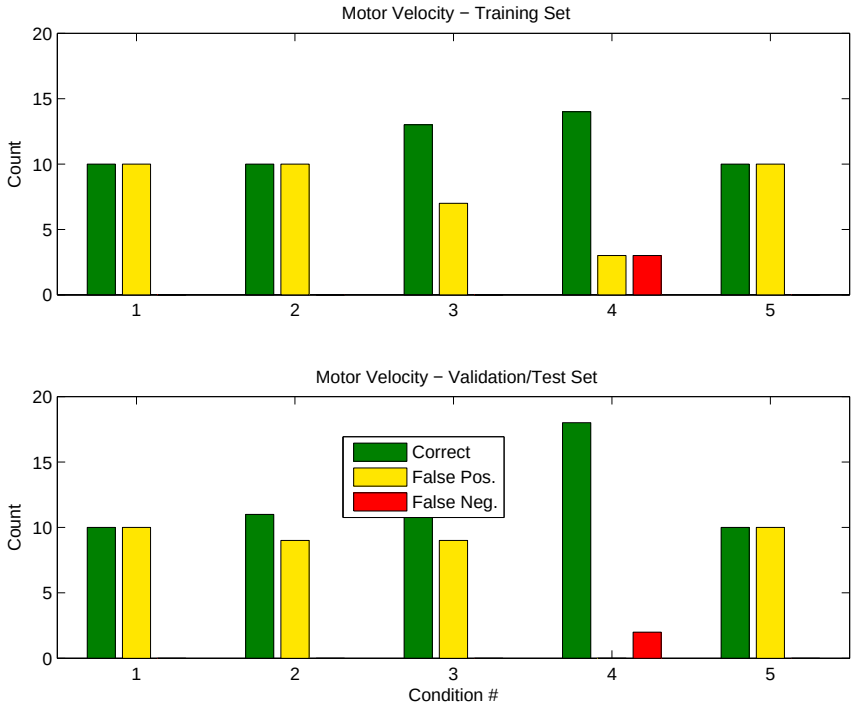

Figure 4.70: Motor Velocity Performance Metrics - Condition Independent Training

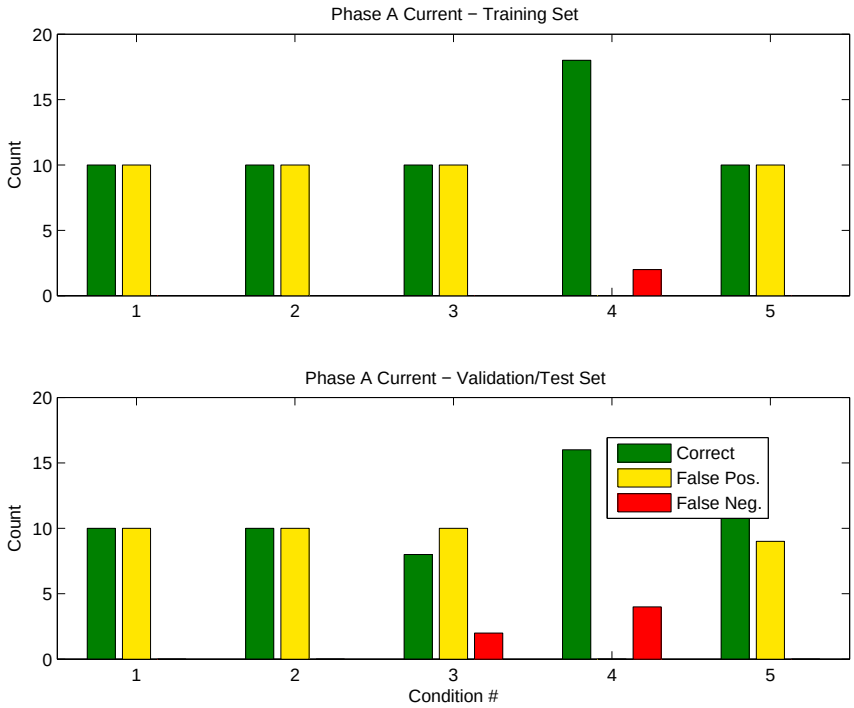

Figure 4.71: Phase A Current Performance Metrics - Condition Independent Training

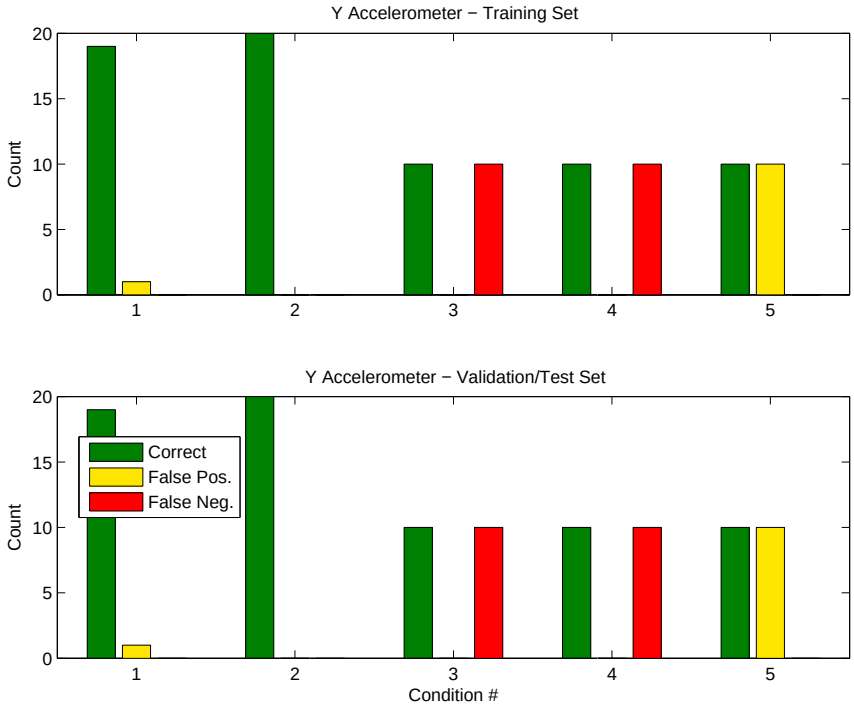

Figure 4.72: Y Axis Accelerometer Performance Metrics - Condition Independent Training

Table 4.6: Classification Statistics with a Single Classifier

	% Correct	% False Positives	% False Negatives
LVDT	76	20	4
Motor Velocity	60	38	2
Current	55	39	6
Y Accelerometer	69	11	20

4.5 Discussion

In order to explain and validate the results for both training cases, a closer look at the raw and processed data for each signal must be done to determine if the classifier is exposing features in the data due to the presence of the bearing defect as desired or of some other phenomena.

The accelerometer signal was a good indicator of EMA condition, having sharp peaks at harmonics of the bearing inner ring defect frequency for the degraded EMA. The magnitude of the peaks was largest for conditions 1 and 2 where motor speeds were the highest (ref. Figure 4.10 and 4.22). For the other conditions where motor speed was lower, the PSD magnitudes were smaller but could still be distinguished from the healthy accelerometer data. This resulted in a low number of false positives and false negatives, especially for the case where training was performed separately on each condition. In fact, no samples were misclassified for conditions 1 and 2 for both training methods. For the conditions where motor speed was lower, the number of incorrect classifications increased for the condition independent training method.

The Phase Current signal was expected to be a good signal for EMA condition monitoring, since it had been used in other research to detect faults

in motor controlled systems. However, for the classifiers trained for each condition, the correct classification percentage was the lowest of any signal at 85%. This is mainly due to the fact that the separation between the healthy and degraded EMA samples in the feature plots was very small compared with the other signals and often overlapped making correct classification difficult. However, the classifier seems to be most successful for conditions 1 and 2 where motor speed is the highest. The PSD plots for these cases show large sidebands around the fundamental frequency (6 orders) which may be due to the deficient lubrication (ref. Figure 4.10 and 4.22). At lower speeds these sidebands are less pronounced and the healthy EMA samples begin to show larger PSD magnitudes, much like they did for the LVDT and motor velocity signals for conditions 3-5. It was also expected that the Phase Current PSD would show bearing defects at harmonics of the motor current defect frequency according to Equation (2.4). However since the defect frequencies ($f_c/f_r = |6 + 6.123m|$) happened to line up almost directly with the harmonics of the fundamental frequency ($f_e/f_r = 6$), exposure of the defect in the PSD signal was not possible.

Surprisingly, the LVDT signal had the lowest number of false positives and false negatives of any signal for both training cases. However, further inspection of the resampled PSD data shows that the healthy EMA has greater amplitudes compared with the degraded EMA, with noticeable peaks at orders of 12 and 36. Since the motor electrical frequency is at 6 orders (6 times the motor frequency) it is possible that electrical noise from the motor was corrupting the LVDT signal when data was collected for the healthy EMA but not as much for the degraded EMA. Since the PCA technique aims to exploit the largest variations in the training set data, this is enough

to cause the weight matrix to be the most sensitive at these orders, resulting in the classification to be based on the noise rather than the defect. A similar explanation follows for the motor velocity signal where the healthy EMA data also had larger amplitudes in the PSD signal.

Chapter 5

Conclusions

This research presented a data driven approach to EMA condition monitoring based on frequency domain feature extraction. Simulation and laboratory results showed the technique was capable of classifying condition of EMAs over non-steady loads and speeds when healthy and defective EMAs contain distinct frequency domain characteristics. This is a significant improvement over past research which cited the non-steady EMA operation as a reason for missed detections. For instance, accelerometer data collected for the degraded EMA with inner ring bearing defect clearly showed the defect in the re-sampled PSD signal at distinct frequencies even when motor speed was not steady, which allowed the fault to be detected. The simulation results also showed that multiple distinct defect signatures synchronous with motor position present in data could be isolated with non-steady motor velocities. As a data driven approach, no models or prior knowledge of the EMA faults was needed. Instead training data collected from the degraded and healthy EMAs was used to train the feature extraction and classification algorithms. A trained feature transformation matrix was used to deal with contending features and reduce the feature data prior to classification. In this research, frequency domain features were reduced from a dimension of 100 to 2 while retaining the most important frequency information.

Although the simulation was important for validating the approach, there

were some important conclusions that could be drawn from the laboratory results that could not be gleaned from the simulated data. Accelerometer data proved to be the best signal for EMA condition monitoring, clearly showing the defect in the resampled PSD and resulted in a small percentage of false negatives and positives. Although motor current was not a good signal for detecting the bearing fault, it is inconclusive whether or not motor phase currents are good signals for condition monitoring of EMAs since the defect frequencies overlapped with the fundamental current frequency. The LVDT and motor velocity signals had a surprisingly high correct classification rate. However, inspection of the data revealed higher noise content for these signals when data was collected for the Healthy EMA so the feature extraction and classification algorithms were trained to distinguish the noise rather than the defect.

Two training methods were also explored in the laboratory demonstration. In the first method, training was done separately for each condition so that Bayesian decision boundaries were tailored for each condition. This resulted in a low amount of false positives and false negatives for each signal. Implementation of this scheme would require the operating condition (load and motor speed) to be known or able to be determined. The second training method was done once using data from all conditions. In this method, only one trained algorithm is needed no matter what the operating condition. This method worked best with accelerometer data in conditions with higher motor velocities. This is expected since conditions with higher speeds and loads will produce greater vibrations in the presence of a defect than in conditions where speeds and/or loads are lower. This leads to the conclusion that not all conditions are appropriate for making condition assessments and that conditions with higher loads and speeds are better for

fault detection and isolation with this approach.

There are several next steps that can be taken to further improve upon the EMA condition monitoring approach and the results. First, this research used motor velocity, position, current and vibration signals separately to arrive at separate condition assessments. Several options can be explored in order to form a single condition assessment. For instance, the separate condition assessments can be fused together to form a single result, or the feature data from each signal can be input to a single classifier. Secondly, the feature extraction process may be improved by exploring the relationships and correlations between sensors, instead of analyzing each signal separately. For example, the cross power spectrum and frequency response functions are other methods that can be used to explore the relationship between signals in the frequency domain which may give further insight into the health of EMAs as they degrade.

Third, the results presented in this research utilized only one healthy and one degraded EMA for training and testing the condition monitoring algorithms. In order to get a better statistical distribution and characterize unit to unit variances, data from several other healthy and degraded EMAs can be incorporated. Fourth, simulation results showed that it was possible to isolate more than one defect, but only a bearing defect was utilized in the laboratory demonstration. Future EMA testing will also include other types of critical faults to validate the isolation of faults in an EMA. Testing other defects would also help to evaluate motor current as a viable signal for EMA condition monitoring since the motor current bearing defect frequency coincided with the fundamental current frequency in the lab demonstration. Finally, this research focused on the feature extraction and fault diagnosis portions of Integrated Health Management for EMAs. To better facilitate

maintenance operations and decision support in the field, prognostics capabilities need to be added that provide advanced warning of failure.

Bibliography

[1] J. Rosero, J. Ortega, E. Aldabas, and L. Romeral, "Moving towards a more electric aircraft," *Aerospace and Electronic Systems Magazine, IEEE*, vol. 22, pp. 3 – 9, 2007.

[2] L. S. Botten, R. C. Whitley, and D. A. King, "Flight control actuation technology for next generation all-electric aircraft," *Technology Review Journal*, Fall/Winter 2000.

[3] L. Hao, Y. Jinsong, Z. Ping, and L. Xingshan, "A review on fault prognostics in integrated health management," *The Ninth International Conference on Electronic Measurement and Instruments*, 2009.

[4] M. Smith, C. Byington, M. Watson, S. Bharadwaj, G. Swerdon, K. Goebel, and E. Balaban, "Experimental and analytical development of health management for electro-mechanical actuators," *IEEE Aerospace Conference*, pp. 1 – 14, 2009.

[5] S. C. Byington, M. Watson, D. Edwards, and P. Stoelting, "A model-based approach to prognotics and health management for flight control actuators," in *IEEE Aerospace Conference Proceedings*, vol. 6, pp. 3551 – 3562, 2004.

[6] E. Balaban, P. Bansal, P. Stoelting, A. Saxena, K. Goebel, and S. Curran, "A diagnostic approach for electro-mechanical actuators in aerospace systems," *IEEE Aerospace conference*, pp. 1 – 13, 2009.

[7] D. Bodden, N. Scott Clements, B. Schley, and G. Jenney, "Seeded failure testing and analysis of an electro-mechanical actuator," *IEEE Aerospace Conference*, pp. 1 – 8, 2007.

[8] M. Baybutt, S. Nanduri, P. Kalgren, D. Bodden, N. Clements, and S. Alipour, "Seeded fault testing and in-situ analysis of critical electronic components in ema power circuitry," *IEEE Aerospace Conference*, pp. 1 – 12, 2008.

[9] C. Byington, M. Watson, and D. Edwards, "Data-driven neural network methodology to remaining life predictions for aircraft actuator components," *IEEE Aerospace Conference Proceedings*, vol. 6, pp. 3581 – 3589, 2004.

[10] D. Brown, G. Georgoulas, H. Bae, G. Vachtsevanos, R. Chen, Y. Ho, G. Tannenbaum, and J. Schroeder, "Particle filter based anomaly detection for aircraft actuator systems," *IEEE Aerospace conference*, 2009.

[11] L. Romeral, J. Rosero, A. Espinosa, J. Cusido, and J. Ortega, "Electrical monitoring for fault detection in an ema," *IEEE Aerospace and Electronic Systems Magazine*, vol. 25, pp. 4 – 9, 2010.

[12] C. Wang and R. Gao, "Wavelet transform with spectral post-processing for enhanced feature extraction," *Instrumentation and Measurement, IEEE Transactions on*, vol. 52, pp. 1296 – 1301, 2003.

[13] K.-K. Huh, R. Lorenz, and N. Nagel, "Gear fault diagnostics integrated in the motion servo drive for electromechanical actuators," *IEEE Energy Conversion Congress and Exposition*, pp. 2255 – 2262, 2009.

[14] W. Zhou, T. Habetler, and R. Harley, "Stator current-based bearing

fault detection techniques: A general review," *IEEE International Symposium on Diagnostics for Electric Machines, Power Electronics and Drives*, pp. 7 – 10, 2007.

[15] A. Malhi and R. Gao, "Pca-based feature selection scheme for machine defect classification," *IEEE Transactions on Instrumentation and Measurement*, vol. 53, pp. 1517 – 1525, 2004.

[16] B. Zhang, G. Georgoulas, M. Orchard, A. Saxena, D. Brown, G. Vachtsevanos, and S. Liang, "Rolling element bearing feature extraction and anomaly detection based on vibration monitoring," *16th Mediterranean Conference on Control and Automation*, pp. 1792 – 1797, 2008.

[17] S. Rajagopalan, T. Habetler, R. Harley, T. Sebastian, and B. Lequesne, "Current/voltage based detection of faults in gears coupled to electric motors," *IEEE International Conference on Electric Machines and Drives*, pp. 1780 – 1787, 2005.

[18] A. Knight and S. Bertani, "Mechanical fault detection in a medium-sized induction motor using stator current monitoring," *IEEE Transactions on Energy Conversion*, vol. 20, pp. 753 – 760, 2005.

[19] L. Eren and M. Devaney, "Motor current analysis via wavelet transform with spectral post-processing for bearing fault detection," *Proceedings of the 20th IEEE Instrumentation and Measurement Technology Conference*, vol. 1, pp. 411 – 414, 2003.